Study on composition dependent phase stability of Ni50MnxIn50-x shape memory alloys by ab-initio simulation

Xiaomeng Liu

UNIVERSITÉ DE LORRAINE

NORTHEASTERN UNIVERSITY

DISSERTATION

Presented at
Université de Lorraine and Northeastern University

Xiaomeng LIU 刘肖朦

To obtain the doctor's degree of
University of Lorraine and Northeastern University

SPECIAL FIELD: Engineering Science
OPTIONL: Materials Science

Study on composition dependent phase stability of $Ni_{50}Mn_xIn_{50-x}$ shape memory alloys by ab-initio simulation

Defended on July 16th, 2020 in front of the jury:

Alexandre LEBON	Maitre de Conférences HDR	Université Bretagne Occidentale, France	Reviewer & Jury member
Daoyong CONG	Professor	University of science and technology Beijing, China	Reviewer & Jury member
Hong XU	Professor	Université de Lorraine, France	Jury member
Jean-marc RAULOT	Professor	Université de Lorraine, France	Supervisor
Liang ZUO	Professor	Northeastern University, China	Supervisor
Claude ESLING	Professor	Université de Lorraine, France	Invited

Laboratoire d'Étude des Microstructures et de Mécanique des Matériaux, LEM3

7 rue Félix Savart 57070 Metz, France

Abstract

A series of first-principle calculations to discover the martensitic transition of the Ni-Mn-In alloys were implemented using the pseudopotential method by VASP and the full charge density method by EMTO-CPA within the framework of the Density Functional Theory (DFT).

In the stoichiometric $Ni_{50}Mn_{25}In_{25}$ alloy, the effect of effective Coulomb and exchange parameters ($U+J$) on the phase stability, structural and magnetic properties was studied. The lattice parameters and the phase stability vary with the U and J couplings in the cubic $L2_1$ austenite. However, the bandgap is still showing metallic bonding in the cubic $Ni_{50}Mn_{25}In_{25}$ alloy.

To figure out the effect of excess Mn atoms on the preference of the martensite structure, the tetragonal distortion was employed in the off-stoichiometric $Ni_{50}Mn_xIn_{50-x}$ alloys with different Mn contents. The calculations were conducted with the optimization of the magnetic structure, where the stoichiometric $Ni_{50}Mn_{25}In_{25}$ alloy was served as the reference. The ground state-energy-resolved tetragonal distortion reveals that the excess Mn changes the preferred stable structure from the perfect cubic $L2_1$ structure to the tetragonally distorted structures. Furthermore, to find out more accurate preference of the martensite structure, the formation energies were calculated. The results show that, the orthorhombic structure is preferred at lower Mn concentrations (between 29 at. % and 40 at. %), whereas the tetragonal $L1_0$ structure is more stable at the higher Mn concentrations (above 40 at. %). Moreover, the effect of the Mn concentration on the magnetic properties was also studied. With the increase of the excess Mn content, the magnetic moment increases linearly in the ferromagnetic cubic $L2_1$ structure, whereas it varies in the two kinds of martensite. The excess Mn could lead to the coexistence of ferromagnetism and antiferromagnetism. The appearance of the antiferromagnetism could be attributed to the Ni-Mn antiferromagnetic interaction in the tetragonal martensite.

Furthermore, the effects of Mn concentration and thermally excited contributions (including the vibrational, electronic excitation and magnetic contributions) on the phase stability of austenite and martensite from 0 K to finite temperatures in Heusler type $Ni_{50}Mn_xIn_{50-x}$ shape memory alloys were also studied. Results show that at 0 K, the energy differences between the non-modulated (NM) martensite and the austenite become negative when extra Mn is added, indicating that the added Mn stabilizes the martensite and promotes martensitic transformation. At finite temperatures, the three thermal contributions (the vibrational, electronic excitation and magnetic contributions)

were further calculated based on the equilibrium structure at 0 K. It was revealed that the vibrational entropies of the two phases increase with the increase of the temperature for all Mn contents. Under the two effects (temperature and Mn-content), the austenite has a larger vibrational entropy than the martensite, which indicates that the vibrational entropy contributes to promoting the martensitic transition. The Mn content and the temperature show a similar influence on the electronic entropies of the two phases. And the magnetic moments increase linearly with the Mn content, however, the influence of temperature is relatively small. Above 100 K, the magnetic moment of the austenite is higher than that of the martensite in ferromagnetic $Ni_{50}Mn_{29.25}In_{20.75}$ alloy, suggesting that the magnetic entropy makes a similar contribution to promote the martensitic transformation, like the vibrational and electronic excitation entropies.

The present work provides fundamental knowledge to understand the martensitic transition of off-stoichiometric $Ni_{50}Mn_xIn_{50-x}$ alloys, which could be used for the design of ferromagnetic shape memory alloys with improved functional performances.

Keywords: Ni-Mn-In alloys; VASP; EMTO-CPA; martensitic transition; formation energy; thermodynamic contribution

Résumé

Une série de calculs de premier principe pour étudier la transformation martensitique des alliages Ni-Mn-In a été mise en œuvre en utilisant la méthode du pseudopotentiel de VASP et la méthode de densité de charge complète par EMTO-CPA dans le cadre de la théorie de la fonctionnelle de la densité (DFT).

Pour l'alliage stoechiométrique $Ni_{50}Mn_{25}In_{25}$, l'effet de Coulomb efficace et des paramètres d'échange ($U + J$) sur la stabilité de phase, les propriétés structurelles et magnétiques a été étudié. Les paramètres du réseau et la stabilité de phase varient avec les différents couplages U et J dans l'austénite cubique $L2_1$. Cependant, la bande interdite présente toujours une liaison métallique dans l'alliage cubique $Ni_{50}Mn_{25}In_{25}$.

Pour déterminer l'effet des atomes de Mn en excès sur la préférence de la structure martensitique, la distorsion tétragonale a été utilisée dans les alliages $Ni_{50}Mn_xIn_{50-x}$ avec différentes teneurs en Mn. La distorsion tétragonale à l'état fondamental, résolue en énergie, révèle que l'excès de Mn change la structure stable préférée de la structure cubique parfaite $L2_1$ en structures déformées tétragonales. De plus, pour découvrir une préférence plus précise de la structure de la martensite, les énergies de formation ont été calculées. Les résultats montrent que la structure orthorhombique est préférée aux concentrations de Mn faibles (entre 29 at.% et 40 at.%), Tandis que la structure tétragonale $L1_0$ est plus stable aux concentrations Mn plus élevées (supérieures à 40 at.%). De plus, l'effet de la concentration en Mn sur les propriétés magnétiques a également été étudié. Avec l'augmentation de la teneur en Mn en excès, le moment magnétique augmente linéairement dans la structure ferromagnétique cubique $L2_1$, alors qu'il varie dans les deux types de martensite. L'excès de Mn pourrait conduire à la coexistence du ferromagnétisme et de l'antiferromagnétisme. L'apparition de l'antiferromagnétisme pourrait être attribuée à l'interaction antiferromagnétique Ni-Mn dans la martensite tétragonale.

De plus, les effets de la concentration en Mn et des contributions excitées thermiquement (y compris les contributions vibratoires, électroniques et magnétiques) sur la stabilité de phase de l'austénite et de la martensite de 0 K à des températures finies dans les alliages à mémoire de forme $Ni_{50}Mn_xIn_{50-x}$ typés Heusler ont également été étudiés. Les résultats montrent qu'à 0 K, les différences d'énergie entre la martensite non modulée (NM) et l'austénite deviennent négatives lorsque du Mn supplémentaire est ajouté, indiquant que le Mn ajouté stabilise la martensite et

favorise la transformation martensitique. Aux températures finies, il a été révélé que les entropies vibrationnelles des deux phases augmentent avec l'augmentation de la température pour toutes les teneurs en Mn. Sous les deux effets (température et teneur en Mn), l'austénite a une entropie vibrationnelle plus grande que la martensite, ce qui indique que l'entropie vibrationnelle contribue à favoriser la transformation martensitique. La teneur en Mn et la température montrent une influence similaire sur les entropies électroniques des deux phases. Et les moments magnétiques augmentent linéairement avec la teneur en Mn, cependant, l'influence de la température est relativement faible. Au-dessus de 100 K, le moment magnétique de l'austénite est plus élevé que celui de la martensite dans l'alliage ferromagnétique $Ni_{50}Mn_{29.25}In_{20.75}$, suggérant que l'entropie magnétique contribue de manière similaire à favoriser la transformation martensitique, comme les entropies vibratoires et d'excitation électronique.

Le présent travail fournit des connaissances fondamentales pour comprendre la transformation martensitique des alliages Ni-Mn-In stœchiométriques, qui pourraient être utilisés pour concevoir des alliages ferromagnétiques à mémoire de forme avec des performances fonctionnelles améliorées.

Mots-clés: Alliages Ni-Mn-In; VASP; EMTO-CPA; transition martensitique; énergie de formation; contribution thermodynamique

摘要

在密度泛函理论(DFT) 框架下，本文利用基于赝势方法的 VASP 和基于全电子方法的 EMTO-CPA 的两种量子力学计算软件包，展开了一系列的 Ni-Mn-In 形状记忆合金的马氏体相变研究。

在立方 $L2_1$ 结构奥氏体相化学计量比的 $Ni_{50}Mn_{25}In_{25}$ 合金中，研究了有效库仑和交换参数（$U+J$）对相稳定性，晶体结构和磁性能的影响。其中，晶格参数和相稳定性随不同的 U 和 J 耦合参数而变化，而由合金电子结构可知，带隙仍显示为金属性。

采用四方畸变方法，在非化学计量比 $Ni_{50}Mn_xIn_{50-x}$ 合金中进行了 Mn 含量对 Ni-Mn-In 合金马氏体组织稳定性的研究。通过磁结构优化计算，进行合金基态能量计算。以化学计量比 $Ni_{50}Mn_{25}In_{25}$ 合金为参考，过量的 Mn 使得 Ni-Mn-In 合金稳定结构由立方 $L2_1$ 变为四方结构。此外，为了得到更准确的马氏体结构偏好，两种马氏体结构的形成能分别计算：*1)* 铁磁性 $L1_0$ 四方马氏体，采用化学无序方法；*2)* 铁磁性正交马氏体，采用超胞方法。通过比较由不同优化方法计算所得晶体结构形成能可知，当 Mn 含量较低时（29 at. % ~ 40 at. %），合金的稳定结构为斜方晶体；当 Mn 含量较高时（> 40 at. %），合金的优选结构为四方 $L1_0$ 晶体。此外，本文计算了 Mn 含量对磁性能的影响。随着 Mn 含量增加，铁磁立方 $L2_1$ 结构中的磁矩线性增加，而两种马氏体中的磁矩却发生变化。过量的 Mn 可导致铁磁性和反铁磁性的共存，并且反铁磁性的出现可归因于四方马氏体中 Ni-Mn 反铁磁性相互作用。

此外，还研究了 Mn 含量和热激发贡献（包括振动，电子激发和磁贡献）对铁磁性奥氏体和马氏体在 0K 至有限温度下相稳定性的影响。在 0 K 时，富余 Mn 使得非调幅（NM）马氏体和奥氏体之间的能量差为负值，表明富余 Mn 稳定了马氏体相稳定性。基于 0 K 时的平衡结构，在有限温度下进一步计算了三个热贡献（振动，电子激励和磁贡献）。在所有的合金中，两相的振动熵随温度的升高而增加。在所有情况下（温度和 Mn 含量），奥氏体振动熵均大于马氏体，这表明振动熵有助于促进马氏体转变。在两相中，富余 Mn 成分和温度对电子熵显示出相似的影响。此外，磁矩随 Mn 含量线性增加，但是温度对其影响相对较小。当温度高于 100 K 时，铁磁 $Ni_{50}Mn_{29.25}In_{20.75}$ 合金中的奥氏体磁矩大于马氏体的磁矩，这表明磁熵与振动熵同时对马氏体相变起到促进作用。

本工作为非化学计量比 Ni-Mn-In 合金的马氏体转变提供了基础知识，并可用于设计功能性能改良的铁磁形状记忆合金。

关键词：Ni-Mn-In 合金; VASP; EMTO-CPA; 马氏体相变; 形成能; 热力学贡献

Contents

Chapter 1 Introduction

1.1 Ni-Mn-In ferromagnetic shape memory alloys

Shape memory alloys can be characterized by two kinds of behaviors: the shape memory effect and the superelasticity [1–4]. The shape memory effect, as shown in Fig. 1.1, stands for the recovering residual strains capacity of the alloys under the thermal field after cyclic loading, and it is related to the thermoelastic martensitic phase transformation [5]. And the superelasticity is associated with the recovering capacity of the loading-originated strains without any residual strains [6]. The shape memory alloys contain two kinds of phases, *i.e.*, the austenite and the martensite, in which the physical properties vary from the one to the other. It includes the phase stability, the thermal conductivity and thermal expansion coefficient, which would be attributed to the different crystal structure and the different electronic structures of the two phases [7–9]. The shape memory effect is related to the phase transition from the austenite to the martensite with different structures, which could also be affected by the chemical compositions of the alloys and the applied field [10]. The variante is the structure of martensite with lower symmetry and the multiple configurations of the martensite.

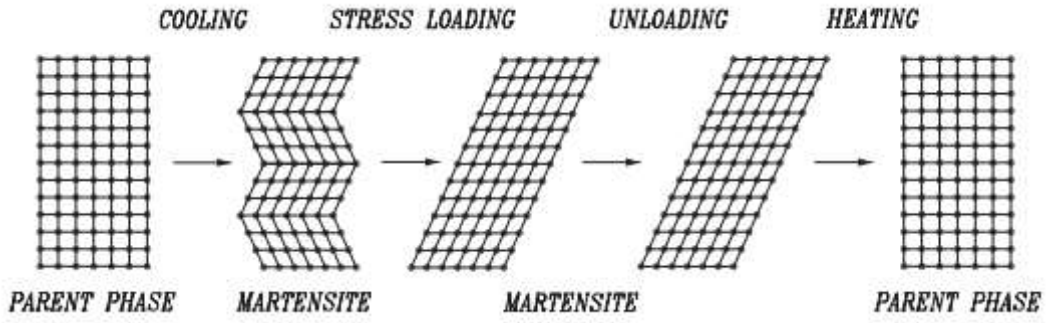

Fig. 1.1 Illustration of the shape memory effect [5, 6]

The shape memory effect was first pointed out in Au-Cd alloys in 1951 [11] and then it was discovered in the Ti-Ni alloys in 1963 [12]. As the shape memory alloy could be used for innovative devices and applications (including aerospace [13,14], automotive [15], and actuators [16]), it has attracted increasing attention in recent years [17].

Magnetic shape memory alloys would produce motion which is associated with the twin boundaries of the differently oriented martensite variants or the interfaces between the austenite and the martensite [18]. It also force the recovering to its original form under an applied magnetic field [19]. Among them, the Ni-Mn-Ga alloys produce the large magnetic-field-induced strains [20,21], which could be deduced to the reorientation of the martensite twins, under the magnetic field. However, its magnetostress is quite small, which is due to the small twinning/detwinning resistance [22]. Therefore, as the lower environmental resistant and the strong dependence on the magnetic field, the application of the Ni-Mn-Ga alloys is limited in single crystals under large magnetic-field-induced strain. [23]. For the Ni-Mn-X (X: In, Sn, Sb) alloys, the magnetostriction is attributed to its magnetic field-induced reverse martensitic transformation [24–26]. The shape memory alloys undergo the martensitic transition from the ferromagnetic austenite to the weak-magnetic martensite with temperature reduced [27], which called the metamagnetic shape memory effect. During this process, the martensitic transition temperature could be influenced by the magnetic field, and many unique physical properties would show up, including the giant magnetoresistance, the magneto-thermal conductivity and inverse magnetocaloric effects [28].

Up to now, the Heusler-typed Ni-Mn-In alloys have been studied intensively in many aspects, including crystal structure [29,30] , martensitic phase transition [31–35] and the martensitic phase stability and magnetic properties [30,36–39], using experimental and computational methods. They have attracted increasing attention due to their multi functionality, including metamagnetic shape

memory effect [40,41], giant magnetocaloric effect [42], metamagnetic shape memory effect [43,44], exchange bias effect [45], the giant Hall effect [36], and magnetoresistance effect [46].

1.1.1 Crystal structure of Ni-Mn-In alloys

During the thermodynamic process, a Ni-Mn-In alloy undergoes a series of transformation which results in many different phases with different structures, as shown in the phase diagram in Fig. 1.2. The first step phase transition is that the melt solidified directly into the partially disordered intermediate *B2* phase [47], and the second order *B2* - $L2_1$ transition takes place during cooling [43, 48]. Then, the first order cubic $L2_1$ austenite transform to the martensite with different structures, which is strongly dependent on the chemical composition around the stoichiometric Ni-Mn-In alloy [37]. For the martensitic phase transition, the Heusler typed Ni-Mn-In alloys transform to two kinds of low-temperature martensite phases: i) the modulated martensite, i.e. the orthorhombic or monoclinic modulated structures (i.e. $c/a < 1$, in the cubic coordinate system) with In deplete, such as *6M* [29], *10M* [30], *4O* [49] modulated structures; ii) and the non-modulated martensite, i.e. the tetragonal structure at low In concentration, such as $L1_0$ tetragonal non-modulated structure (i.e. $c/a > 1$, in the cubic coordinate system) [50]. The microstructures were evidenced by the selected area electron diffraction (SAED), the x-ray diffraction (XRD), or the neutron diffraction (ND).

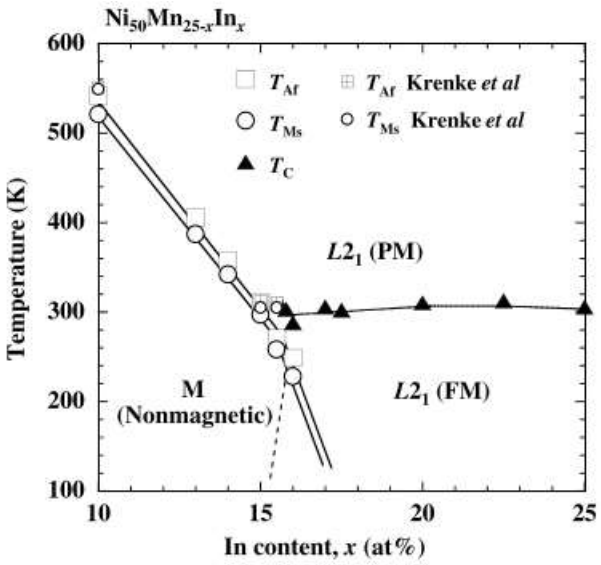

Fig. 1.2 Phase diagram of $Ni_{50}Mn_{25-x}In_x$ alloy [43]

1.1.2 Magnetic properties of Ni-Mn-In alloys

1.1.2.1 Curie temperature

The Curie temperature (T_C) refers to the temperature at which the magnetic transition occurs by losing the long-range magnetic order. During the magnetic transition process, the material transform from the ferromagnetism to the paramagnetism. In the Ni-Mn-In alloys, the ferromagnetic austenite could not transform directly into the ferromagnetic martensite, but have to go through the antiferromagnetic martensite [34,51]. As discovered in the experimental research, the Heusler typed Ni-Mn-Co-In alloys display the unique martensitic transition from the ferromagnetic austenite to the paramagnetic martensite and could be activated under a applied magnetic field [41]. Sutou et. al [27] pointed out that the martensitic transition from the ferromagnetic $L2_1$ structure to an non-magnetic orthorhombic four-layered structure could happen in the Ni-Mn-X (X: In, Sn, Sb) alloys. They discovered that the Curie Temperature (T_C) of the austenite phase keeps stable with the change of composition, whereas the Curie Temperature of the

martensite phase changes obviously with the composition. The Curie temperature of the martensite shows an abrupt decrease at high Mn concentrations in the Ni-Mn-X alloys. Furthermore, in the off-stoichiometric NiMnIn alloys with Ni doped to the Mn site, the Curie temperature of the ferromagnetic state also shows a systematical decrease with the increasing Ni content[38].

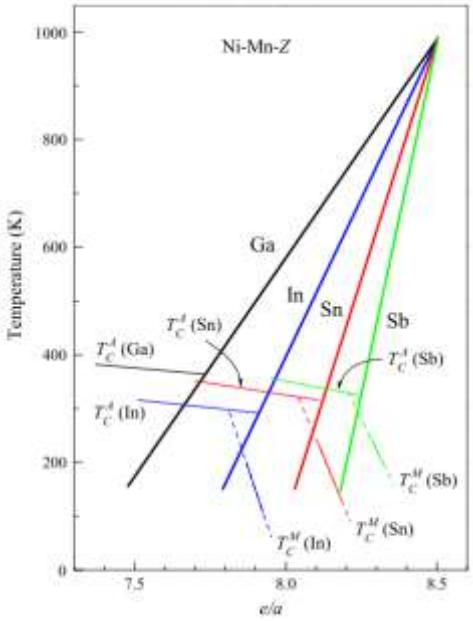

Fig. 1.3 the *e/a* dependence of the martensitic transition temperature (*Ms*) and the Curie temperature of austenite and martensite states for Ni-Mn-Z Heusler alloys with Z as Ga, In, Sn and Sb. [50] (*e/a* is the concentration-weighted average of the valence electrons)

1.1.2.2 Magnetic moment

The magnetic properties of the Heusler off-stoichiometric Ni-Mn-In alloys have been investigated experimentally and theoretically. The previous studies found that the magnetic moment can be mainly attributed to the Mn atoms and the localized magnetic moment, which is caused by the indirect hybridization between the Ni and Mn atoms in the Ni-Mn-based shape memory alloys [50,52,53]. The magnetic moment is increasing with the increased Mn concentration in the Ni-Mn-In austenite [30], which can be attributed to the ferromagnetic coupling

between the Mn atoms located at the In sites and the Mn atoms located at the Mn sites, as discovered by the magnetization measurements of $Ni_{0.5}Mn_{0.5-x}In_x$ (x = 0.14, 0.156) [30,39,43,54]. However, the total magnetic moment of the martensite decreases abruptly when the Mn content exceeds 34 at. % [39,55,56]. It was revealed that the martensite exhibits coexisting ferromagnetic and antiferromagnetic interactions in the off-stoichiometric alloys. This means that the excess Mn results in the antiferromagnetic exchange interactions in the martensite, which could be attributed to the different hybridization of Mn-Mn atoms [39,57] or Ni-Mn atoms [55,58].

1.2 Introduction of a quantum theory of materials

1.2.1 Schrödinger Equation

The physical properties of a solid could be described by the first-principle calculations under the frame of the density functional theory. Using the Schrödinger equations to express all the electronic structural properties, the interaction between the nuclei and electrons could be solved through the Schrödinger equations. However, that needs huge computational capacity and is almost impossible to be carried out even for the extremely small systems. Thus, we only focus on the time-independent situation using the Schrödinger equation in most situations. In the Born-Oppenheimer nonrelativistic approximation, an isolated N-electron atomic or molecular system [1] can be expressed as below,

$$\hat{H}\Psi = E\Psi \tag{1.1}$$

In the equation, E is the electronic energy, $\Psi = \Psi(\vec{x}_1, \vec{x}_2, \ldots, \vec{x}_n)$ is the wave function, and $\hat{H}$ is the Hamiltonian operator [60]

$$\hat{H} = \sum_{i=1}^{N}(-\frac{1}{2}\nabla_i^2) + \sum_{i=1}^{N} v(\vec{r}_i) + \sum_{i<j}^{N}(\frac{1}{\vec{r}_{ij}}) \tag{1.2}$$

$$\text{with } v(\vec{r}_i) = -\sum_\alpha \frac{Z_\alpha}{\vec{r}_{i\alpha}} \tag{1.3}$$

$v(\vec{r}_i)$ is the "external" potential acting on electron i, which is introduced from the nucleus with Z_α charges. As the mass of the nuclei is much larger than the electrons, the nuclei moves much slower than the electrons and can be treated as fixed with the electrons moving around. Then, the kinetic energy of the nucleus, which contains the constant potential energy, is set to be zero. Therefore, the Hamiltonian of the electron can be written compactly as

$$\hat{H}_{elec} = \hat{T} + \hat{V}_{Ne} + \hat{V}_{ee} \tag{1.4}$$

The electronic wave function Ψ_{elec} and its energy $E_{elec}$is the solution of the Schrödinger equation.

$$\hat{H}_{elec}\Psi_{elec} = E_{elec}\Psi_{elec} \tag{1.5}$$

The E_{elec} and the constant nuclear repulsion E_{nuc} will obtain the total energy

$$E_{tot} = E_{elec} + E_{nuc} \qquad with \qquad E_{nuc} = \sum_{A=1}^{M}\sum_{B>A}^{M} \frac{Z_A Z_B}{R_{AB}} \tag{1.6}$$

1.2.2 Variational principle of ground state

The Schrödinger equation must be obtained with respect to the appropriate boundary conditions. There are many acceptable independent solutions for a given system: the eigenfunctions Ψ_k, with corresponding energy eigenvalues E_k. The Ψ_k set is complete, and the Ψ_k may always be taken to be orthogonal and normalized

$$\int \Psi_k^* \Psi_l dx^N = \langle \Psi_k | \Psi_l \rangle = \delta_{kl} \tag{1.7}$$

$\int dx^N$ is the integration cover 3N spatial coordinates and summation over N spin coordinates. The Ψ_0 and E_0 are used to denote the ground-state wave function and energy.

With the system in the state Ψ, the expectation value of the energy will be given by

$$E[\Psi] = \frac{\langle\Psi|\hat{H}|\Psi\rangle}{\langle\Psi|\Psi\rangle} \quad where \quad \langle\Psi|\hat{H}|\Psi\rangle = \int \Psi^* \hat{H} \Psi d\vec{x} \tag{1.8}$$

The variational principles reveal that the upper bound of the ground state energy E_0 is obtained from the guessed state Ψ. Therefore, the $E[\Psi]$ could be used to minimize the N-electron wave functions with ground state Ψ_0.

$$E_0 = min_{\Psi \to N} E[\Psi] = min_{\Psi \to N} \langle \Psi | \hat{T} + \hat{V}_{Ne} + \hat{V}_{ee} | \Psi \rangle \tag{1.9}$$

1.2.3 Hartree-Fock approximation

In many-dimensional space, the solving of the wave equation is so complex that it could not deal with the atoms with many electrons in the accurate quantum theory. Therefore, the combination of the employing the self-consistent field[61] and the Hartree's method [4] is resorted as the best approximation method. By displaying the many-body wave function as a Slater determinant [1] for the single particle wave functions, the Pauli Exclusion Principle is used to execute the Hartree-Fock approach [2] by considering the equivalent electrons into the exchange phenomena. Fock [62] pointed out, the three-dimensional wave functions will be suitable to the Hartree's equation only when the three-dimensional wave function is formed by taking the best approximation into the many-dimensional wave function. That will satisfy the extra terms contained which could be treated as the exchange phenomena representing into the equations [63].

For a N electrons system with the nuclear potential V_{ext}, the ground-state wave function Ψ_0 and energy E_0 could be determined by the vibrational principle [61]. The ground state energy can be treated as a function of electrons number (N) and the nuclear potential (V_{ext}):

$$E_0 = E[\, N, V_{ext}\,] \tag{1.10}$$

The solutions of the Schrödinger equation could be solved by the vibrational principle with the approximation of many-electron wave function $\Psi(\vec{r}_1, \vec{r}_2, \ldots, \vec{r}_N)$ with $\vec{r}_i$ as the particle

coordinates and spins. Based on the self-consistent field, the core and the valence components could be used to separate the vibrational principle $\Psi(\vec{r}_1, \vec{r}_2, \ldots, \vec{r}_N)$.

Then, the trial function (as below) can be used to derive the Hartree equation [62]:

$$\Psi(\vec{r}_1, \vec{r}_2, \ldots, \vec{r}_N) = \psi_1(\vec{r}_1) \ldots \ldots \psi_N(\vec{r}_N) \tag{1.11}$$

Therefore, with the potential produced from the average field, which is arisen from the other electrons within the self-consistent field, each single $\psi_i(\vec{r}_i)$ could satisfy a one-electron Schrödinger equation.

The ensuing equations are too difficult to solve. But the important physics, *i.e.* the electron-electron interaction, still could not be obtained from the Hartree-Fock approximation. Beyond the Hartree-Fock approximation, the wave function could be constructed for example as a series of Slater determinants with huge computational consuming. Therefore, this method could only be employed to study very small systems.

1.3 Fundamentals of the Density Functional Theory

In the condensed matter physics, using the first principle to predict the crystal structure is the most fundamental problem. The first principle method could be used to compute the total ground state energy of system with electrons and nuclei. As nearly all the physical properties could be related to total energies or to differences between total energies, the ground state energy should be calculated and minimized with the relaxation of the nuclear positions to predict and to obtain the equilibrium state of the solid [64]. Therefore, to predict the equilibrium lattice constant of a crystal, the total energy is implemented by a series of lattice distortion calculations, and then the equilibrium structure state could be obtained by the Equation of States. Furthermore, by minimizing the total energy, we could obtain the equilibrium lattice constant of a crystal or obtain the equilibrium structures of surfaces, interfaces, defects and nanostructures. Total-energy

techniques also have been successfully used to predict the elastic constants, the phonons vibrations, and the electronic structures [63,65].

The first principle calculations, which could be used to calculate the quantum-mechanical properties, can be used to study the complex solid materials. To understand the physical properties of the solid, the first principle calculations could be used by analyze the crystal structure and the electronic structure information to guide materials design with higher quality and better performance.

1.3.1 Electron density

Defined as electron number of per unit volume in a accurate state, the electron density ($\rho(\vec{r})$) is the central quantity in density functional theory. In term of Ψ, its formula is

$$\rho(\vec{r}) = N \int \dots \int |\Psi(\vec{x}_1, \vec{x}_2, \dots, \vec{x}_N)|^2 ds_1 d\vec{x}_2 \dots d\vec{x}_N \tag{1.12}$$

The non-negative function, $\rho(\vec{r})$, vanishes at infinity and can be integrated by the total number of the electrons.

$$\rho(\vec{r} \to \infty) = 0 \qquad \int \rho(\vec{r}) d\vec{r} = N \tag{1.13}$$

For the ground state atoms, the electronic density decreases monotonically with the distance from the nucleus [66], in approximately piecewise exponential fashion [67]. The electron density has a finite value for an atom which we designate as $\rho(\vec{r}_0)$. Therefore, the results of electron density from the standard first-order perturbation theory for a nondegenerate state will be obtained.

1.3.2 the Thomas-Fermi model

According to the quantum mechanics principles, by employing a series of approximations and simplifications regarding to the interaction between the nucleus and the electrons, the first-principle

method could solve the Schrödinger equation. Therefore, the total energy calculation can be carried out by the first principle methods to solve the many-body system. Therefore, some approximations are employed to solve the many-body problem.

As the density is the function of three-dimension coordinates, the number of freedom could be decreased significantly. Instead of using the wave function to solve the many-body problem, Thomas [68] and Fermi [69] proposed an alternative approach by the solution of the electronic density. Thomas found that, if the effective electric field could be obtained, the observable atomic constants could be calculated theoretically. Based on the Thomas and Fermi approximation, the independent fermions of the electrons can be written as below with Coulomb energy,

$$E_{es}[n] = \frac{e^2}{2} \int d\vec{r} \int dr' \frac{n(\vec{r})n(\vec{r}')}{|\vec{r} - \vec{r}'|} \tag{1.14}$$

With kinetic energy

$$T[n] = \int d\vec{r} t[n(\vec{r})] \tag{1.15}$$

Using the constant electron number $N = \int d\vec{r} n(\vec{r})$, $E[n]$ could be minimized,

$$E[n] + \lambda N = T[n] + E_{es}[n] + \int d\vec{r} n(\vec{r}) \{V_{ext}(\vec{r}) + \lambda\} \tag{1.16}$$

The corresponding Euler equation in the Thomas-Fermi equation will be obtained. TF approximation makes the total energy be calculated for all atoms within the well-defined mathematical model.

1.3.3 the Hohenberg-Kohn theorems

The ground state energy can be treated as the minimized total energy, and the exact single-particle ground-state density corresponds to the density of this minimized state [70]. In 1964,

Hohenberg and Kohn [71] pointed out that the exact ground-state energy of a system with interacting electrons can be expressed by the functional of the electron density

$$E_{GS} = E[\rho(\vec{r})] \tag{1.17}$$

The electronic density could be employed to determine the Hamiltonian operator within the Hohenberg-Kohn theorem. According to the density theory function, the related physical properties could be obtained. In this theory, the external potential $V_{ext}(\vec{r})$ can be treated as a constant function of the electronic density $\rho(\vec{r})$; therefore, the external potential could be displayed as a unique function of the electronic density with the Hamiltonian for the ground state. Thus, the electron number of the system and the external potential could be derived from the electronic density. Furthermore, the physical properties of the solids at ground state could be obtained, with which the ground state energy could be expressed as

$$E[\rho] = E_{Ne}[\rho] + T[\rho] + E_{ee}[\rho] = \int \rho(\vec{r}) V_{Ne}(\vec{r}) d\vec{r} + F_{HK}[\rho] \tag{1.18}$$

$$with\ F_{HK}[\rho] = T[\rho] + E_{ee}[\rho]$$

Therefore, containing the kinetic energy of both the electron-electron interaction and the non-interaction particles, the functional $F_{HK}[\rho]$ can be expressed by the electronic density. As the importance part of the density functional theory, the functional $F_{HK}[\rho]$ would be used to settle the Schrödinger equation. The electron-electron interaction contains two parts: the classical part $J[\rho]$ which named as the self-interaction correction and the non-classical contribution $E_{ncl}[\rho]$ which named as the exchange and Coulomb correlation. Therefore, the expression of the functionals $T[\rho]$ and $E_{ncl}[\rho]$ becomes the most challenging part in the density functional theory. The functional $F_{HK}[\rho]$ can be used to display the solids at the ground state. When the input of the ground state density is used as the density in the theory, it could be shown as

$$E_0 \leq E[\tilde{\rho}] = T[\tilde{\rho}] + E_{Ne}[\tilde{\rho}] + E_{ee}[\tilde{\rho}] \tag{1.19}$$

Therefore, when the trial density is satisfied with the boundary condition ($\tilde{\rho}(\vec{r}) \geq 0$, $\int \tilde{\rho}(\vec{r})\, d\vec{r} = N$,) and related to the external potential, the ground state energy E_0 could be obtained from the equation as discussed above, in which the ground state density would also be solved by the Thomas-Fermi model.

From now on, for the solid which would be solved by the quantum physics, the physical properties could be obtained by the external potential and the density at the ground state. For the ground state energy, the density ρ could be obtained through the function as below,

$$\int \rho(\vec{r}) V_{ext} d\vec{r} + E_{HK}[\rho] \tag{1.20}$$

The minimum ground state energy could be obtained when the ground state density input as the initial density, *i.e.* $\tilde{\rho}(\vec{r}) \equiv \rho(\vec{r})$. Then, the variation principle could only be used for the ground state. It is hard to express it for the solid at the excited state. Hence, the functional $E_{HK}[\rho]$ becomes the essential point for the solving of the density functional theory.

1.3.4 the Kohn-Sham equations

According to Hohenberg and Kohn theorem, the ground state energy of a system can be written out as below,

$$E_0 = min_{\rho \to N} \left(F[\rho] + \int \rho(\vec{r}) V_{Ne}(\vec{r}) d\vec{r} \right) \tag{1.21}$$

Concerning to the contribution of the kinetic energy, the classical Coulomb interaction and the non-classical portion could be covered into the functional $F[\rho]$:

$$F[\rho] = T[\rho] + J[\rho] + E_{ncl}[\rho] \tag{1.22}$$

As the Thomas-Fermi model is limited to the expression of the kinetic energy, the main issue to solve the function is still focused on finding out the expression of the $T[\rho]$ and $E_{ncl}[\rho]$. The Kohn-Sham proposes the expression of it by using the self-consistent one-electron Schrödinger

equations replacing the many-electron problem in 1965 [72,73]. They suggested that the non-interacting reference system should be calculated by the real density for the kinetic energy,

$$T_S = -\frac{1}{2}\sum_{i}^{N}\langle\psi_i|\nabla^2|\psi_i\rangle \qquad \rho_S(\vec{r}) = \sum_{i}^{N}\sum_{s}|\psi_i(\vec{r},s)|^2 = \rho(\vec{r}) \tag{1.23}$$

The orbitals of the non-interacting system are expressed as ψ_i. T_S is the false kinetic energy. The separation of the functional $F[\rho]$ is introduced by the Kohn-Sham equation,

$$F[\rho] = T_S[\rho] + J[\rho] + E_{XC}[\rho] \tag{1.24}$$

Where $E_{XC}[\rho]$ is the exchange-correlation energy. Therefore, the interacting system could be expressed by considering the separation, as follows,

$$E[\rho] = T_S[\rho] + J[\rho] + E_{XC}[\rho] + E_{Ne}[\rho] \tag{1.25}$$

$$E[\rho] = T_S[\rho] + \frac{1}{2}\int\int\frac{\rho(\vec{r}_1)\rho(\vec{r}_2)}{r_{12}}\,d\vec{r}_1 d\vec{r}_2 + E_{XC}[\rho] + \int V_{Ne}\rho(\vec{r})d\vec{r} \tag{1.26}$$

Then the only inexplicit part is $E_{XC}[\rho]$ and the wave functions is $\psi_i(\vec{r})$.

The one-body Hamiltonian was introduced by the Kohn-Sham equation through interpretation, but without being justified. As the approximation method has to be applied to find out the exact expression of the $E_{XC}[\rho]$, many of researches have been focused on the approximation methods to describe the exchange and correction energies.

1.3.5 Methods for solving the Kohn-Sham Equation

The development of solving the Kohn-Sham equations by the more efficient and accurate method is the biggest challenge for computational materials science. The solving of the Kohn-Sham equation can be implemented by the approximation method which could offer the basic knowledge of the physical properties in the fixed crystal structure. But, the calculation of the energy or the distortion of the structures needs much higher accuracy.

There are mainly three methods to solve this problem.

Firstly, by keeping in the interstitial region, the full-potential could describe the localized bonds, and the pseudopotential of the nuclei could be expressed by the approximation Coulomb potential, which could also be given almost the same properties of both the physical and chemical properties compared with the all-electron full potential method [74].

Secondly, the pseudopotential method could be implemented to fulfill the solving of the interaction between the nuclei and the valence electrons, and the gradient level description or the exact localized density could be executed for the solids [75–83].

In practice, the finite number of the basic functions by a linear combination could be used to express the wave function $\psi_i(\vec{r})$. The efficient pseudopotential could be used to explain the electronic-ion interaction by using the Hamiltonian formalism because the physical properties are dependent on the valence electrons instead of the core electrons. The pseudopotential approximation removes the core electrons and replaces them by the pseudo wave functions to represent the true valence waves functions. The functions of the valence wave, the corresponding pseudopotential and the pseudo wave functional are displayed in Fig. 1.4. The screened pseudopotential, which is determined by the empirical, and the self-consistently screened ab initio pseudopotentials make the pseudopotential method use generalized in the solid [65]. The energy could be solved by the one-particle equations and evaluated by the density functional expression which could be used to describe the physical properties of the solid systems.

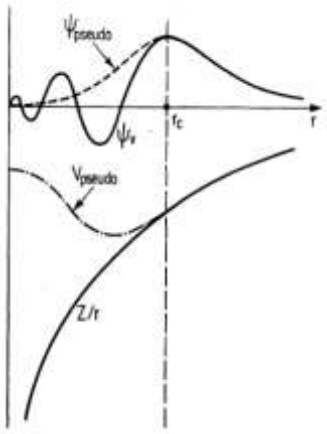

Fig. 1.4 All-electron (solid lines) and pseudoelectron (dashed lines) potentials with the corresponding wave function, respectively. The r_c is the radius of all-electron and pseudoelectron values [106].

Thirdly, the muffin-tin approximation can also be employed as the Kohn-Sham methods which could give reasonable effective and electronic density and can be defined as the Full Charge Density technique [84,85]. Due to the limitation, it could only be used to the density packed systems. The atomic-like around the core sites and almost fewer changes are the reason that the approximation could be used, which leads the spherically symmetrical potential center and the interstitial region to express the Kohn-Sham potentials. The standard Korringa-Kohn-Rostoker (KKR) [86,87], screened-KKR [88] and the Atomic Sphere Approximation(ASA) [89–92] are all the Muffin-tin approximation. The developed muffin-tin formalism is the Exact Muffin-tin Orbitals (EMTO) theory which could solve the optimized overlapping muffin-tin (OOMT) potential more accurately within the single-electron equation.

The exact physical property will decide the computational accuracy within the Kohn-Sham method. The fixation crystal structure and the lattice distortion with the changed energy would require different computational accuracy and computational consumption. Besides these, the computational expenses differ from different computational methods both in the accuracy and efficiency. The full-potential method is the most accurate method but with the most expensive computational resource cost, and could be replaced by the pseudopotential method which solves

the Kohn-Sham equation only by the valence electrons [93–97]. As the full-potential method is mainly focused on the bonding within the interstitial region, the pseudopotential could replace the Coulomb-like potential with enough accuracy and the property results are almost consistent with the results of the full-potential methods [74]. In the present work, the calculations are implemented using the pseudopotential method by the Vienna Ab-initio Simulation Package (VASP) [93,98,99] and the full-charge method, the muffin-tin approximation by the Exact Muffin-tin Orbital theory combined with the Coherent Potentials Application (EMTO-CPA) [100–103].

1.3.5.1 Plane wave in combination with Pseudopotential approximations

The ab-initio could be implemented by the VASP using the Ultra-Soft Pseudopotential (USPP) [104–106] or the Projector-Augmented Wave (PAW) [107] methods with a plane wave basis set, which could be used to reduce the plane wave number of per atom for the transition metals. The ground state could be obtained by the relaxation of the atoms by the forces and the full stress tensor.

The wave functions of the electrons could be expanded by the plane waves, as demonstrated in the Blöch's theorem states, however, the plane wave basis set could not be suitable to be employed to expand the electronic waves due to the huge number of plane waves needed for the bound core orbitals and the initial oscillation of the wave functions near the core. Therefore, to perform the all-electron calculation, a large plane wave basis is needed and a huge computational time is required. However, a smaller plane wave basis setting is needed to describe the electronic wave functions under the pseudopotential approximation. So the calculation of the physical properties is focused on the pseudo-potential-based electronic structure simulation.

1.3.5.2 the EMTO-CPA effective potential

In spite of using the pseudopotential approximation of the Schrödinger equation to obtain the physical properties, there is another approach to obtain the physical properties through the

electronic spectrum through solving the Green function [108–110], which could be employed to obtain the Hamiltonian formalism of both the ordered systems and the disordered systems. The Green function could be used to implement the muffin-tin methods, which could be obtained from the electronic structure by coherent potential. The well-developed full-charge density is the extra muffin-tin orbital method which could obtain the overlapping muffin-tin potential for each single sublattice of the alloys. By combining the coherent potential approximation into the extra muffin-tin orbital (EMTO) approach, the spherical potential could be simulated by the averaged Green function for each alloy component. The charge densities of the electronic and the protonic with the electrostatic potential could be component dependent due to the inside and the outside charges from the potential sphere. Employing the Screened Impurity Model (SIM), the charge misfit of the spherical potentials are included [111,112], and the total potential inside the potential sphere of the alloys are calculated with the total intracellular potential by the Madelung potential, the Spherical Cell Approximation and the SIM corrections. Then, the average interstitial potential which is obtained from the spherical potential can be used to obtain the interstitial potential within the SCA.

As an efficient method, the EMTO could be employed to solve the Kohn-Sham equation in the frame of the density functional theory, and could be used to describe the exact crystal potential more accurately than the other muffin-tin methods. The formula is as below:

$$E_{tot}=T_s[n]+\sum_R (F_{intraR}[n_R]+E_{xcR}[n_R]+F_{inter}[n]) \qquad (1.27)$$

T_s is Kinetic energy. E_{xcR} is the Exchange-correlation energy. E_{intraR} is the intra-cell energy belongs to the Wigner-Seitz cells at Radium(R) and E_{intra} is the interaction between diffenrent cells. The EMTO approach could be used to calculate not only the one-electron states but also provide the ideal ground state more accurately with the CPA combined for the random alloys.

1.3.6 Exchange-correlation functions

There are two kinds of approximations widely used to provide the exchange-correction parts: the generalized gradient approximation (GGA) and the local density approximation (LDA). The local density approximation (LDA) could solve the extended systems as the most accurate approximation [70,72]. The LDA could map the many-body problem by the one-electron exchange-correlation potential with non-interaction. However, the LDA is limited to some systems, in which: (i) the semiconductors and insulators are underestimated because of the band gaps which could be excited; (ii) the systems with the overbinding, in which the cohesive energies would be severely overestimated and the lattice parameters would be underestimated; (iii) the magnetic and the strongly correlated systems; (iv) Van der Waals interactions are not described in the LDA properly, although there are some recent suggestions for overcoming this problem [113,114].

Then, due to the limitation of the local density approximation on the exchange-correlation functional, the generalized gradient approximation (GGA) has been proposed by Perdrew et. al [115–117]. The gradient of the electron density shows an explicit dependence, and could be widely used to the systems, where the LDA has limitations by correction of the overbinding [93,118] and the correction of the magnetic ground states, especially for the ferromagnetic [119] and the antiferromagnetic systems [120], which would offer the improvement of the magnetic moments for the systems with strong localization and correction.

1.4 Motivation and objectives

In the last decades, the experimental method has been employed to study the physical properties of the Ni-Mn-In alloys. However, compared with the theoretical method, there are many limitations, including the high cost and the time-consuming. In computational materials science, we could simulate:

1) the preferred substitution positions of the extra Mn and the effect of the Mn concentration on the preference of the martensite phases with any designed compositions by analysis of the ground state energies and the electronic structures. That could provide useful guidance for the Ni-Mn-In off-stoichiometric alloys design with different structures for experiments and practical applications;
2) the entropy change (including the vibrational, electronic excitation and magnetic entropies) of any desired Mn concentrations at a temperature, which cannot be obtained from the experiments. The simulation of the entropy could give prediction for the experimental martensitic transformation variation.

Based on this background, we have been oriented to investigate the phase stability by the ground state properties (including the formation energy, electronic structures, and the elastic constants of ground states at 0K), and the thermal excited contributions (including the vibrational, electronic excitation and magnetic contributions at finite temperatures) of the austenite and the martensite phases in stoichiometric and off-stoichiometric Ni-Mn-In alloys.

1) The effect of effective Coloum and exchange parameters on the phase stability, structural and magnetic properties of the ferromagnetic austenite with $L2_1$ structure of stoichiometric $Ni_{50}Mn_{25}In_{25}$ alloy were simulated using the plane-wave pseudopotential density-functional calculations. The exchange-correlation function was expressed by the Generalized Gradient Approximation (GGA) with the effective Coulomb and exchange U and J parameters by the *Vienna Ab-initio Simulation Package* (VASP).
2) To figure out the effect of the excess Mn atoms on the preference of the martensite structures, the tetragonal distortion was employed in the off-stoichiometric Ni-Mn-In alloys with different Mn contents using the Extra Muffin-tin Orbital combined with the Coherent Potential Approximation (EMTO-CPA). The calculations were conducted with the

optimization of the magnetic structure, where the stoichiometric $Ni_{50}Mn_{25}In_{25}$ alloy was served as the reference. Furthermore, based on the martensitic structure preference results, the phase stability of the tetragonal $L1_0$ and the orthorhombic structures in the ferromagnetic state were compared with the cubic $L2_1$ structure in the off-stoichiometric Ni-Mn-In alloys with different Mn contents. The effect of the Mn concentration on the total magnetic moment was calculated for the three structures in the ferromagnetic state. The antiferromagnetic interaction of tetragonal structures was also analyzed by the magnetic moment of the elements.

3) To figure out the effect of the Mn concentration and thermally excited contributions (including the vibrational, electronic excitation and magnetic contributions) on the phase stability of austenite and martensite from 0 K to finite temperatures of the $Ni_{50}Mn_xIn_{50-x}$ alloys, 5 different Mn contents for the austenite and the martensite were calcualted at finite temperatures. The phase stabilities of the ground state of the austenite with an ordered $L2_1$ structure and the martensite with a non-modulated (NM) tetragonal $L1_0$ structure were studied by the formation energies at 0 K. The temperature excitation entropic contributions (including vibrational and electronic) were calculated at different Mn contents. The relationship between the magnetic moment variation and the Mn concentration were also analyzed at finite temperatures for the further prediction of the magnetic entropy change tendency.

The objective of the present work is to bridge the gap between the experimental observation and theoretical calculations; provide direct evidence for the explanation of the experimental results of the Ni-Mn-In alloys; reveal the mechanism of the physical properties; lay a solid foundation for the promoting of the current alloys and for the design of the ferromagnetic shape memory alloys. To carry out the calculation, Université de Lorraine and Northeastern University supported the

clusters for the implementation of the Clusters. And to ensure the quality of the calculation, the systems of the supercomputer for both organizations are both using the Portable Batch System (PBS) for the batch job and computer system resource management. and setting 16 cores for one note.

Reference

1. Otsuka, K.; Wayman, C.M. *shape memory materials*; Cambridge University Press, 1998; ISBN 0521663849;9780521663847;
2. Wayman, C.M. *Introduction to the crystallography of martensitic transformations*; Macmillan: New York, 1964;
3. Nishiyama, Z. *Martensitic Transformation*; New York: Academic Press, 1978; ISBN 9780125198509.
4. Kainuma, R.; Oikawa, K.; Ito, W.; Sutou, Y.; Kanomata, T.; Ishida, K. Metamagnetic shape memory effect in NiMn-based Heusler-type alloys. *J Mater Chem* **2008**, *18*, 1837–1842.
5. Mohd Jani, J.; Leary, M.; Subic, A.; Gibson, M.A. A review of shape memory alloy research, applications and opportunities. *Mater Des* **2014**, *56*, 1078–1113.
6. Lobo, P.S.; Almeida, J.; Guerreiro, L. Shape Memory Alloys Behaviour: A Review. *Procedia Eng* **2015**, *114*, 776–783.
7. Sreekumar, M.; Nagarajan, T.; Singaperumal, M. Application of trained NiTi SMA actuators in a spatial compliant mechanism: Experimental investigations. *Mater Des* **2009**, *30*, 3020–3029.
8. Mihálcz, I. Fundamental characteristics and design method for nickel-titanium shape memory alloy. *Period Polytech Mech Eng* **2001**, *45*, 75–86.
9. Mertmann, M.; Vergani, G. Design and application of shape memory actuators. *Eur Phys J*

Spec Top **2008**, *158*, 221–230.

10. Ming, H.W.; L. McD., S. Industrial Applications for Shape Memory Alloys. In Proceedings of the the International Conference on Shape Memory and Superelastic Technolgies, Pacific Grove, California; 2000; Vol. 19, pp. 171–182.
11. Chang, L.C.; Read, T.A. Plastic Deformation and Diffusionless Phase Changes in Metals-the Gold-Cadmium Beta Phase. *JOM* **1951**, *3*, 47–52.
12. Buehler, W.J.; Gilfrich, J. V.; Wiley, R.C. Effect of low-temperature phase changes on the mechanical properties of alloys near composition TiNi. *J Appl Phys* **1963**, *34*, 1475–1477.
13. Hartl, D.J.; Lagoudas, D.C. Aerospace applications of shape memory alloys. *Proc Inst Mech Eng Part G J Aerosp Eng* **2007**, *221*, 535–552.
14. Bil, C.; Massey, K.; Abdullah, E.J. Wing morphing control with shape memory alloy actuators. *J Intell Mater Syst Struct* **2013**, *24*, 879–898.
15. Stoeckel, D. Shape memory actuators for automotive applications. *Mater Des* **1990**, *11*, 302–307.
16. Sun, L.; Huang, W.M.; Ding, Z.; Zhao, Y.; Wang, C.C.; Purnawali, H.; Tang, C. Stimulus-responsive shape memory materials: A review. *Mater Des* **2012**, *33*, 577–640.
17. Menna, C.; Auricchio, F.; Asprone, D. Applications of Shape Memory Alloys in Structural Engineering. In *Shape memory alloy engineering*; Lecce, L., Concilio, A., Eds.; Butterworth-Heinemann, 2015; pp. 369–403 ISBN 9780080999210.
18. Ullakko, K. Magnetically controlled shape memory alloys: A new class of actuator materials. *J Mater Eng Perform* **1996**, *5*, 405–409.
19. Tellinen, J.; Suorsa, I.; Aaltio, I.; Ullakko, K. Basic Properties of Magnetic Shape Memory Actuators. *8th Int Conf ACTUATOR 2002* **2002**, 10–12.
20. Ullakko, K.; Huang, J.K.; Kokorin, V. V.; O'Handley, R.C. Magnetically controlled shape

memory effect in Ni_2MnGa intermetallics. *Scr Mater* **1997**, *36*, 1133–1138.

21. Tickle, R.; James, R.D.; Shield, T.; Wuttig, M.; Kokorin, V. V. Ferromagnetic shape memory in the NiMnGa system. *IEEE Trans Magn* **1999**, *35*, 4301–4310.
22. Murray, S.J.; Marioni, M.; Allen, S.M.; O'Handley, R.C.; Lograsso, T.A. 6% magnetic-field-induced strain by twin-boundary motion in ferromagnetic Ni-Mn-Ga. *Appl Phys Lett* **2000**, *77*, 886–888.
23. Karaca, H.E.; Karaman, I.; Basaran, B.; Lagoudas, D.C.; Chumlyakov, Y.I.; Maier, H.J. On the stress-assisted magnetic-field-induced phase transformation in Ni_2MnGa ferromagnetic shape memory alloys. *Acta mater* **2007**, *55*, 4253–4269.
24. Kainuma, R.; Imano, Y.; Ito, W.; Morito, H.; Sutou, Y.; Oikawa, K.; Fujita, A.; Ishida, K. Metamagnetic shape memory effect in a Heusler-type $Ni_{43}Co_7Mn_{39}Sn_{11}$ polycrystalline alloy. *Appl Phys Lett* **2006**, *88*, 192513.
25. Sozinov, A.; Likhachev, A.A.; Lanska, N.; Ullakko, K. Giant magnetic-field-induced strain in NiMnGa seven-layered martensitic phase. *Appl Phys Lett* **2002**, *80*, 1746–1748.
26. Ullakko, K.; Huang, J.K.; Kantner, C.; O'Handley, R.C.; Kokorin, V. V. Large magnetic-field-induced strains in Ni_2MnGa single crystals. *Appl Phys Lett* **1996**, *69*, 1966–1968.
27. Sutou, Y.; Imano, Y.; Koeda, N.; Omori, T.; Kainuma, R.; Ishida, K.; Oikawa, K. Magnetic and martensitic transformations of NiMnX (X = In, Sn, Sb) ferromagnetic shape memory alloys. *Appl. Phys. Lett.* **2004**, *85*, 4358–4360.
28. Umetsu, R.Y.; Xu, X.; Kainuma, R. NiMn-based metamagnetic shape memory alloys. *Scr Mater* **2016**, *116*, 1–6.
29. Yan, H.; Zhang, Y.; Xu, N.; Senyshyn, A.; Brokmeier, H.G.; Esling, C.; Zhao, X.; Zuo, L.; Liang Zuo; Zuo, L. Crystal structure determination of incommensurate modulated martensite in Ni-Mn-In Heusler alloys. *Acta Mater* **2015**, *88*, 375–388.

30. Krenke, T.; Acet, M.; Wassermann, E.F.; Moya, X.; Mañosa, L.; Planes, A. Ferromagnetism in the austenitic and martensitic states of Ni-Mn-In alloys. *Phys Rev B* **2006**, *73*, 174413.

31. Umetsu, R.Y.; Ito, W.; Ito, K.; Koyama, K.; Fujita, A.; Oikawa, K.; Kanomata, T.; Kainuma, R.; Ishida, K. Anomaly in entropy change between parent and martensite phases in the $Ni_{50}Mn_{34}In_{16}$ Heusler alloy. *Scr mater* **2009**, *60*, 25–28.

32. Pérez-sierra, A.M.; Bruno, N.M.; Pons, J.; Cesari, E.; Karaman, I. Atomic order and martensitic transformation entropy change in Ni-Co-Mn-In metamagnetic shape memory alloys. *Scr mater* **2016**, *110*, 61–64.

33. Kazakov, A.P.; Prudnikov, V.N.; Granovsky, A.B.; Zhukov, A.P.; Gonzalez, J.; Dubenko, I.; Pathak, A.K.; Stadler, S.; Ali, N. Direct measurements of field-induced adiabatic temperature changes near compound phase transitions in Ni-Mn-In based Heusler alloys. *Appl. Phys. Lett.* **2011**, *98*, 131911.

34. Oikawa, K.; Ito, W.; Imano, Y.; Sutou, Y.; Kainuma, R.; Ishida, K.; Okamoto, S.; Kitakami, O.; Kanomata, T. Effect of magnetic field on martensitic transition of $Ni_{46}Mn_{41}In_{13}$ Heusler alloy. *Appl. Phys. Lett.* **2006**, *88*, 122507.

35. Kustov, S.; Corro, M.L.; Pons, J.; Cesari, E. Entropy change and effect of magnetic field on martensitic transformation in a metamagnetic Ni-Co-Mn-In shape memory alloy. *Appl. Phys. Lett.* **2009**, *94*, 191901.

36. Dubenko, I.; Pathak, A.K.; Stadler, S.; Ali, N.; Kovarskii, Y.; Prudnikov, V.N.; Perov, N.S.; Granovsky, A.B. Giant Hall effect in Ni-Mn-In Heusler alloys. *Phys Rev B* **2009**, *80*, 092408.

37. Miyamoto, T.; Ito, W.; Umetsu, R.Y.; Kainuma, R.; Kanomata, T.; Ishida, K. Phase stability and magnetic properties of $Ni_{50}Mn_{50-x}In_x$ Heusler-type alloys. *Scr Mater* **2010**, *62*, 151–154.

38. Chatterjee, S.; Singh, V.R.; Deb, A.K.; Giri, S.; De, S.K.; Dasgupta, I.; Majumdar, S. Magnetic properties of $Ni_{2+x}Mn_{1-x}In$ Heusler alloys: Theory and experiment. *J Magn Magn*

Mater **2010**, *322*, 102–107.

39. Kanomata, T.; Yasuda, T.; Sasaki, S.; Nishihara, H.; Kainuma, R.; Ito, W.; Oikawa, K.; Ishida, K.; Neumann, K.; Ziebeck, K.R.A. Magnetic properties on shape memory alloys $Ni_2Mn_{1+x}In_{1-x}$. *J Magn Magn Mater* **2009**, *321*, 773–776.

40. Karaca, H.E.; Karaman, I.; Basaran, B.; Ren, Y.; Chumlyakov, Y.I.; Maier, H.J. Magnetic field-induced phase transformation in NiMnColn magnetic shape-memory alloys-a new actuation mechanism with large work output. *Adv Funct Mater* **2009**, *19*, 983–998.

41. Kainuma, R.; Imano, Y.; Ito, W.; Sutou, Y.; Morito, H.; Okamoto, S.; Kitakami, O.; Oikawa, K.; Fujita, A.; Kanomata, T.; et al. Magnetic-field-induced shape recovery by reverse phase transformation. *Nature* **2006**, *439*, 957–960.

42. Liu, J.; Gottschall, T.; Skokov, K.P.; Moore, J.D.; Gutfleisch, O. Giant magnetocaloric effect driven by structural transitions. *Nat Mater* **2012**, *11*, 620–626.

43. Umetsu, R.Y.; Kusakari, Y.; Kanomata, T.; Suga, K.; Sawai, Y.; Kindo, K.; Oikawa, K.; Kainuma, R.; Ishida, K. Metamagnetic behaviour under high magnetic fields in $Ni_{50}Mn_{50-x}In_x$ (x= 14.0 and 15.6) shape memory alloys. *J Phys D Appl Phys* **2009**, *42*, 075003.

44. Kainuma, R.; Ito, W.; Umetsu, R.Y.; Khovaylo, V.V.; Kanomata, T. Metamagnetic Shape Memory Effect and Magnetic Properties of Ni-Mn Based Heusler Alloys. *Mater Sci Forum* **2011**, *684*, 139–150.

45. Wang, B.M.; Liu, Y.; Ren, P.; Xia, B.; Ruan, K.B.; Yi, J.B.; Ding, J.; Li, X.G.; Wang, L. Large exchange bias after zero-field cooling from an unmagnetized state. *Phys Rev L* **2011**, *106*, 077203.

46. Sharma, V.K.; Chattopadhyay, M.K.; Shaeb, K.H.B.; Chouhan, A.; Roy, S.B. Large magnetoresistance in $Ni_{50}Mn_{34}In_{16}$ alloy. *Appl. Phys. Lett.* **2006**, *89*, 222509.

47. McCormack, R.; de Fontaine, D. First-principles study of multiple order-disorder transitions

in Cd_2AgAu Heusler alloys. *Phys Rev B* **1996**, *54*, 9746–9755.

48. Khovailo, V.V.; Takagi, T.; Vasil'ev, A.N.; Miki, H.; Matsumoto, M.; R. Kainuma On Order-Disorder (*$L2_1$* -> B2') Phase Transition in $Ni_{2+x}Mn_{1-x}Ga$ Heusler Alloys. *Phys Stat Sol* **2001**, *183*, R1–R3.

49. Zhang, C.Y.; Zhang, Y.D.; Esling, C.; Zhao, X.; Zuo, L. Crystallographic features of the martensitic transformation and their impact on variant organization in the intermetallic compound $Ni_{50}Mn_{38}Sb_{12}$ studied by SEM/EBSD. *IUCrJ* **2017**, *4*, 700–709.

50. Planes, A.; Mãnosa, L.; Acet, M. Magnetocaloric effect and its relation to shape-memory properties in ferromagnetic Heusler alloys. *J Phys Condens Matter* **2009**, *21*, 223201.

51. Krenke, T.; Duman, E.; Acet, M.; Wassermann, E.F.; Moya, X.; Mañosa, L.; Planes, A. Inverse magnetocaloric effect in ferromagnetic Ni-Mn-Sn alloys. *Nat Mater* **2005**, *4*, 450–454.

52. Webster, P.J.; Ziebeck, K.R.A.; Town, S.L.; Peak, M.S. Magnetic order and phase transformation in Ni_2MnGa. *Philos Mag Part B* **1984**, *49*, 295–310.

53. Brown, P.J.; Neumann, K.-U.; Ziebeck, K.R.A.; Bargawi, A.Y.; Crangle, J. Direct observation of a band Jahn-Teller effect in the martensitic phase transition of Ni2MnGa Redistribution of magnetization in the martensitic transitionof V_3Si Direct observation of a band Jahn-Teller effect in the martensitic phase transition of Ni. *J Phys Condens Matter* **1999**, *11*, 4715–4722.

54. Şaşıoğlu, E.; Sandratskii, L.M.; Bruno, P. First-principles calculation of the intersublattice exchange interactions and Curie temperatures of the full Heusler alloys Ni_2MnX (X = Ga, In, Sn, Sb). *Phys Rev B* **2004**, *70*, 024427.

55. Priolkar, K.R.; Bhobe, P.A.; Lobo, D.N.; D'Souza, S.W.; Barman, S.R.; Chakrabarti, A.; Emura, S. Antiferromagnetic exchange interactions in the $Ni_2Mn_{1.4}In_{0.6}$ ferromagnetic

Heusler alloy. *Phys Rev B* **2013**, *87*, 144412.

56. Krenke, T.; Duman, E.; Acet, M.; Wassermann, E.F.; Moya, X.; Mañosa, L.; Planes, A.; Suard, E.; Ouladdiaf, B. Magnetic superelasticity and inverse magnetocaloric effect in Ni-Mn-In. *Phys Rev B* **2007**, *75*, 104414.

57. Umetsu, R.Y.; Fujita, A.; Ito, W.; Kanomata, T.; Kainuma, R. Determination of the magnetic ground state in the martensite phase of Ni-Mn-Z (Z = In, Sn and Sb) off-stoichiometric Heusler alloys by nonlinear AC susceptibility. *J Phys Condens Matter* **2011**, *23*, 326001.

58. Şaşıoğlu, E.; Sandratskii, L.M.; Bruno, P. Role of conduction electrons in mediating exchange interactions in Mn-based Heusler alloys. *Phys Rev B* **2008**, *77*, 064417.

59. Parr, R.G. Density functional theory of atoms and molecules. In *Horizons of Quantum Chemistry*; Fukui K., P.B., Ed.; Springer Netherlands: Dordrecht, 1980; pp. 5–15.

60. Chatterjee, A. Density Functional Theory. In *Structure Property Correlations for Nanoporous Materials*; Boca Raton: CRC Press, 2010; p. 22.

61. Hartree, D. The wave mechanics of an atom with a non-coulomb central field. Part I. theory and methods. *Proc Camb Phil Soc* **1927**, *24*, 89–110.

62. Fock, V. Näherungsmethode zur Lösung des quantenmechanischen Mehrkörperproblems. *Zeit für Phys* **1930**, *61*, 126–148.

63. Payne, M.C.; Teter, M.P.; Allan, D.C.; Arias, T.A.; Joannopoulos, J.D. Iterative minimization techniques for ab initio total-energy calculations molecular dynamics and conjugate gradients. *Rev Mod Phys* **1992**, *64*, 1045–1097.

64. Joannopoulos, J.D. Predicting the structure of solids. In *Physics of Disordered Materials*; Adler, D., Fritzsche, H., Ovshinsky, S.R., Eds.; Plenum Press: New York and London, 1985; p. 19 ISBN 9781461295198.

65. Pickett, W.E. Pseudopotential methods in condensed matter applications. *Comput Phys*

Reports **1989**, *9*, 115–197.

66. Weinstein, H.; Politzer, P.; Srebrenik, S. A misconception concerning the electronic density distribution of an atom. *Theor Chim Acta* **1975**, *38*, 159–163.
67. Wang, W.P. Fixed-shell statistical atomic models with piecewise exponentially decaying electron densities. *Phys Rev A* **1982**, *25*, 2901–2912.
68. Thomas, L.H. The calculation of atomic fields. *Proc Camb Phil Soc* **1927**, *23*, 542.
69. Fermi, E.; Rasetti, F. Eine messung des verhältnisses h/k durch die anomale dispersion des thalliumdampfes. *Zeitschrift für Phys* **1927**, *43*, 379–383.
70. Hohenberg, P.; Kohn, W. Inhomogeneous electron gas. *Phys Rev* **1964**, *136*, 864–871.
71. Cuevas, J. C.; Patil, P.. S. introduction of density functional theory(slides). *Tetrahedron Lett* 1989, *30*, 5841–5844.
72. Kohn, W.; Sham, L.J. Self-consistent equations including exchange and correlation effects. *Phys Rev* **1965**, *140*, 1133–1138.
73. Lundqvist, S.; March, N.H. *Theory of the inhomogeneous electron gas*; Springer US: Boston, MA, 1983; ISBN 978-1-4899-0417-1.
74. Kiejna, A.; Kresse, G.; Rogal, J.; De Sarkar, A.; Reuter, K.; Scheffler, M. Comparison of the full-potential and frozen-core approximation approaches to density-functional calculations of surfaces. *Phys Rev B* **2006**, *73*, 035404.
75. Slater, J.C. Wave Functions in a Periodic Potentia. *Phys Rev* **1937**, *51*, 846–851.
76. Andersen, O.K. Linear methods in band theory. *Phys Rev B* **1975**, *12*, 3060–3083.
77. Singh, D.J. *Planewaves, pseudopotentials and the LAPW method*; Kluwer Academic Publishers: Bosten, 1994; ISBN 9780387296845.
78. Dederichs, P.H.; Drittler, B.; Zeller, R. A Full-Potential KKR Green's Function Method for Impurities in Metals. *MRS Proc* **1991**, *253*, 185.

79. Sha, X.; Cohen, R.E. First-principles studies of electrical resistivity of iron under pressure. *J Phys Condens Matter* **2011**, *23*, 075401.

80. Fiorentini, V.; Methfessel, M. Extracting convergent surface energies from slab calculations. *J Phys Condens Matter* **1996**, *8*, 6525–6529.

81. Wills, J.M.; Cooper, B.R. Synthesis of band and model Hamiltonian theory for hybridizing cerium systems. *Phys Rev B* **1987**, *36*, 3809–3823.

82. Liu, X.; Wang, Y.; Eisenbach, M.; Malcolm Stocks, G. A full-potential approach to the relativistic single-site Green's function. *J Phys Condens Matter* **2016**, *28*, 355501.

83. Papanikolaou, N.; Zeller, R.; Dederichs, P.H.; Stefanou, N. Ab initio study of structural distortion and its influence on the magnetic properties of metallic dilute alloys. *Comput Mater Sci* **1997**, *8*, 131–135.

84. Kollár, J.; Vitos, L.; Skriver, H.L. From ASA Towards the Full Potential. In *Electronic Structure and Physical Properies of Solids*; Springer Berlin Heidelberg: Berlin, Heidelberg, 1999; pp. 85–114.

85. Vitos, L.; Kollár, J.; Skriver, H. Full charge-density scheme with a kinetic-energy correction: Application to ground-state properties of the 4d metals. *Phys Rev B* **1997**, *55*, 13521–13527.

86. Korringa, J. On the calculation of the energy of a Bloch wave in a metal. *Physica* **1947**, *13*, 392–400.

87. Kohn, W.; Rostoker, N. Solution of the Schrödinger Equation in Periodic Lattices with an Application to Metallic Lithium. *Phys Rev* **1954**, *94*, 1111–1120.

88. Szunyogh, L.; Újfalussy, B.; Weinberger, P.; Kollár, J. Self-consistent localized KKR scheme for surfaces and interfaces. *Phys Rev B* **1994**, *49*, 2721–2729.

89. Skriver, H.L. *The LMTO method*; Springer-Verlag Berlin Heidelberg, 1984;

90. Andersen, O.K.; Jepsen, O.; Sob, M. Linearized band structure methods. In *Electronic Band*

Structure and Its Applications; Springer Berlin Heidelberg: Berlin, Heidelberg, 1987; pp. 1–57.

91. Tôru Moriya The theory of itinerant electron magnetism. *J Magn Magn Mater* **1991**, *100*, 261–271.
92. Asato, M.; Settels, A.; Hoshino, T.; Asada, T.; Blügel, S.; Zeller, R.; Dederichs, P.H. Full-potential KKR calculations for metals and semiconductors. *Phys Rev B* **1999**, *60*, 5202–5210.
93. Kresse, G.; Furthmüller, J. Efficient iterative schemes for ab initio total-energy calculations using a plane-wave basis set. *Phys Rev B* **1996**, *54*, 11169–11186.
94. Bachelet, G.B.; Hamann, D.R.; SchÏter, M. Pseudopotentials that work: From H to Pu. *Phys Rev B* **1982**, *26*, 4199–4228.
95. Hartwigsen, C.; Goedecker, S.; Hutter, J. Relativistic separable dual-space Gaussian pseudopotentials from H to Rn. *Phys Rev B* **1998**, *58*, 3641–3662.
96. Cohen, M.L. The pseudopotential panacea. *Phys Today* **1979**, *32*, 40–47.
97. Phillips, J.C. Energy-Band Interpolation Scheme Based on a Pseudopotential. *Phys Rev* **1958**, *112*, 685–695.
98. Kresse, G.; Furthmüller, J. Efficiency of ab-initio total energy calculations for metals and semiconductors using a plane-wave basis set. *Comput Mater Sci* **1996**, *6*, 15–50.
99. Hafner, J. Atomic-scale computational materials science. *Acta mater* **2000**, *48*, 71–92.
100. Vitos, L. Total-energy method based on the exact muffin-tin orbitals theory. *Phys Rev B* **2001**, *64*, 014107.
101. Vitos, L.; Skriver, H.L.; Johansson, B.; Kollár, J. Application of the exact muffin-tin orbitals theory: the spherical cell approximation. **2000**, *18*, 24–38.
102. Vitos, L. *Computational quantum mechanics for materials engineers: the EMTO method*

and applications; Springer US: Boston, MA, 2005; ISBN 9781846289507.

103. Vitos, L.; Abrikosov, I.A.; Johansson, B. Coherent Potential Approximation within the Exact Muffin-Tin Orbitals theory. In *Complex Inorganic Solids*; Springer US: Boston, MA, 2005.

104. Vanderbilt, D. Soft self-consistent pseudopotentials in a generalized eigenvalue formalism. *Phys Rev B* **1990**, *41*, 7892.

105. Shu, J.; Kresse, G. Norm-conserving and ultrasoft pseudopotentials for first-row and transition elements. *J Phys Condens Matter* **1994**, *6*, 8245–8257.

106. Kresse, G.; Joubert, D. From ultrasoft pseudopotentials to the projector augmented-wave method. *Phys Rev B* **1999**, *59*, 1758–1775.

107. Blöchl, P.E. Projector augmented-wave method. *Phys Rev B* **1994**, *50*, 17953–17979.

108. Rickayzen, G. *Green's functions and condensed matter*; Academic Press, 1980; ISBN 0125879504.

109. Gonis, A. *Green functions for ordered and disordered systems*; North-Holland, 1992; ISBN 0444889868.

110. Weinberger, P. *Electron scattering theory for ordered and disordered matter*; Clarendon Press, 1990; ISBN 9780198520252.

111. Ruban, A. V; Abrikosov, I.A. Configurational thermodynamics of alloys from first principles: effective cluster interactions. *Reports Prog Phys* **2008**, *71*, 046501.

112. Korzhavyi, P.A.; Ruban, A. V.; Abrikosov, I.A.; Skriver, H.L. Madelung energy for random metallic alloys in the coherent potential approximation. *Phys Rev B* **1995**, *51*, 5773–5780.

113. Andersson, Y.; Andersson, D.C.; Lundqvist, B.I. Van der Waals interactions in density-functional theory. *Phys Rev Lett* **1996**, *76*, 102–105.

114. Kohn, W.; Meir, Y.; Makarov, D.E. Van der Waals energies in density functional theory.

Phys Rev L **1998**, *80*, 4153–4156.

115. Perdew, J.P. Generalized gradient approximation for the fermion kinetic energy as a functional of the density. *Phys Lett A* **1992**, *165*, 79–82.

116. Perdew, J.P.; Burke, K.; Ernzerhof, M. Generalized gradient approximation made simple. *Phys Rev Lett* **1996**, *77*, 3865–3868.

117. Perdew, J.P.; Ruzsinszky, A.; Csonka, G.I.; Vydrov, O.A.; Scuseria, G.E.; Constantin, L.A.; Zhou, X.; Burke, K. Restoring the density-gradient expansion for exchange in solids and surfaces. *Phys Rev L* **2008**, *100*, 136406.

118. Seifert, K.; Hafner, J.; Furthmuller, J.; Kresse, G. The influence of generalized gradient corrections to the LDA on predictions of structural phase stability: The Peierls distortion in As and Sb. *J Phys Condens Matter* **1995**, *7*, 3683–3692.

119. Leung, T.C.; Chan, C.T.; Harmon, B.N. Ground State properties of Fe, Co and Ni and their momoxides: results of the greneralzied gradient approxiamtion. *Phys* **1991**, *44*, 2923–2927.

120. Asada, T. Electronic structures and magnetism of α and β Mn. *J Magn Magn Mater* **1995**, *140–144*, 47–48.

Chapter 2 Effect of effective Coulomb and exchange parameters on phase stability, structural and magnetic properties of $Ni_{50}Mn_{25}In_{25}$ alloys

2.1 Outline

In this chapter, we revealed the crystal structure, the phase stability and the electronic structures of the ferromagnetic austenite with cubic *L2₁* structure in the stoichiometric $Ni_{50}Mn_{25}In_{25}$ alloy under the frame of density-functional theory using the plane-wave pseudopotential calculations considering the Hubbard *U* and *J* coupling parameter into exchange-correlation by the *Vienna Ab-initio Simulation Package* (VASP). We first investigated the effective Coulomb and exchange *U* and *J* parameters on phase stability, structural and magnetic properties of the ordered austenite of the $Ni_{50}Mn_{25}In_{25}$ alloy with. When the Hubbard *U* and *J* coupling was added into the first principle calculations, the lattice parameter and the ground state energy vary with the different *U* and *J* coupling in the cubic *L2₁* austenite of the $Ni_{50}Mn_{25}In_{25}$ alloy. The bulk modulus and elastic constants, which were obtained by the Equation of States (EOS) and the shear strain method, respectively, were affected by the Hubbard *U* and *J* parameter of the austenite $Ni_{50}Mn_{25}In_{25}$ alloy. With the results of the parameter test, we thoroughly compared the physical properties, including the formation energy and the electronic structure, which were obtained with and without the effective Coulomb and exchange parameters. The electronic structure was given by the band structure and the density of states (DOS). The charge density difference was also investigated with the Hubbard *U* and *J* parameter added into the first principle calculations. And we analyzed the physical property results and compared them with the principle function of their definition.

2.2 Introduction

As a type of magnetic actuator materials, ferromagnetic shape memory alloys attract intensive attention because of the shape memory effect, which is originated from the magnetic field-induced strain [1]. There are two kinds of ferromagnetic Ni-Mn-based shape memory alloys, i) the Ni-Mn-Ga alloy, ii) the Ni-Mn-X alloy (X: In, Sb, Sn). The Ni-Mn-Ga alloy represents a magnetic field-induced strain, which is larger than 5% as reported in the previous researches [2,3]. Whereas, the wide usage of the Ni-Mn-Ga alloy is limited as it has a low Curie temperature (T_C) and low martensitic transition temperature (M_S) [4]. As shown in the phase diagram, the Ni-Mn-X alloys (X: In, Sn and Sb) have a higher martensitic transformation temperature, which is compositional dependent and could increase with the decreasing In, Sn and Sb contents [1,5,6]. They also have a large magnetic field-induced strain at the same time, which are originated from its thermal transition from the cubic ferromagnetic austenite to the modulated weak-ferromagnetic martensite [1].

As the crystal structure of the Ni-Mn-In alloys are crucial for understanding the mechanism of the martensite transition process which would result in shape memory effect, the crystal structure of phases have been largely investigated through experimental methods, such as X-ray diffraction (XRD), neutron diffraction (ND) and TEM selected area electron diffraction (SAED) [1,7–13]. A ternary Ni-Mn-In alloy usually could have the austenite phase with cubic $L2_1$ structure (space group, *Fm-3m*), the non-modulated martensite phase with tetragonal $L1_0$ structure [7] and the monoclinic modulated martensite phase with *6M* (space group, *P2/m*, with β = 93.044°) [13], *10M* [7] or *4O* [14] structure. As shown in Fig. 2.1, the lattice orientation relationship of the austenite and the martensite could be expressed by the Bain model, $[1\ 1\ 0]_A$ // $[1\ 0\ 0]_M$, $[0\ 0\ 1]_A$ // $[0\ 1\ 0]_M$, $[1\ \text{-}1\ 0]_A$ // $[0\ 0\ 1]_M$ [13]. In order to understand the physical mechanism of the shape memory effect, which

is induced by a magnetic field, the study of the electronic structure and the magnetic property of different structures is essential. As discovered in the previous research, the ferromagnetism of the alloys was discovered to be mainly attributed to the indirect *d-d* coupling of the Mn-Mn atoms, which would contribute to the magnetic properties of the alloys [15]. However, there is relatively scarce analysis of the origin of the magnetic properties in the experimental studies.

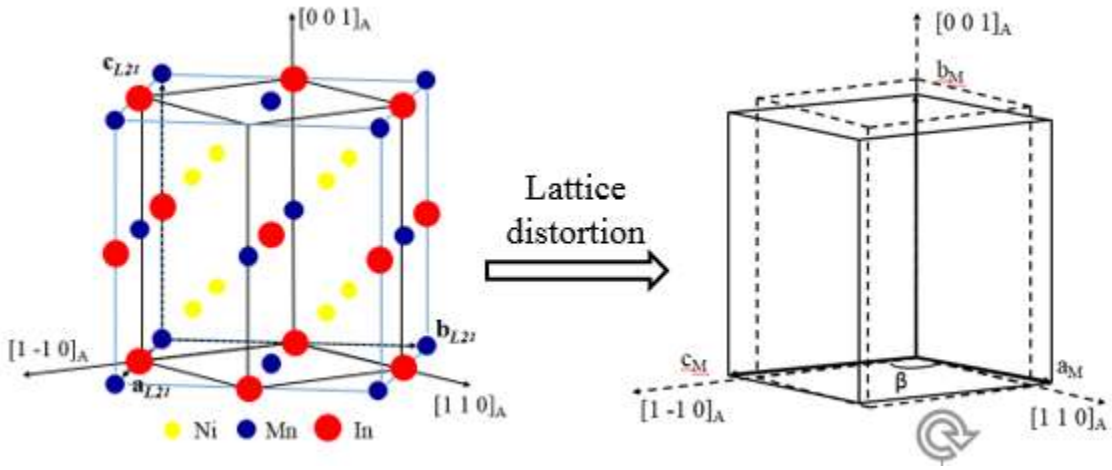

Fig. 2.1 Orientation relationship between the cubic $L2_1$ austenite (A) and the martensite (M), constructed under the Bain model [13].

As the Hubbard *U* parameter stands for the onsite Coulomb repulsion between two electrons of one atom [16] and could describe the electronic properties of the materials with exotic magnetism in reasonable situation [17], the combination of the Hubbard *U* parameter with the conventional first principle calculations could be used to take the Coulomb and exchange-correlation, which are orbital dependent, into consideration during the analysis of the electronic structure and the magnetic properties for the transition metal with the strong correction of *d* or *f* electrons [18–20]. The Hubbard *U* parameter is the required energy, which is used to move an electron from one atom to another assuming that the atoms are all embedded in a polarized surrounding. It is equivalent to the difference between ionization potential and electron affinity in

solids [21]. Moreover, the ground state energy could be lowered by removing an electron, which would lead to a polarization of its surroundings [22]. Therefore, the Hubbard parameter U is considered into the calculation of the ordered austenite stoichiometric $Ni_{50}Mn_{25}In_{25}$ alloys for a more accurate analysis of the ground state energy and the magnetic properties by employing the *Generalized Gradient Approximation* exchange-correlation (*GGA + U*) method [18]. In this method, the correlation effects for on-site Coulomb repulsion between the localized *3d* states of Mn and Ni would be considered.

As reported in the literature, the elastic constants are associated to the interatomic bonding characterization between the adjacent atomic planes and the anisotropic character of the bonding [23,24], therefore, it could be used to predict the mechanism of the phase stability [25–27]. For the cubic $L2_1$ structure, it has three independent elastic constants C_{11}, C_{12} and C_{44}, which can be obtained from the bulk modulus [28] and distortion methods [29,30]. For the cubic $Ni_{50}Mn_{25}In_{25}$ austenite, *i.e.*, the ordered $L2_1$ structure, the mechanical stability conditions can be evaluated with the conditions below,

$$C_{44} > 0, \quad C_{11} - |C_{12}| > 0 \quad \textit{and} \quad C_{11} + 2 * C_{12} > 0$$

As the elastic constants stand for phase ability to respond to the external forces [26], the elastic constants could be derived by the stress-strain relationship, which could be obtained from the ground state energy calculations as a function of crystal deformation by the *ab-initio* method [31]. The elastic constants, as the second derivatives of the total energy [32], could be derived from the total energy of the crystal around the equilibrium volume by a truncated Taylor expansion of the strain components [33,34].

2.3 Computational method

First-principle calculations were implemented by the *Vienna Ab-initio Simulation Package* (VASP) within the framework of Density Functional Theory (DFT) [35–37]. The Projector Augmented Wave method (PAW, [38,39]) was employed as an efficient method with high accuracy computational ability for the transition elements, *i.e.*, Ni and Mn. Atom relaxation was carried out by a conjugate gradient algorithm. The Methfessel Paxton smearing method with smearing width 0.2 eV was applied to determine the occupation of the electronic states in alloys with highly accurate force and energy [40], which was recommended in the VASP documentation. The preliminary calculations were executed using the *Generalized Gradient Approximation* (*GGA*) of Perdew, Burke and Ernzerhof (*PBE*) [41]. The electronic convergence threshold with 10^{-4} eV per unit cell was used for the structural relaxation. With the setting of the total energy difference and the total- and atomic- force changes to be within 1meV/atom and 0.02 eV/Å, respectively, the atom position and the lattice parameters were optimized for all structures to obtain the equilibrium state. The electronic configurations (Ni ($3d^8 4s^2$), Mn ($3d^6 4s^1$) and In ($5s^2 5p^1$)) were employed. The ground states of pure Ni, pure Mn and the pure In metals were calculated using the $L2_1$ structure for formation energy calculation of the Ni-Mn-In alloy. Firstly, to ensure the quality of the calculations, the calculation parameters, including the cut-off energy (*ENCUT* values) and the k-point grid, were obtained through a series of tests by the full-relaxation (optimizing the cell and ionic). The tests were implemented by a series of total energy calculations with various kinetic energy cutoff radii (*ENCUT* values) combined with different k-point meshes for the stoichiometric Ni-Mn-In alloy in the primitive cell. The test results are shown in Table 2.1 and Fig. 2.2. We could obtain that, for the *ENCUT* value tests, the different k-point meshes do not affect the convergence trend of the energy difference tendency. However, the energy difference varies with the different

ENCUT values, and it decreases before 320eV, then increases with *ENCUT* value and keeps stable after 420 eV. When the *ENCUT* value reaches 420 eV and the k-points use 10 × 10 × 10 point grids, the energy difference begins to be less than 1 meV/atom, as shown in Table 2.1. Therefore, all the calculations would be calculated using spin polarization with an energy cut-off of 420 eV for further physical properties calculation and the Monkhorst-Pack [42] with 12 × 12 × 12 (for 4-atom cell of austenitic primitive cell) k-point meshes were applied for the integration of Brillouin zone.

Table 2.1 Convergence test with different kinetic energy cutoff radii (*ENCUT* values) and k-point grid combination for primitive cell of stoichiometric $Ni_{50}Mn_{25}In_{25}$ alloy

k-point grids	Number of k-points	270 eV	320 eV	370 eV	420 eV	470 eV
4x4x4	10	0.025410	0.005323	0.019322	0.023782	0.023749
6x6x6	28	-0.001088	-0.021158	-0.007386	-0.002631	-0.002722
8x8x8	60	0.004087	-0.016157	-0.002394	0.002306	0.002278
10x10x10	110	0.001461	-0.018870	-0.005027	-0.000361	-0.000440
12x12x12	182	0.001584	-0.018510	-0.004704	-0.000028	-0.000074
14x14x14	280	0.001419	-0.018729	-0.004942	-0.000256	-0.000311
16x16x16	408	0.001823	-0.018432	-0.004610	0.000058	0.000000

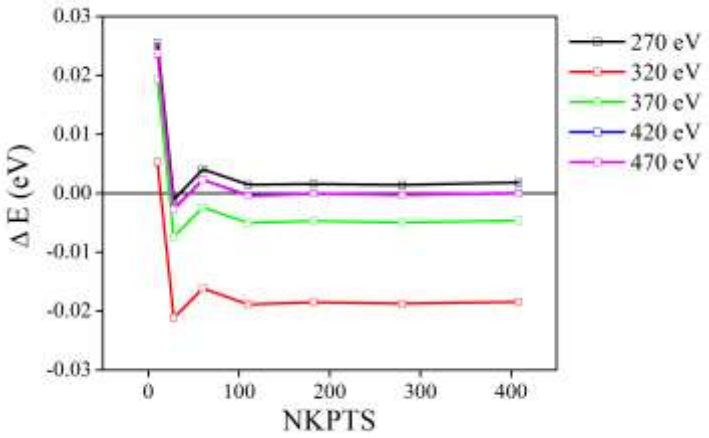

Fig. 2.2 VASP convergence test, including energy cut-off (*ENCUT* value) and k-point (KPTS) parameters based on energy difference within 10^{-4} eV/atom.

Furthermore, the formation energy (E_f) of austenite was calculated using *Eq* (2.1) for the stoichiometric $Ni_{50}Mn_{25}In_{25}$ alloy with and without effective Coulomb and exchange U and J coupling parameter. The E_f is defined as the total energy of the alloy minus the sum of the energies of the related pure elements in their reference states [43]. For the $Ni_{50}Mn_{25}In_{25}$ alloy, the unit which contains 2 Ni atoms, 1 Mn atom and 1 In atom was considered here.

$$E_f = E_{tot}(Ni_2MnIn) - 2E_{Ni} - E_{Mn} - E_{In} \quad (2.1)$$

In the equation, E_{tot} is the energy of a conventional cell with the formula of $Ni_{50}Mn_{25}In_{25}$, and the E_{Ni}, E_{Mn}, and E_{In} is the calculated energy of the pure element Ni, Mn and In with the cubic $L2_1$ structure, respectively. The energy per atom in their ground state were first calculated as the reference for the formation energy calculations. The results are shown in Table 2.2.

Table 2.2 Formation energy of pure element

element	E/(eV/atom)
Pure_Ni	-5.557
Pure_Mn	-8.883
Pure _In	-2.557

Using the theoretical equilibrium optimized lattice parameter, the elastic constants were calculated by the energy-strain relationship, which is obtained as the second derivatives of the system energy with respect to the strains [29]. It should be noted that the distortion within 2 % was employed to minimize the errors, which could arise from the higher-order terms in the Taylor equation. The bulk modulus was derived from the Equation of States (EOS) by the Morse function [28] and the shear modulus *C'* was obtained from the orthorhombic distortions [30], then the crystal elastic constants (C_{11} and C_{12}) were obtained from the bulk modulus $B = (C_{11}+2C_{12})/3$ and the tetragonal shear modulus $C' = 1/2 (C_{11}-C_{12})$. For the band structure calculations, the self-consistent CHGCAR file was determined by a fully self-consistent calculation with a k-point grid spanning the entire Brillouin zone. The Density of States (DOS) was calculated by the tetrahedron method with the Blöchl corrections using the Gamma centered k-mesh. Taking the position of non-interacting atoms as a reference, the charge density difference was calculated and analyzed by the VESTA software [22]. The Generalized Gradient Approximation exchange-correlation (*GGA + U*) method was used to account for the on-site correlation at the transition-metal sites considering electron-electron correlation [40].

2.4 Results and discussion

With the aim to figure out the influence of the Hubbard *U* and *J* parameter on phase stability of the stoichiometric $Ni_{50}Mn_{25}In_{25}$ alloy, a series of $Ni_{50}Mn_{25}In_{25}$ alloys with 26 different Hubbard *U* and *J* parameter combinations were simulated at 0 K. Firstly, the structural parameter, the ground state energy and the total magnetic moment of the $Ni_{50}Mn_{25}In_{25}$ alloy without considering any Hubbard *U* parameter were calculated by crystal structure optimization within a 16-atom cell using the VASP. The 16-atom cell was constructed using the experimental lattice parameter a = 6.071Å [13]. The optimized lattice parameter is 6.061 Å which is in good agreement with the previous experimental and computational results [44,45]. Then the structural properties of the austenite phase were also calculated considering the effective Coulomb and exchange parameters, and the results are displayed in Fig. 2.3. From Fig 2.3 (a), we could find that the equilibrium structural parameter *a* change with the *U* and *J* parameters. For all *J* values, the optimized lattice parameter increases first and then decreases with the increase of the *U* value. The lattice parameters *a* become very close at *U* equal to 6 under all the *J* values. These lattice parameters are near the experimentally evaluated value. However, the ground state energy increases with the *U* value for all *J* values, as shown in Fig. 2.3 (b), which means that the increased *U* value would decrease the stability of the austenite of the $Ni_{50}Mn_{25}In_{25}$ alloy. It decreases with the increased *J* values for all the *U* values except for the cases of *J* equal to 0.5 and 0.55. At these two *J* values, the ground state energies are very close at each *U* value. This means that the phase stability would be enhanced by the *J* value and it could arrive at a stable stage around *J* equal to 0.5. The magnetic moment has a similar tendency to that of the lattice parameter with all the *U* and *J* coupling, as shown in Fig. 2.3 (c). It increases with *U* and then decreases when *U* is larger than 6 eV for all the *J*.

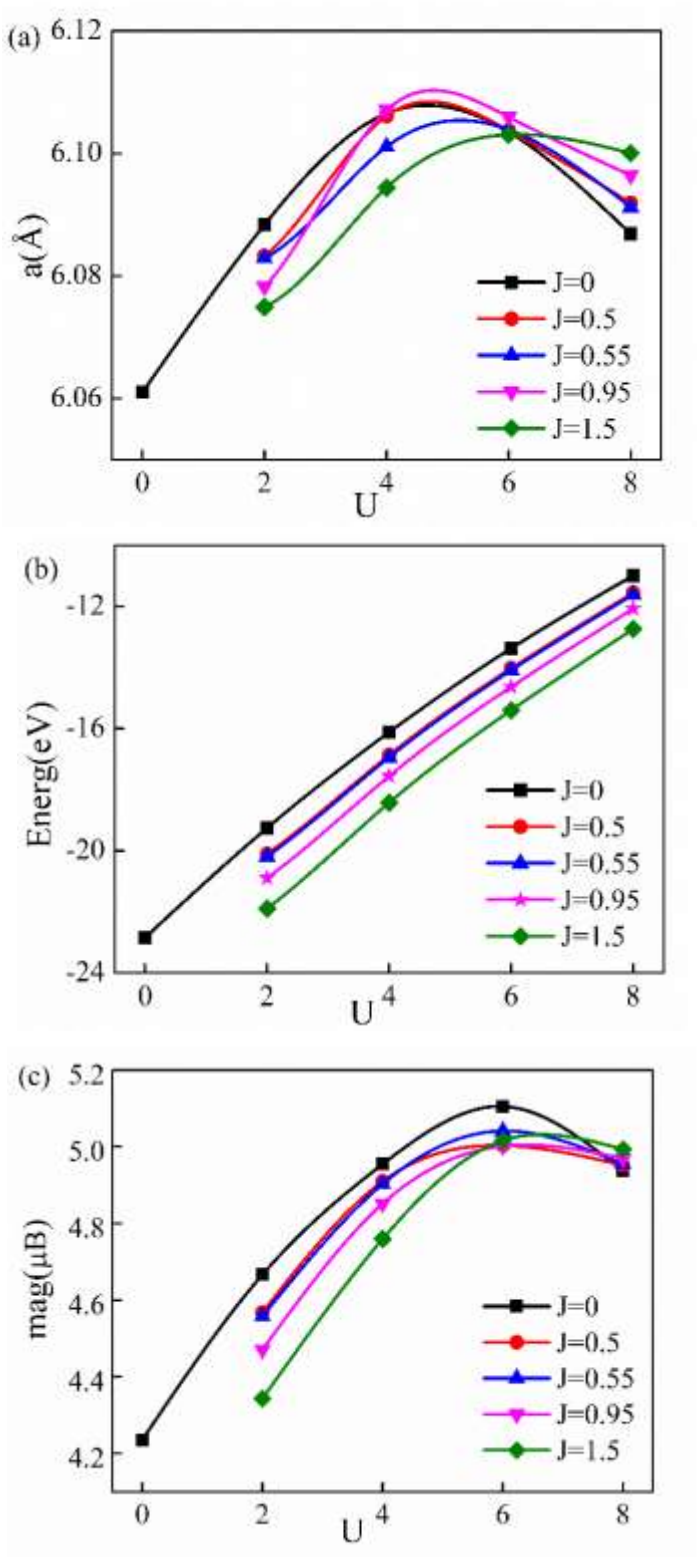

Fig. 2.3 Variations of (a) optimized lattice parameter; (b) ground state energy; (c) total magnetic moment of austenite of $Ni_{50}Mn_{25}In_{25}$ alloy with U and J coupling.

Then the phase stability was analyzed by the elastic constants and bulk modulus with different *U* and *J* coupling. Firstly, the bulk modulus and the elastic constants of the cubic structure without *U* and *J* coupling were calculated and compared with of the published experimental data [5] and calculation data [46], as shown in Table 2.4. It is seen that the calculated elastic constant ($C_{11,}$ C_{12}) of the $Ni_{50}Mn_{25}In_{25}$ austenite is lower than the theoretical results [46] which is obtained by the full potential linear muffintin orbital method. In present work, C_{44} is around 90 GPa, which is consistent with the reported experimental results, as shown in the table. For the bulk modulus, its value is positive but a little larger than the calculation result in Ref. [46]. Our calculational results which were obtained by the pseudopotential method using VASP are comparable to the previous experimental results.

Table 2.4 Bulk modulus and elastic constants of austenite phase with $L2_1$ structure obtained from without *U* and *J* coupling calculation, compared with experimental and theoretical results obtained from the previous literature. Unit is GPa.

	PAW_PBE	Exp. [5][a]	Exp. [5][b]	Theo. [46]
B	132.76	116	174	129
C_{11}	147.05	132±8	190±5	22.09
C_{12}	128.84	108	166	166.93
C_{44}	90.52	90±3	90±15	59.56

[a] Elastic constants obtained from the ultrasonic methods at 300 K [5].

[b] Elastic constants obtained from using Neutron diffraction experiments with the initial slopes of the acoustic phonon branches ($\xi \rightarrow 0$) at 520 K [5].

The calculation of the elastic constants of $Ni_{50}Mn_{25}In_{25}$ with different *U* and *J* coupling were carried out, as displayed in Fig. 2.4. The black dash line was the result of the calculation without *U* and *J* coupling. It is seen that the bulk modulus (*B*) and the elastic constants (C_{11} and C_{12}) vary with the Hubbard *U* and *J* values and converge at *U* equal to 8 eV for all the J values. The values

of C_{11}, C_{12}, and B at convergence vary with the different Hubbard U and J coupling and show large difference compared with the values without Hubbard U and J coupling, whereas the values of C_{44} converge to 101 GPa at U = 8 eV for all the J values. The negative C_{11}-$|C_{12}|$ values of U = 4 eV showed that the U = 4eV would lead the disability of the austenite structure. From the elastic constant results, we could deduce that the phase stability of the austenite of $Ni_{50}Mn_{25}In_{25}$ alloy could be affected by the Hubbard U and J coupling.

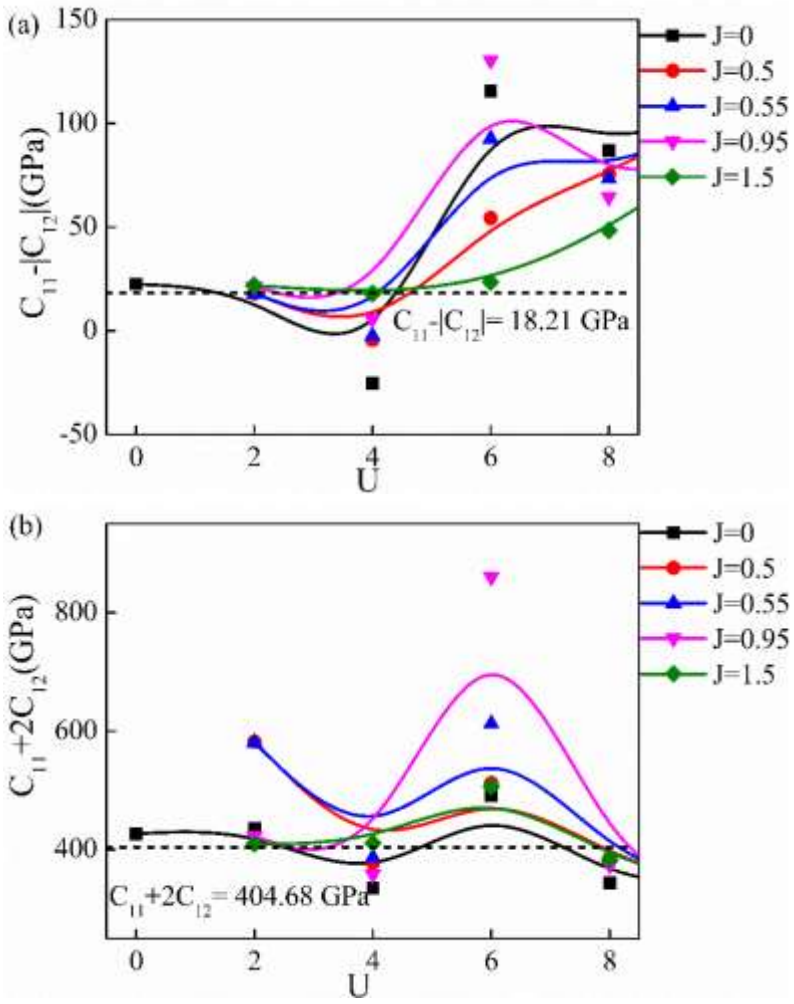

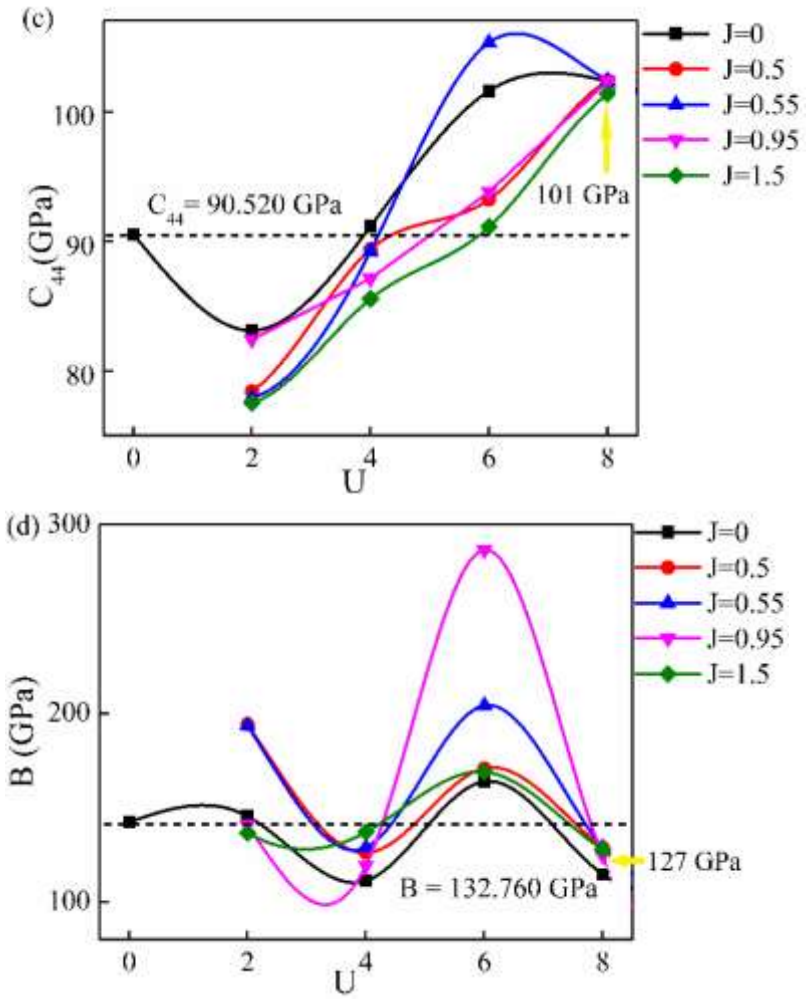

Fig. 2.4 Variation of elastic constants of austenite of $Ni_{50}Mn_{25}In_{25}$ alloy with different spin orbital U and J coupling. Dashed lines stand for elastic constants without U and J coupling

Therefore, based on the above effective Coulomb and exchange parameters test, we choose the effective Coulomb parameter U = 6 eV based on the optimization of the lattice parameter and the magnetic moment, and the effective exchange parameter J = 0.5 from the minimum ground state energy variation, for further physical properties analysis.

The formation energies of the austenite phase without and with U = 6 eV and J = 0.5 coupling were calculated based on the optimized equilibrium state and the ground state energy of the ferromagnetic austenite $Ni_{50}Mn_{25}In_{25}$ alloy. The results were displayed in Table 2.3. Compared with the calculation result without considering the effective Coulomb and exchange U and J

coupling, the lattice parameter of the austenite increases from 6.0610 Å to 6.1037 Å by considering Hubbard *U* and *J* coupling, which are both in good consistent with the previous experimental measurement values (*a* = 6.071 Å [47] and 6.078 Å [48]) and theoretical value (*a* = 6.090 Å [49]). The magnetic moment of the ferromagnetic austenite of the $Ni_{50}Mn_{25}In_{25}$ alloy without *U* and *J* coupling is 4.235 μ_B which agrees with the theoretical simulation results (4.208 μ_B [50] and 4.410 μ_B [49]). Whereas, the magnetic moment increases to 5.0035 μ_B, when the Hubbard *U* = 6 eV and *J* = 0.5, which is slightly larger than the previous results. However, larger ground state energy and the larger formation energy were obtained, which means that the consideration of the Hubbard *U* and *J* coupling makes the $L2_1$ structure less stable. Based on the comparison of the formation energy of the $Ni_{50}Mn_{25}In_{25}$ ferromagnetic austenite with and without the *U* and *J* coupling, we could find that the Hubbard *U* and *J* coupling could reduce the stability of the cubic $L2_1$ austenite phase. However, based on the definition of the Hubbard *U* which could be used to embed the atoms in a polarization surrounding, the ground state would be lowered by adding the Hubbard *U* and *J* coupling into the $Ni_{50}Mn_{25}In_{25}$ alloy which has the transition metal element with *3d* electrons [22].

Table 2.3 Optimized lattice parameter, magnetic moment and formation energy of cubic $Ni_{50}Mn_{25}In_{25}$ austenite (unit cell with 4 atoms) without *U* and *J* coupling and with *U* = 6 eV and *J* = 0.5.

	a/(Å)	mag/(□$_B$)	E_0/(*eV*)	E_f/(*eV*)	structure
$Ni_{50}Mn_{25}In_{25}$ (without *U* + *J* coupling)	6.061	4.235	-22.838	-0.256	cubic
$Ni_{50}Mn_{25}In_{25}$ (*U* = 6 eV and *J* = 0.5)	6.104	5.003	-14.024	8.531	cubic

In order to figure out the effect of the Hubbard *U* and *J* parameter on the electronic structure of the $Ni_{50}Mn_{25}In_{25}$ alloy, which has a strong correlation with the *3d* electrons in the transition

metal elements, we further calculated the band structure, the density of states (DOS) and the charge density differences. Fig. 2.5 displays the band structure and the DOS of the austenite of the $Ni_{50}Mn_{25}In_{25}$ alloy with the cubic structure without and with the *U* and *J* coupling. From the band structures in the figure, we found that the effective Coulomb and exchange parameters did not make significant change around the Fermi level, and only some band structures move away from the Fermi level which shows the energy as -6 eV instead of -1 eV. Concerning the DOSs, we could find that the Mn *3d* states and In *p*-states are hybridized with the Ni *3d* states under the Fermi level in the calculation without the Hubbard *U* and *J* coupling. The effect of *U* and *J* coupling would create a stronger localization of the Ni *3d* states, as shown in Fig. 2.5 (b). There is a ~10 eV energy split between the Mn up and down *3d*-states with considering the effective Coulomb and exchange *U* and *J* coupling, whereas they were near the Fermi level without the effective Coulomb and exchange parameters. We could also find a strengthened In *p*-states moving far away from the Fermi level, when the effective Coulomb *U* and *J* parameters were considered. However, with the effective Coulomb and exchange *U* and *J* coupling, the bandgap is still showing the metallic bonding in the cubic $Ni_{50}Mn_{25}In_{25}$ alloy.

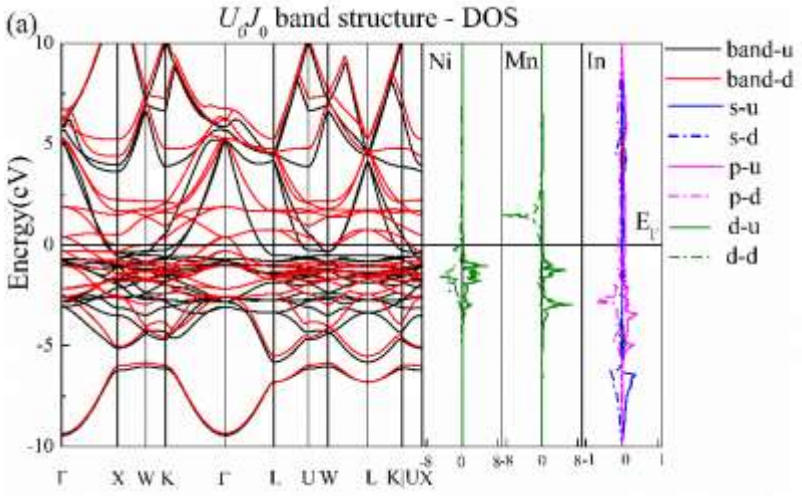

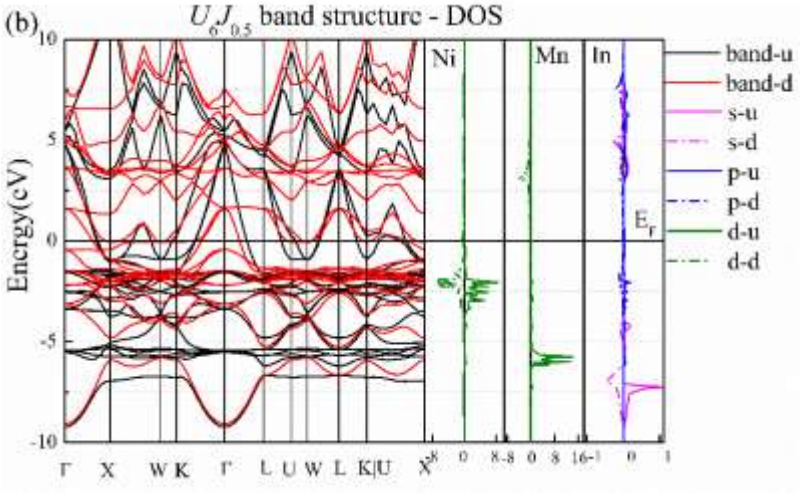

Fig. 2.5 Band structure and density of states (DOS) of austenite of $Ni_{50}Mn_{25}In_{25}$ with U_0J_0 and $U_6J_{0.5}$ calculations.

The charge density difference was also analyzed for different effective Coulomb and exchange parameters, and the calculation results without and with the effective Coulomb and exchange coupling $U = 6$ and $J = 0.5$ were shown in Fig. 2.6. It is seen that the redistribution of the charge density could be affected by the Hubbard U and J parameters. We would find that a charge density localization between the Mn and the Ni atoms. This density of charge increases with the increase of the U and J coupling. For $U = 6$ and $J = 0.5$, a charge density localization appears between the Ni and In atoms. There is a charge transfer between the In *p*-orbitals and the Ni *d*-orbitals. We could obtain the same effect between Mn *d*-orbitals and Ni *d*-orbitals. The electronic configuration of the Ni, Mn and In atoms (initially $3d^84s^2$, $3d^64s^1$ and $5s^25p^1$) changes toward the respective $3d^{10}4s^2$, $3d^54s^1$ and $5s^25p^0$.

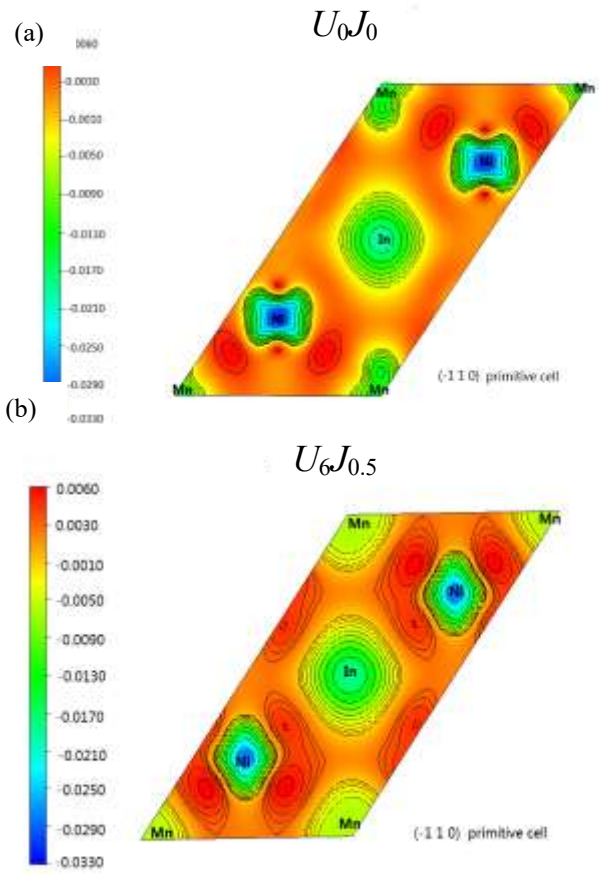

Fig. 2.6 Charge density difference of $Ni_{50}Mn_{25}In_{25}$ calculated (a) U_0J_0 (without effective Coulomb and exchange parameters); (b) $U_6J_{0.5}$ (with effective Coulomb and exchange parameters).

2.5 Conclusions

The effect of the effective Coulomb U and exchange J parameters on the structural parameters, the phase stability (including the ground state energy, the formation energy, and the elastic constants), and the electronic structure (including the band structure and the density of states, the magnetic moment, and the charge density difference) of the cubic austenite stoichiometric $Ni_{50}Mn_{25}In_{25}$ alloy was systematically calculated in this chapter. The first principle calculations combined with exchange-correlation of the *GGA* + *U* approach allow us to draw the following conclusions.

i) With 26 different effective Coulomb and exchange U and J parameter couplings, we found that the optimized lattice parameter changes with the effective Coulomb and exchange U and J parameters around the experimentally evaluated value. The lattice parameters a become extremely close at U equal to 6 under all the J values. The ground state energy increases with U value at all J values, whereas it could arrive at a stable stage around J equal to 0.5. The elastic constants and the bulk modulus vary with the different U and J coupling, and did not show any evident tendency to enhance or reduce the phase stability. Therefore, we choose the effective Coulomb parameter of U = 6 eV, which is based on the optimization of the lattice parameter and the magnetic moment, and the effective exchange parameter J = 0.5 which is based on the minimum ground state energy variation for further physical properties analysis.

ii) With U = 6 eV and J = 0.5 considered into the exchange-correlation GGA method, the lattice parameter of the austenite increases slightly. The magnetic moment is slightly larger than the result of the calculation without considering the effective Coulomb and exchange parameters. However, the calculation did not obtain a lower formation energy but a higher value, which means that the consideration of the Hubbard U and J coupling makes the $L2_1$ structure less stable.

iii) The effects of the effective Coulomb and exchange parameters on the electronic structure were carried out by the calculation of the band structure, density of states and charge density difference. Even though the Coulomb parameter has some slight influence on the spin coupling, there is no obvious change around the Fermi Level. With the effective Coulomb and exchange parameters U and J coupling, the bandgap is still showing the metallic bonding in the cubic austenite $Ni_{50}Mn_{25}In_{25}$ alloy.

In the present Chapter, with the aim to present more accurately electronic structure near Fermi level for the cubic austenite of the $Ni_{50}Mn_{25}In_{25}$ alloy with the metal transition element Ni and Mn with *3d* orbitals, we first tried to systematically calculate the physical properties by considering the effective Coulomb and exchange *U* and *J* parameters with the exchange-correlation *GGA* method in VASP. However, we did not find any obvious effect on the equilibrium crystal structure or the electronic structure. We could conclude that there is no need to add the efficient Coulomb parameter into the physical property calculation of the Heusler type Ni-Mn-In alloys in the first-principle calculations. Therefore, we did not add the efficient Coulomb parameter into the exchange-correlation for later calculations for the Ni-Mn-In alloys.

Reference

1. Sutou, Y.; Imano, Y.; Koeda, N.; Omori, T.; Kainuma, R.; Ishida, K.; Oikawa, K. Magnetic and martensitic transformations of NiMnX (X = In, Sn, Sb) ferromagnetic shape memory alloys. *Appl. Phys. Lett.* **2004**, *85*, 4358–4360.
2. Ullakko, K.; Huang, J.K.; Kantner, C.; O'Handley, R.C.; Kokorin, V. V. Large magnetic-field-induced strains in Ni_2MnGa single crystals. *Appl Phys Lett* **1996**, *69*, 1966–1968.
3. Zheludev, A.; Shapiro, S.; Wochner, P.; Tanner, L. Precursor effects and premartensitic transformation in Ni_2MnGa. *Phys Rev B* **1996**, *54*, 15045–15050.
4. Webster, P.J.; Ziebeck, K.R.A.; Town, S.L.; Peak, M.S. Magnetic order and phase transformation in Ni_2MnGa. *Philos Mag Part B* **1984**, *49*, 295–310.
5. Moya, X.; González-Alonso, D.; Mañosa, L.; Planes, A.; Garlea, V.O.; Lograsso, T.A.; Schlagel, D.L.; Zarestky, J.L.; Aksoy, S.; Acet, M. Lattice dynamics in magnetic superelastic Ni-Mn-In alloys: Neutron scattering and ultrasonic experiments. *Phys Rev B* **2009**, *79*, 214118.

6. Ito, W.; Imano, Y.; Kainuma, R.; Sutou, Y.; Oikawa, K.; Ishida, K. Martensitic and magnetic transformation behaviors in Heusler-type NiMnIn and NiCoMnIn metamagnetic shape memory alloys. *Metall Mater Trans A* **2007**, *38*, 759–766.

7. Krenke, T.; Acet, M.; Wassermann, E.F.; Moya, X.; Mañosa, L.; Planes, A. Ferromagnetism in the austenitic and martensitic states of Ni-Mn-In alloys. *Phys Rev B* **2006**, *73*, 174413.

8. Sánchez Llamazares, J.L.; Sanchez, T.; Santos, J.D.; Ṕrez, M.J.; Sanchez, M.L.; Hernando, B.; Escoda, L.; Suñol, J.J.; Varga, R. Martensitic phase transformation in rapidly solidified $Mn_{50}Ni_{40}In_{10}$ alloy ribbons. *Appl. Phys. Lett.* **2008**, *92*, 2006–2009.

9. Kazakov, A.P.; Prudnikov, V.N.; Granovsky, A.B.; Zhukov, A.P.; Gonzalez, J.; Dubenko, I.; Pathak, A.K.; Stadler, S.; Ali, N. Direct measurements of field-induced adiabatic temperature changes near compound phase transitions in Ni-Mn-In based Heusler alloys. *Appl. Phys. Lett.* **2011**, *98*, 131911.

10. Pathak, A.K.; Khan, M.; Dubenko, I.; Stadler, S.; Ali, N. Large magnetic entropy change in $Ni_{50}Mn_{50-x}In_x$ Heusler alloys. *Appl Phys Lett* **2007**, *90*, 262504.

11. Oikawa, K.; Ito, W.; Imano, Y.; Sutou, Y.; Kainuma, R.; Ishida, K.; Okamoto, S.; Kitakami, O.; Kanomata, T. Effect of magnetic field on martensitic transition of $Ni_{46}Mn_{41}In_{13}$ Heusler alloy. *Appl. Phys. Lett.* **2006**, *88*, 2004–2007.

12. Liu, J.; Woodcock, T.G.; Scheerbaum, N.; Gutfleisch, O. Influence of annealing on magnetic field-induced structural transformation and magnetocaloric effect in Ni-Mn-In-Co ribbons. *Acta mater* **2009**, *57*, 4911–4920.

13. Yan, H.; Zhang, Y.; Xu, N.; Senyshyn, A.; Brokmeier, H.G.; Esling, C.; Zhao, X.; Zuo, L.; Liang Zuo; Zuo, L. Crystal structure determination of incommensurate modulated martensite in Ni-Mn-In Heusler alloys. *Acta Mater* **2015**, *88*, 375–388.

14. Zhang, C.; Zhang, Y.; Esling, C.; Zhao, X.; Zuo, L. Crystallographic features of the martensitic transformation and their impact on variant organization in the intermetallic compound $Ni_{50}Mn_{38}Sb_{12}$ studied by SEM/EBSD. *IUCrJ* **2017**, *4*, 700–709.

15. Liu, Z.H.; Hu, H.N.; Liu, G.D.; Cui, Y.T.; Zhang, M.; Chen, J.L.; Wu, G.H.; Xiao, G. Electronic structure and ferromagnetism in the martensitic-transformation material Ni_2FeGa. *Phys Rev B* **2004**, *69*, 134415.

16. Sandeep, D.P.R.; Shankar, A.; Ghimire, M.P.; Khenata, R.; Thapa, R.K. Study of electronic and magnetic properties in 4f electron based cubic $EuAlO_3$: A first-principles calculation. *Phys Scr* **2015**, *90*, 065803.

17. Rai, D.P.; Thapa, R.K. A First Principle Calculation of Full-Heusler Alloy Co_2TiAl: LSDA+U Method. *ISRN Condens Matter Phys* **2012**, *2012*, 41326.

18. Dudarev, S.L.; Botton, G.A.; Savrasov, S.Y.; Humphreys, C.J.; Sutton, A.P. Electron-energy-loss spectra and the structural stability of nickel oxide: An LSDA + U study. *Phys Rev B* **1998**, *57*, 1505–1509.

19. Anisimov, V.I.; Aryasetiawan, F.; Lichtenstein, A.I. First-principles calculations of the electronic structure and spectra of strongly correlated systems: the LDA + U method. *J Phys Condens Matter* **1997**, *9*, 767–808.

20. Kandpal, H.C.; Fecher, G.H.; Felser, C. Correlation in the transition-metal-based Heusler compounds Co_2MnSi and Co_2FeSi. *Phys Rev B* **2006**, *73*, 094422.

21. Meinders, M.B.J.; Van Den Brink, J.; Lorenzana, J.; Sawatzky, G.A. Atomic screening and intersite Coulomb repulsion in strongly correlated systems. *Phys Rev B* **1995**, *52*, 2484–2495.

22. Brink, J. Van Den; Meinders, M.B.J.; Sawatzky, G.A. Influence of screening effects and

inter-site Coulomb repulsion on the insulating correlation gap. **1995**, *207*, 682–684.

23. Fu, H.; Liu, W.F.; Peng, F.; Gao, T. Phase transition and thermodynamic properties of MgTe under high pressure. *J Alloys Compd* **2009**, *480*, 587–591.
24. Fine, M.E.; Brown, L.D.; Marcus, H.L. Elastic constants versus melting temperature in metals. *Scr Metall* **1984**, *18*, 951–956.
25. Li, C.; Wang, Z. Computational modelling and ab initio calculations of MAX Phases-I. *Adv Sci Technol $M_{n+1}AX_n$ Phases* **2012**, 197–222.
26. Ravindran, P.; Fast, L.; Korzhavyi, P.A.; Johansson, B.; Wills, J.; Eriksson, O. Density functional theory for calculation of elastic properties of orthorhombic crystals: Application to $TiSi_2$. *J Appl Phys* **1998**, *84*, 4891–4904.
27. Born, M.; Huang, K. *Dynamical Theory of Crystal Lattices*; Oxford University Press: Oxford, 1954;
28. Moruzzi, V.L.; Janak, J.F.; Schwarz, K. Calculated thermal properties of metals. *Phys Rev B* **1988**, *37*, 790–799.
29. Tian, F. A review of solid-solution models of high-entropy alloys based on ab initio calculations. *Front Mater* **2017**, *4*, 1–10.
30. Vitos, L. *Computational quantum mechanics for materials engineers: the EMTO method and applications*; Springer US: Boston, MA, 2005; ISBN 9781846289507.
31. Gao, M.C.; Hawk, J.A.; Alman, D.E. Computational modeling of high-entropy alloys : Structures , thermodynamics and elasticity. *J Mater Res* **2017**, *32*, 3627.
32. Nielsen, O.H.; Martin, R.M. Quantum-mechanical theory of stress and force. *Phys Rev B* **1985**, *32*, 3780–3791.
33. Sholl, D.S.; Janice A. Steckel *Density functional theory: a practical introduction*; New

Jersey, Canada, 1999;

34. Fu, H.; Li, X.; Liu, W.; Ma, Y.; Gao, T.; Hong, X. Electronic and dynamical properties of NiAl studied from first principles. *Intermetallics* **2011**, *19*, 1959–1967.
35. Kresse, G.; Furthmüller, J.; Hafner, J. Ab initio force constant approach to phonon dispersion relations of diamond and graphite. *Epl* **1995**, *32*, 729–734.
36. Kresse, G.; Hafner, J. Ab Initio Molecular Dynamics of Liquid Metals. *Phys Rev B* **1993**, *47*, 558–561.
37. Kresse, G.; Furthmüller, J. Efficiency of total energy calculations for metals and semiconductors using a plane-wave basis set. *Comput Mater Sci* **1996**, *6*, 15–50.
38. Blöchl, P.E. Projector augmented-wave method. *Phys Rev B* **1994**, *50*, 17953–17979.
39. Hafner, J. Atomic-scale computational materials science. *Acta mater* **2000**, *48*, 71–92.
40. Methfessel, M.; Paxton, A.T. High-precision sampling for Brillouin-zone integration in metals. *Phys Rev B* **1989**, *40*, 3616–3621.
41. Perdew, J.P.; Burke, K.; Ernzerhof, M. Generalized gradient approximation made simple. *Phys Rev Lett* **1996**, *77*, 3865–3868.
42. Monkhorst, H.J.; Pack, J.D. Special points for Brillouin-zone integrations. *Phys Rev B* **1977**, *13*, 5188–5192.
43. Chen, J.; Li, Y.; Shang, J.; Xu, H. First principles calculations on martensitic transformation and phase instability of Ni-Mn-Ga high temperature shape memory alloys. *Appl. Phys. Lett.* **2006**, *89*, 231921.
44. Priolkar, K.R.; Bhobe, P.A.; Lobo, D.N.; D'Souza, S.W.; Barman, S.R.; Chakrabarti, A.; Emura, S. Antiferromagnetic exchange interactions in the $Ni_2Mn_{1.4}In_{0.6}$ ferromagnetic Heusler alloy. *Phys Rev B* **2013**, *87*, 144412.

45. Miyamoto, T.; Ito, W.; Umetsu, R.Y.; Kainuma, R.; Kanomata, T.; Ishida, K. Phase stability and magnetic properties of $Ni_{50}Mn_{50-x}In_x$ Heusler-type alloys. *Scr Mater* **2010**, *62*, 151–154.

46. Rached, H.; Rached, D.; Khenata, R.; Reshak, A.H.; Rabah, M. First-principles calculations of structural, elastic and electronic properties of Ni_2MnZ (Z = Al, Ga and In) Heusler alloys. *Phys Stat Sol* **2009**, *246*, 1580–1586.

47. Li, C.M.; Luo, H. Bin; Hu, Q.M.; Yang, R.; Johansson, B.; Vitos, L. Role of magnetic and atomic ordering in the martensitic transformation of Ni-Mn-In from a first-principles study. *Phys Rev B* **2012**, *86*, 214205.

48. Chatterjee, S.; Singh, V.R.; Deb, A.K.; Giri, S.; De, S.K.; Dasgupta, I.; Majumdar, S. Magnetic properties of $Ni_{2+x}Mn_{1-x}In$ Heusler alloys: Theory and experiment. *J Magn Magn Mater* **2010**, *322*, 102–107.

49. Ağduk, S.; Gökoğlu, G. First-principles study of elastic and vibrational properties of Ni_2MnIn magnetic shape memory alloys. *Eur Phys J B* **2011**, *79*, 509–514.

50. Şaşıoğlu, E.; Sandratskii, L.M.; Bruno, P. First-principles calculation of the intersublattice exchange interactions and Curie temperatures of the full Heusler alloys Ni_2MnX (X = Ga, In, Sn, Sb). *Phys Rev B* **2004**, *70*, 24427.

Chapter 3 Composition dependent martensitic structural preference of $Ni_{50}Mn_xIn_{50-x}$ alloys by VASP and EMTO-CPA method

3.1 Outline

In this chapter, in order to figure out the Mn concentration effect on the preference of the martensitic structure, the tetragonal distortion was employed in the off-stoichiometric $Ni_{50}Mn_xIn_{50-x}$ alloys with a series of Mn contents using the Extra Muffin-tin Orbital combined with Coherent Potential Approximation (EMTO-CPA) without a spin fixation by taking the stoichiometric $Ni_{50}Mn_xIn_{50-x}$ alloy as the reference. Furthermore, to figure out more accurate preference of the martensitic structure, the formation energies of the tetragonal $L1_0$ and the orthorhombic structures at ferromagnetic state were calculated using different relaxation method by the chemical disorder method with a 4-atom cell by the EMTO-CPA for the tetragonal structure ($c/a > 1$) and a supercell method with a 96-atom cell by VASP for the orthorhombic structure at 0 K, respectively. Moreover, the effect of the Mn concentration on the magnetic properties was also calculated for the austenite with the cubic $L2_1$ structure and the martensite with the tetragonal $L1_0$ and the orthorhombic structures, and the antiferromagnetic interaction of the martensite with the tetragonal $L1_0$ structure are also carried out.

3.2 Introduction

Based on the activation mechanisms of shape memory effect, the Heusler type Ni-Mn-based alloys could be classified into two groups: (i) Ni-Mn-Ga alloys, in which the shape change is originated from the magnetic field-induced martensite variant rearrangement [1–4]; (ii) Ni-Mn-X (X = In, Sb and Sn) alloys, in which the shape change is generated from the magnetic field-induced reverse martensitic transformation [5–7]. During the cooling process, both these alloys undergo a

series of transitions, including the melt to the partially disordered *B2* phase transition [8], the second-order *B2* - $L2_1$ transition [9] and the first-order martensitic transition. Especially, for the Ni-Mn-In alloys, the austenite could transform into two kinds of martensite phase depending on the chemical composition, *i.e.*, (i) the modulated martensite with orthorhombic or monoclinic structure, such as *6M* [10], *10M* [11] or *4O* [12] structures; (ii) the non-modulated martensite with tetragonal $L1_0$ structure [13]. These structures have been previously examined by X-ray diffraction, neutron diffraction or TEM selected area electron diffraction.

For the off-stoichiometric $Ni_{50}Mn_xIn_{50-x}$ alloys, the ferromagnetic austenite does not directly transform to the ferromagnetic martensite, but has to go through the antiferromagnetic martensite, which is called metamagnetic transition [14,15]. That is because the extra Mn atoms may enhance the ferromagnetism in the austenite by increasing the total magnetic moment [11,16]. This results in the antiferromagnetic exchange interactions in the martensite, which could be attributed to the different hybridization of Mn-Mn atoms [16–18] or Ni-Mn atoms [19,20]. It also leads to a composition-dependent Curie temperature variation of the martensite. The Curie temperature could decrease drastically with the increased Mn concentration [6]. Moreover, the phase stabilities of austenite and martensite could vary with the Mn composition [11], and the martensitic transition temperatures would increase significantly with the additional Mn content [6,21]. Therefore, the effect of the Mn concentration on the phase stability and the magnetic properties of the austenite and the martensite [21–23] is critical for understanding the martensitic transformation. In the previous report [16], the possibility of martensitic phase transition was studied in Ni-Mn-In alloys, where the structural transformation was realized by the tetragonal distortion and the antiferromagnetic interaction was caused by the Mn-Mn hybridization. The results showed a transition from the cubic structure into the tetragonal structure with *c* larger than *a* (in the cubic

coordination system) [16]. However, the possibility of martensitic transition from the cubic structure to the tetragonal structure with *c* smaller than *a* (in the cubic coordinate system) by tetragonal distortion was not much studied. It is considered that this kind of tetragonal structure could be the origin of the orthorhombic or the monoclinic modulated structure leading to the formation of the modulated structures [6,22]. Moreover, as demonstrated by experimental observations and theoretical calculations, the antiferromagnetic interaction could also be attributed to the Ni-Mn hybridization with additional Mn content [19,20,24].

In the present work, the effect of the Mn concentration on the preference of the martensitic structure in the off-stoichiometric $Ni_{50}Mn_xIn_{50-x}$ alloys was studied by the tetragonal distortion using the Extra Muffin-tin Orbital method combined with the Coherent Potential Approximation (EMTO-CPA) under magnetic structure optimization. Based on the martensitic structure preference results, the phase stability of the tetragonal $L1_0$ and the orthorhombic structures in the ferromagnetic state were calculated by chemical disorder method within the EMTO-CPA and the supercell method within the VASP. The formation energies were compared with the cubic $L2_1$ structure of the off-stoichiometric $Ni_{50}Mn_xIn_{50-x}$ alloys with different Mn contents. Furthermore, the effect of the Mn concentration on the total magnetic moment was calculated for the three structures in the ferromagnetic state. The type of antiferromagnetic interaction within the tetragonal $L1_0$ martensite in the ferromagnetic and antiferromagnetic coexisting state was also analyzed.

3.3 Computational method

Before constructing the crystal structures of the off-stoichiometric $Ni_{50}Mn_xIn_{50-x}$ alloys, the preferred site of the excess Mn atoms with an amount of 6.25 at. % in a unit cell with 16 atoms was determined by the formation energies using the Vienna Ab-initio Simulation Package (VASP) [25]. The conventional cell of the cubic $L2_1$ $Ni_{50}Mn_{25}In_{25}$ alloy is presented in Fig. 3.1. In the figure, the

primitive cell is also outlined with the dashed lines. Here, the atomic combination of the primitive cell (4 atoms) is defined as a motif, and it is used as one of the structure units for calculating the formation energy and total magnetic moment of other structures (tetragonal and orthorhombic, as described later). The full charge density method was applied to treat the tetragonal distortion by the Extra Muffin-Tin Orbital method combined with the Coherent Potential Approximation (EMTO-CPA) [26–28] with the optimization of the magnetic structure. For the phase stability analysis of the tetragonal $L1_0$ martensite of the Ni-Mn-In alloys with different Mn concentrations, the more efficient EMTO-CPA was used. For the simulation of the orthorhombic martensite structures with different Mn concentrations, a cell containing 96 atoms was constructed with the supercell method allowing volume relaxation using the VASP. The Generalized Gradient Approximation (GGA), established by Perdew, Burke, and Ernzerhof (GGA-PBE) [29], was employed to describe the exchange-correlation functions. The electronic configurations were Ni ($3d^8 4s^2$), Mn ($3d^6 4s^1$), and In ($4s^2 4p^1$), respectively. Based on the convergence test, the reciprocal-grid density of 12 × 12 × 12 Gamma centered Monkhorst-Pack k-point meshes for the $L2_1$ primitive cell and 420 eV as the kinetic energy cutoff were applied in the VASP calculations. The EMTO was performed with a basis set including the *s*, *p*, *d*, *f* orbitals. After carefully testing the convergence of the equilibrium parameter against the k-point meshes, a 13 × 13 × 13 k-point meshes was set for the primitive cell with 4 atoms. The formation energy (E_f) of the $Ni_2Mn_xIn_{2-x}$ was determined according to the following function of the Mn concentration (x):

$$E_f(x) = E_0(Ni_2Mn_xIn_{2-x}) - 2 * E_{Ni} - x * E_{Mn} - (2-x) * E_{In}$$

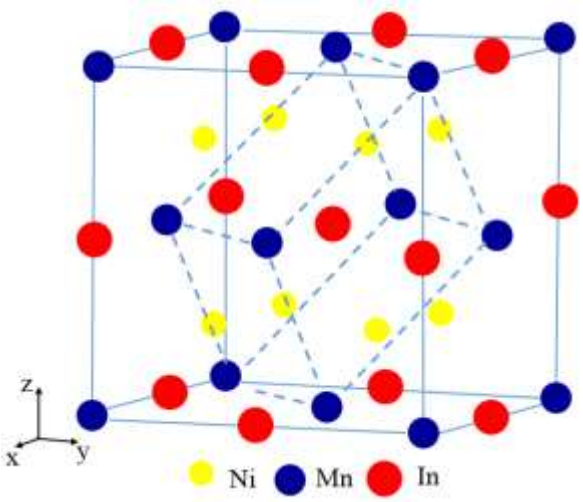

Fig. 3.1 Crystal structure of cubic $L2_1$ $Ni_{50}Mn_{25}In_{25}$ austenite. The solid lines outline a conventional cell with 16 atoms and the dashed lines outline a primitive cell with 4 atoms.

3.4 Results and discussion

To find out the sublattice site preference of the excess Mn atoms, the formation energies of different point defects within the 16-atom cell (Fig. 3.1) were tested by crystal structure optimization using VASP. The calculated formation energies of the perfect austenite and the austenite with 6.25 at. % point defects are shown in Table 3.1. It is seen that the values of the point vacancy defect formation are positive. This indicates that the point defect will reduce the ground state stability of the ferromagnetic cubic structures. Among all the defected structures, the sublattice with the substitution of Mn for In ($_{In}Mn$) possesses the lowest negative defect formation energy, which infers that this kind of point defect could exist steadily. Therefore, the excess Mn substituting for In was employed for the further study of the influence of Mn content on the martensitic structure preference in the off-stoichiometric $Ni_{50}Mn_xIn_{50-x}$ alloy. Note that the antisite defect with Mn substituting for Ni is not converged at 0 K, which indicates that the cubic structure of $Ni_{50-x}Mn_{25+x}In_{25}$ alloy could not exist at 0 K. This discovery is consistent with the fact that there is less evidence of such kinds of alloys in the previous experimental investigations.

Table 3.1 Optimized lattice parameters and formation energy of perfect austenite and austenite with point defect for a 16-atom cell (v_element indicates vacancy situation)

	a/(Å)	**E_v / (eV/unite cell)**		**a/(Å)**	**E_f / (eV/unite cell)**
v_Ni	6.0261	0.533	$_{In}$Mn	6.0645	-0.850
v_In	5.9195	1.500	$Ni_8Mn_4In_4$	6.0607	-1.130

As the stable structure of the Ni-Mn-X alloys could be changed with the type and the concentration of the element X [13], the tetragonal and the orthorhombic distortions can be applied to simulate the martensitic phase transition [30]. The non-modulated martensite with a tetragonal $L1_0$ structure is related to a distorted cubic structure with *c* larger than *a*. The modulated martensite with a monoclinic structure, like the orthorhombic structure, is originated from a distorted cubic structure with *c* less than *a*, as reported in the literature [11]. Moreover, the previous experimental observation revealed that the martensite exhibits a coexistence of ferromagnetic and antiferromagnetic interactions in the off-stoichiometric alloys. The antiferromagnetic interaction could be originated from Mn-Mn [16–18] or Ni-Mn hybridization [19,20]. It has been shown that the martensitic transition could not happen from the cubic $L2_1$ austenite to the tetragonal $L1_0$ martensite in the stoichiometric alloy [16]. Nevertheless, for the compounds with Mn concentrations ranging from 32.5 at. % to 40 at. %, the transformation could happen from the ferromagnetic cubic $L2_1$ austenite to the co-existing ferromagnetic and antiferromagnetic tetragonal $L1_0$ martensite. The antiferromagnetic interaction is supposed to come from the Mn-Mn hybridization by tetragonal distortion. However, the martensitic transformation from the cubic austenite to the modulated monoclinic martensite remains unclear. In order to figure out the effect of the Mn concentration on the martensite structure preference of the off-stoichiometric

$Ni_{50}Mn_xIn_{50-x}$ alloys and to reveal the antiferromagnetic interaction between the atoms, the tetragonal distortion was applied to determine the possible stable structures at 0 K for the first step. For the calculations, the *c/a* value is limited between 0.7~1.6, and no structural relaxation was conducted. The energies of different structures were calculated using the efficient EMTO-CPA method with the optimization of the magnetic structure. The calculated results were represented with the ground state energy difference between the distorted structure and the initial cubic structure at every Mn concentration. Based on the point defect formation energy analysis, four $Ni_{50}Mn_xIn_{50-x}$ alloys (x = 25, 29.25, 34.5 and 36.5) with the excess Mn substituting for In ($_{In}$Mn) were used. First, we set the ground state energy of the cubic structure (*c/a* = 1) of each alloy to be the reference state, *i.e.*, 0 eV. Then, the ground state energy difference between the distorted structure and its reference state was calculated as a function of the *c/a* ratio for each alloy, and the results are shown in Fig. 3.2 (a). It should be mentioned that the small deviations from 0 eV at *c/a* = 1 for the alloys with 29.25 at. % and 36.5 at. % Mn were caused by the curve fitting.

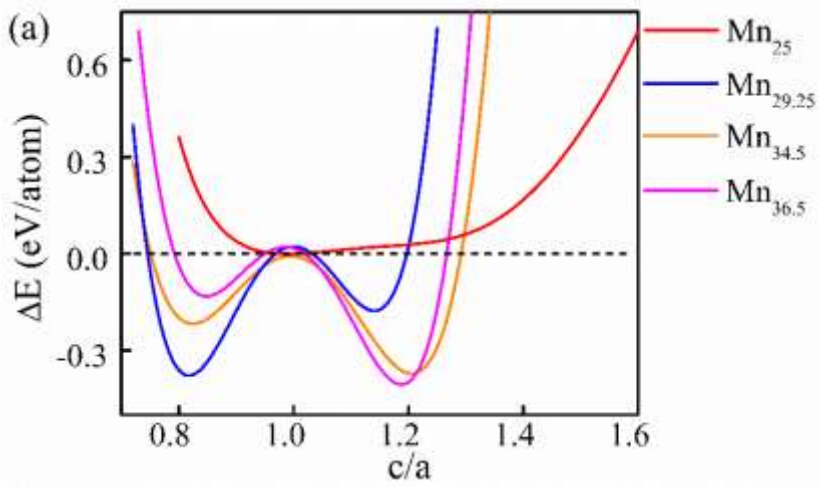

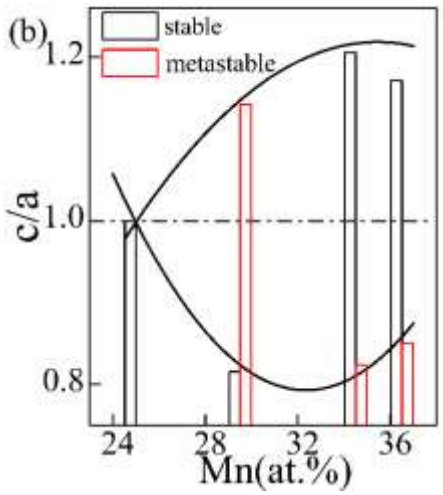

Fig. 3.2 (a) Variation of ground state energy difference as a function of tetragonal distortion (*c/a* ratio) in Ni-Mn-In alloys with different Mn contents. (b) *c/a* ratio value of local minimum energy point of Ni-Mn-In alloys with different Mn contents. Parabola curves indicate *c/a* ratio value of local minimum energy point for $c/a < 1$ and $c/a > 1$.

It is seen from Fig. 3.2 (a) that, for the stoichiometric $Ni_{50}Mn_{25}In_{25}$ compound, the perfect cubic structure with $c/a = 1$ possesses the minimum ground state energy. This reveals that the cubic structure is the most stable state and is hard to undergo any martensitic transformation, which corresponds to the previous calculation result [31]. In contrast, the ground state energy difference between the tetragonally distorted structure and the cubic structure of the off-stoichiometric $Ni_{50}Mn_xIn_{50-x}$ alloys is negative for both $c/a > 1$ and $c/a < 1$ distortions. The $Ni_{50}Mn_{29.25}In_{20.75}$ alloy has the lowest local minimum energy in the $c/a < 1$ case, whereas the $Ni_{50}Mn_{36.5}In_{13.5}$ alloy has the lowest local minimum energy in the $c/a > 1$ case. Since the structure having local minimum ground state energy difference corresponds to the possible stabilized tetragonal structure, we could deduce that the tetragonal structure becomes preferred than the cubic $L2_1$ structure with the excess Mn, and the different Mn content results in different types of tetragonal structure. These results are in good agreement with the experimental results which evidenced that the excess Mn content enhances the stability of the martensite [11]. Moreover, for each off-stoichiometric concentration,

there exist two local minima, with the one being higher than the other, as shown in Fig. 3.2 (a). The structure corresponding to the lower minimum should be the stable structure, whereas that to the higher minimum should be the metastable structure. Taking the concentration of 29.25 at. % Mn as an example, one can find that the stable structure is the one with c/a = 0.81, and the metastable structure is the one with c/a = 1.14. Furthermore, to find out the relationship between the possible preferred stable structure and the excess Mn contents, the tetragonal distortion with $c/a > 1$ and $c/a < 1$ possessing local minimum energy at different Mn concentrations were fitted, and the curves are displayed in Fig. 3.2 (b). In general, the curves of the relative ground state energy as a function of the c/a ratio show a parabolic shape for both $c/a < 1$ and $c/a > 1$ distortions in the off-stoichiometric $Ni_{50}Mn_xIn_{50-x}$ alloys. For the tetragonal distortion with $c/a > 1$, the c/a value corresponding to the local minimum energy increases with the increased Mn content first and then decreases. However, for the tetragonal distortion with $c/a < 1$, the tendency is opposite. The c/a value corresponding to the local minimum energy decreases first and then increases when the Mn concentration is larger than 34.5 at. %. As the tetragonal distortion c/a value of the stable and metastable structure varies with Mn concentration, for clarity, the stable and metastable state corresponding to the two types of local minimum energy were highlighted with the histograms at each composition in Fig. 3.2 (b). It is seen that the stable structure shifts from the tetragonal structure with $c/a < 1$ to $c/a > 1$ with the increasing Mn concentration, whereas the metastable structure changes from the tetragonal structure with $c/a > 1$ to $c/a < 1$. The stable structure with tetragonal distortion $c/a < 1$ only appears in the alloy with 29.25 at. % Mn. When the Mn concentration further increases to 34.5 at. % and above, the stable structures are those with tetragonal distortion $c/a > 1$. Therefore, we could deduce that the tetragonal structure stability would be enhanced with the extra Mn added, and the preferred martensitic structure changes from

the tetragonal structure with $c/a < 1$ to that with $c/a > 1$. This result agrees with the observation that the alloys with lower Mn concentration showed the tetragonality related to the modulated structures [13], and the alloys with higher Mn concentration showed the tetragonal $L1_0$ structure [11].

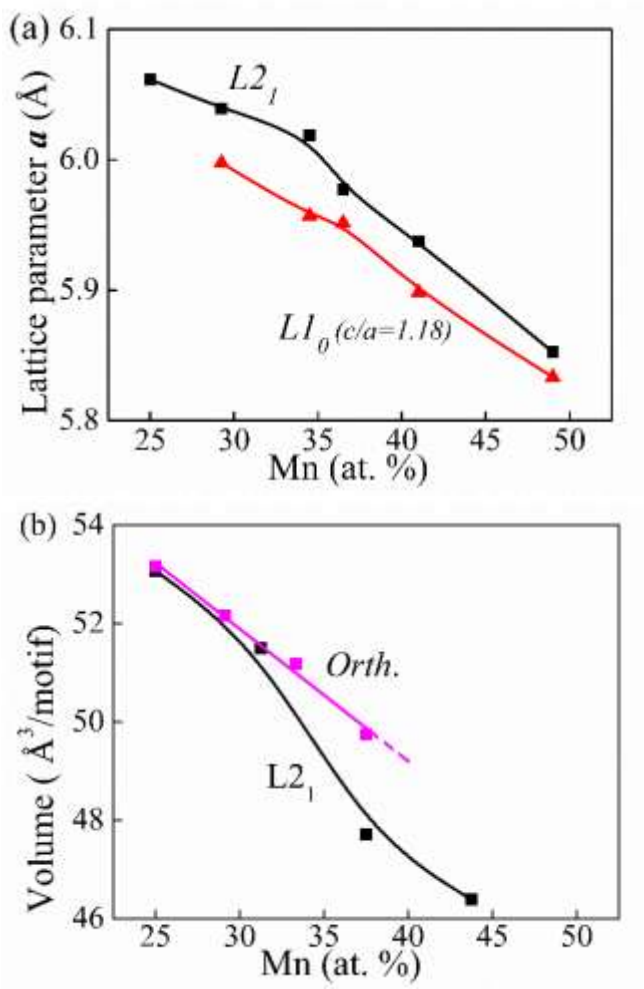

Fig.3.3 (a) Optimized lattice parameter (a) of ferromagnetic cubic $L2_1$ and tetragonal $L1_0$ (c/a = 1.18) structures; (b) optimized cell volume of ferromagnetic cubic $L2_1$ and orthorhombic structures (Dashed-line indicates extrapolation of the fitting.)

Based on the above results of tetragonal distortion, the preference of the martensitic transition to the different tetragonal structures was analyzed for the off-stoichiometric $Ni_{50}Mn_xIn_{50-x}$ alloys with the extra Mn added. As the accurate structure of the preferred martensitic structure under the

effect of the Mn concentration is still not clear, we constructed the tetragonal $L1_0$ structure (space group: *I4/mmm*, [32]) and the orthorhombic structure (originated from the monoclinic *6M* martensite [10]) which correspond to the respective tetragonal structure with $c/a > 1$ and $c/a < 1$ in the tetragonal distortion. The formation energies of the two structures with different Mn concentrations were calculated in the ferromagnetic state, and further compared with that of the perfect cubic $L2_1$ structure. Since the previous experimental observation found that the Curie temperature of the tetragonal martensite ranges from 200 K to 50 K [11,13], we only considered the ferromagnetic state for the martensite with the tetragonal $L1_0$ and the orthorhombic structures in this step. In the present work, firstly, we did the optimization test for the *c/a* values of the tetragonal $L1_0$ structure with a series of lattice parameter (*a*) using the tetragonal distortion under the Equation of State with the Morse function for the $Ni_{50}Mn_{29.25}In_{20.75}$ and $Ni_{50}Mn_{34.5}In_{15.5}$ alloys by the EMTO-CPA. We found that the *c/a* ratio showed little dependence on the Mn concentration. For the *c/a* ratio value around $c/a = 1.18$, the variation is within 0.05. Therefore, we adopt the $c/a = 1.18$ for the tetragonal $L1_0$ structure at all the concentrations for the optimization of their lattice parameter *a*. The optimized lattice parameter (*a*) of the cubic $L2_1$ and the tetragonal $L1_0$ structures in the ferromagnetic ground state is shown in Fig. 3.3 (a). It is seen that the lattice parameters of the two structures show a composition dependence for all the alloys. For the ferromagnetic $L2_1$ structure, the optimized lattice parameter decreases regularly with the increase of the extra Mn. This is consistent with the actual lattice parameter of the ferromagnetic austenite in the stoichiometric alloy ($a = 6.072$ Å) [16] and in the off-stoichiometric alloy ($a = 6.016$ Å) [15]. The lattice parameter (*a*) of the tetragonal $L1_0$ structure shows the same tendency which could be attributed to the smaller atomic radius of the Mn atom. The martensite with an orthorhombic structure was also calculated with volume relaxation for the $Ni_{50}Mn_xIn_{50-x}$ alloys. Since the EMTO-

CPA is too complicated to relax the three lattice parameters, the alloys with different Mn contents were constructed with the supercell method in the VASP with the relaxation of the cell volume and the atom positions. The optimized volume of the cubic $L2_1$ and the orthorhombic (*Orth.*) structures were obtained, and the results are displayed in Fig. 3.3 (b). We truncated the Mn concentration at 37.5 at. % for the orthorhombic structure since the *6M* structure was measured in the Ni-Mn-In alloys with 36 at. % Mn [10]. The volumes of the two structures decrease with the extra Mn added. The volume of the $L2_1$ structure shows an abrupt decrease after 29 at. % and becomes smaller than that of the orthorhombic structure. In contrast, the volume of the orthorhombic structure decreases linearly with the increase of the Mn concentration. Such a volume change tendency is opposite to the experimental observation which demonstrated that the martensite transition from $L2_1$ to the *6M* structure was a volume compression process [33]. This discrepancy may be caused by the original orthorhombic structure setting, as the cell shape was fixed during the calculations.

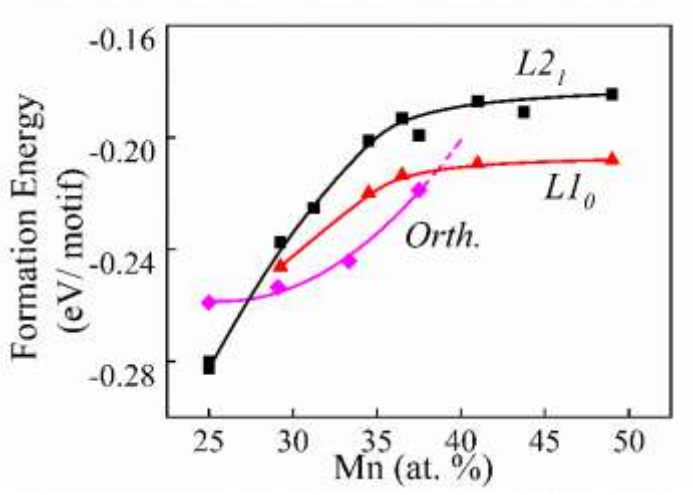

Fig. 3.4 Formation energy of ferromagnetic cubic $L2_1$, tetragonal $L1_0$ with c/a = 1.18 and orthorhombic structures as a function of Mn concentration (Dashed-line indicates extrapolation of the fitting.)

Based on the obtained equilibrium lattice parameters, the formation energies of the cubic $L2_1$, the tetragonal $L1_0$ (c/a = 1.18) and the orthorhombic structures were calculated to analyze the preference of the martensitic structure, as shown in Fig. 3.4. For the stoichiometric $Ni_{50}Mn_{25}In_{25}$

alloy, the cubic $L2_1$ structure still possesses the lowest formation energy. This result further confirms that the stoichiometric cubic structure is the stable structure at 0 K, which agrees with the above tetragonal distortion results (Fig. 3.2 (b)). With the excess Mn added, the formation energies of the three structures increase with the Mn content. This indicates that the stability of all the three structures of the off-stoichiometric $Ni_{50}Mn_xIn_{50-x}$ alloys with the extra Mn would be lowered. The tetragonal $L1_0$ and the orthorhombic structures show lower formation energy than the cubic $L2_1$ structure at the compositions higher than 29 at. % Mn, indicating that the two kinds of martensite are more stable than the cubic austenite with the excess Mn added in the off-stoichiometric $Ni_{50}Mn_xIn_{50-x}$ alloys in the ferromagnetic state. Comparing the formation energy of the cubic $L2_1$ with that of the orthorhombic structure, one can find that the difference increases first and then decreases with the largest formation energy difference appearing at about 33 at. % Mn (Fig. 3.4). However, the formation energy difference between the cubic $L2_1$ and the tetragonal $L1_0$ structures increases first and then keeps roughly constant at compositions higher than 40 at. % Mn (Fig. 3.4). If we compare the formation energies between the two kinds of martensite, we can also find that the orthorhombic structure with about 29 at. % Mn is lower, meaning that the orthorhombic martensite is more stable. This is consistent with the result of the tetragonal distortion test during which the most stable tetragonal structure with $c/a < 1$ appears in the alloy having 29.25 at. % Mn (Fig. 3.2 (b)). However, according to the variation tendency of the formation energies of the two kinds of martensite, the formation energy of the tetragonal $L1_0$ structure becomes smaller than that of the orthorhombic structure at about 40 at. %. This is different from the result predicted by the above tetragonal distortion analysis (Fig. 3.2 (b)). In that prediction, the smallest Mn content when the tetragonal $L1_0$ structure becomes stable is about 34.5 at. % (Fig. 3.2 (b)). The discrepancy may be caused by the different first principle methods for the tetragonal distortion in the tetragonal $L1_0$

and the orthorhombic structure calculations, each having a different relaxation limitation. Despite the discrepancy, this result indicates that the orthorhombic structure is preferred between 29 at. % and 40 at. % Mn, and the tetragonal $L1_0$ structure becomes more stable at the compositions above 40 at. % Mn. Thus, the orthorhombic structure is preferred at lower Mn concentrations, and the tetragonal $L1_0$ structure becomes favored at higher Mn concentrations. This result agrees with the previous report that the ground state structure of the $Ni_{50}Mn_xIn_{50-x}$ (with $29 \leq x \leq 40$) alloy is the modulated martensite with the monoclinic structure, and the ground state structure of the $Ni_{50}Mn_xIn_{50-x}$ (with $40 \leq x \leq 50$) alloy is the non-modulated martensite with the tetragonal $L1_0$ structure [11,34]. Thus, we could deduce that the excess Mn would enhance the possibility of the martensitic transition from the austenite with the cubic structure to the martensite with the orthorhombic or the tetragonal structure. The preferred martensitic structure between the orthorhombic and the tetragonal $L1_0$ structure is determined by the Mn concentration.

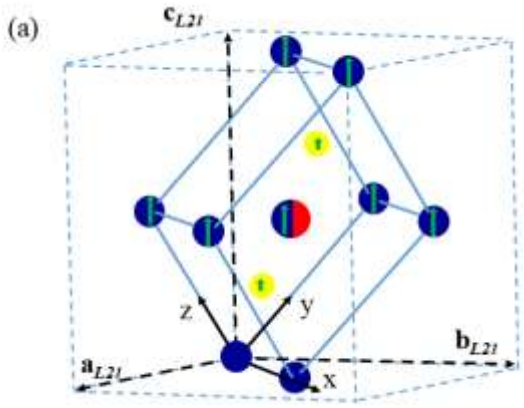

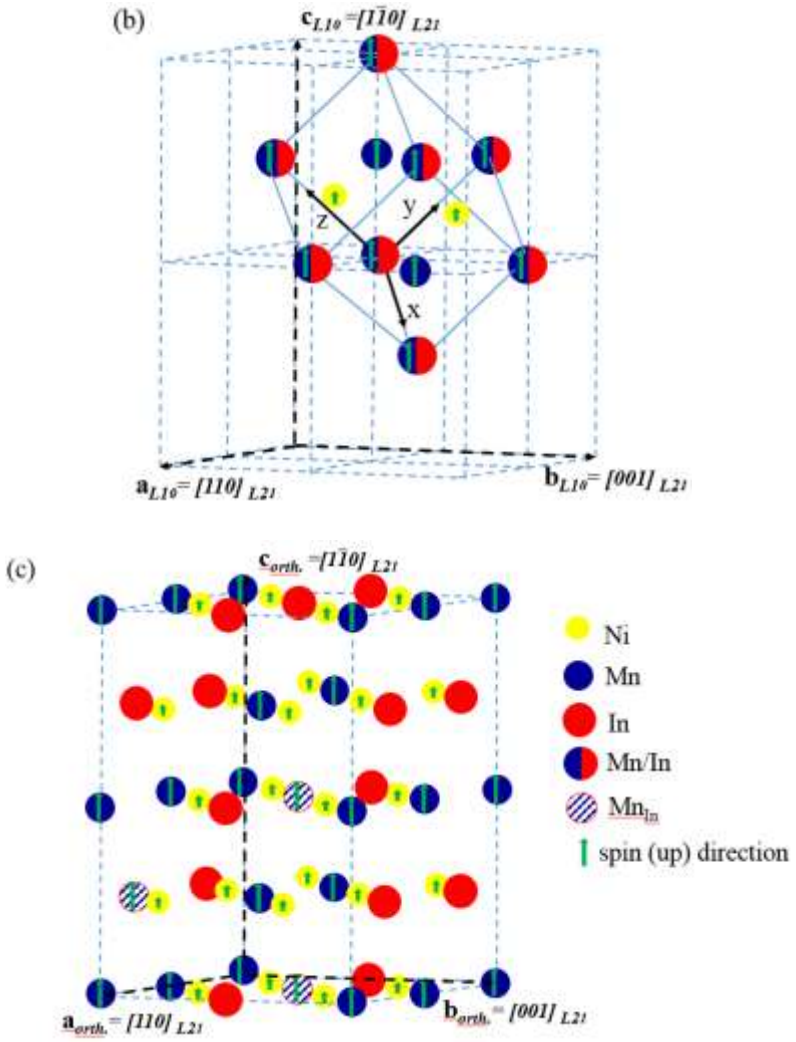

Fig. 3.5 (a) Primitive cell of cubic $L2_1$ structure, (b) primitive cell of tetragonal $L1_0$ structure and (c) conventional cell of orthorhombic structure of ferromagnetic off-stoichiometric $Ni_{50}Mn_xIn_{50-x}$ alloy (34.375 at. % Mn) with excess Mn substituting for In. The spin-up directions of atomic sites are indicated. (Mn/In indicates the excess Mn and In at the same site. Mn_{In} indicates the excess Mn substituting for In.)

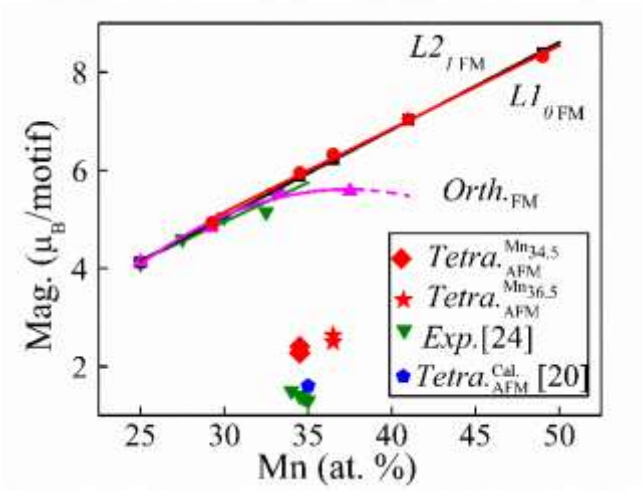

Fig. 3.6 Total magnetic moment of cubic $L2_1$, tetragonal $L1_0$ and orthorhombic structure in off-stoichiometric $Ni_{50}Mn_xIn_{50-x}$ alloys with different Mn contents in the ferromagnetic state and tetragonal structures of $Ni_{50}Mn_{34.5}In_{15.5}$ and $Ni_{50}Mn_{36.5}In_{13.5}$ alloys at ferromagnetic and antiferromagnetic coexisting state. (Dashed-line indicates extrapolation of the fitting.)

Furthermore, with the aim to figure out the effect of the Mn concentration on the magnetic properties of the three structures, the total magnetic moment of one motif of the three structures was also calculated for the off-stoichiometric alloys with different Mn contents in the ferromagnetic state. As an example, the unit cells of the alloy with 34.375 at. % Mn are illustrated in Fig. 3.5, where the spin (up) direction of each atomic site is indicated. In the figure, the $L2_1$ and $L1_0$ structures were constructed by the Coherent Potential approximation [35] (Fig. 3.5 (a) and (b)). However, the orthorhombic structure was constructed by the supercell approach [36] (Fig. 3.5 (c)), and here we show it conventional cell with 32 atoms. The calculated magnetic moment results are displayed in Fig. 3.6. It is seen that the total magnetic moment of the cubic $L2_1$ and that of the tetragonal $L1_0$ structure show an increase with the excess Mn concentration for all the compositions, and the magnetic moment difference between the martensite and the austenite is quite small. For the ferromagnetic orthorhombic structure, the total magnetic moment shows a parabolic tendency which increases with the Mn content first and then tends to decrease after the 37.5 at. % Mn content.

We could find that the total magnetic moment of the alloys with Mn content less than 34 at. % increases with the Mn content, which agrees with the experimental measurements [22]. There is no decrease in the total magnetic moment of all the structures with different Mn content in the ferromagnetic state in the present work. However, in Ref. [22], the total magnetic moment was found to decrease abruptly above 34 at. % Mn.

Then, we carried out the calculation on the total magnetic moment of the 34.5 at. % and the 36.5 at. % Mn alloy with the tetragonal structure. These two compounds possess the local minimum energy in the tetragonal distortion (*i.e.*, the tetragonal structure with $c/a < 1$ corresponds to the orthorhombic martensite, and $c/a > 1$ corresponds to the tetragonal $L1_0$ martensite). During the calculation, the magnetic structure was optimized. Compared with the ferromagnetic martensite, the total magnetic moment of the martensite with tetragonal structures for these two alloys shows an abrupt decrease to around 2.5 μ_B. The magnetic moment of the Ni atoms shows antiferromagnetism with a value of about - 0.2μ_B and that of Mn shows ferromagnetism with a value decreasing to 2.25 μ_B. The results suggest the coexistence of the ferromagnetism and antiferromagnetism in these two concentrations. The antiferromagnetic interaction could be originated from the Ni-Mn hybridization interaction, which is consistent with the theoretical calculation result of the tetragonal structure [19], as displayed in Fig. 3.6. Considering that the Mn content (around 34 at. %) is certificated as the phase transformation point from the cubic to the martensitic structure [11,17], the total magnetic moment of the tetragonal structures with 34.5 at. % and 36.5 at. % Mn were in good agreement with the experimental observation at 5 K [22]. Therefore, we could assert that the excess Mn could linearly enhance the ferromagnetism of the austenite, whereas the excess Mn results in a more complex magnetic state in the martensite. The higher Mn concentration could give rise to a coexistence of the ferromagnetism and the antiferromagnetism

in the two martensite structures. The antiferromagnetic interaction could be attributed to the Ni-Mn hybridization.

3.5 Conclusions

In the present work, we analyzed the effect of Mn concentration on the preference of martensitic phase transition in off-stoichiometric $Ni_{50}Mn_xIn_{50-x}$ alloys. The structural stability of cubic $L2_1$ austenite, tetragonal $L1_0$, and orthorhombic martensite were evaluated by the first-principle calculations. The formation energies of point defect types (vacancy and antisite) around stoichiometric $Ni_{50}Mn_{25}In_{25}$ alloys in the ferromagnetic state were calculated systematically, and the preference substitution of the excess Mn atoms was then determined. Based on the Mn substitution preference, the tetragonal distortion was calculated for the off-stoichiometric $Ni_{50}Mn_xIn_{50-x}$ alloys with different Mn concentrations by the EMTO-CPA with magnetic structure optimization. The results showed that the tetragonal structure stability could be enhanced with the additional Mn, and the cubic $L2_1$ structure becomes less stable. With the increasing Mn concentration, the preferred stable tetragonal structure evolves from the tetragonal structure with $c/a < 1$ to the one with $c/a > 1$. In order to find out the accurate phase stability of the off-stoichiometric $Ni_{50}Mn_xIn_{50-x}$ alloys with tetragonal structures for both $c/a < 1$ and $c/a > 1$ at 0 K, the formation energies of the tetragonal $L1_0$ and orthorhombic structures were calculated with structure optimization in the ferromagnetic state, respectively. As compared with the cubic $L2_1$ structure, the orthorhombic structure is preferred at lower Mn concentrations, and the tetragonal $L1_0$ structure becomes preferred at higher Mn concentrations. Furthermore, the total magnetic moment of the ferromagnetic cubic $L2_1$ and tetragonal $L1_0$ structures are strengthened with the increase of Mn content, whereas that of the orthorhombic structure shows a parabolic tendency with a decreasing tendency after 37.5 at. % Mn. Under the magnetic structure optimization, the

total magnetic moment of the tetragonal structure decreases abruptly after 34.5 at. % Mn. The high Mn concentration could result in the coexistence of ferromagnetism and antiferromagnetism. The latter could be attributed to the Ni-Mn antiferromagnetic hybridization.

References

1. Chernenko, V.A.; Kokorin, V. V.; Babii, O.M.; Zasimchuk, I.K. Phase diagrams in the Ni-Mn-Ga System under compression. *Intermetallics* **1998**, *6*, 29–34.
2. Ullakko, K.; Huang, J.K.; Kantner, C.; O'Handley, R.C.; Kokorin, V. V. Large magnetic-field-induced strains in Ni_2MnGa single crystals. *Appl Phys Lett* **1996**, *69*, 1966–1968.
3. O'Handley, R.C. Model for strain and magnetization in magnetic shape-memory alloys. *J Appl Phys* **1998**, *83*, 3263–3270.
4. James, R.D.; Wuttig, M. Magnetostriction of martensite. *Philos Mag A* **1998**, *77*, 1273–1299.
5. Kainuma, R.; Imano, Y.; Ito, W.; Sutou, Y.; Morito, H.; Okamoto, S.; Kitakami, O.; Oikawa, K.; Fujita, A.; Kanomata, T.; et al. Magnetic-field-induced shape recovery by reverse phase transformation. *Nature* **2006**, *439*, 957–960.
6. Sutou, Y.; Imano, Y.; Koeda, N.; Omori, T.; Kainuma, R.; Ishida, K.; Oikawa, K. Magnetic and martensitic transformations of NiMnX(X=In, Sn, Sb) ferromagnetic shape memory alloys. *Appl. Phys. Lett.* **2004**, *85*, 4358–4360.
7. Karaman, I.; Karaca, H.E.; Basaran, B.; Lagoudas, D.C.; Chumlyakov, Y.I.; Maier, H.J. Stress-assisted reversible magnetic field-induced phase transformation in Ni_2MnGa magnetic shape memory alloys. *Scr Mater* **2006**, *55*, 403–406.
8. McCormack, R.; de Fontaine, D. First-principles study of multiple order-disorder transitions in Cd_2AgAu Heusler alloys. *Phys Rev B* **1996**, *54*, 9746–9755.
9. Khovailo, V.V.; Takagi, T.; Vasil'ev, A.N.; Miki, H.; Matsumoto, M.; R. Kainuma On Order-Disorder ($L2_1$-> B2') Phase Transition in $Ni_{2+x}Mn_{1-x}Ga$ Heusler Alloys. *Phys Stat Sol* **2001**, *183*, R1–R3.
10. Yan, H.; Zhang, Y.; Xu, N.; Senyshyn, A.; Brokmeier, H.G.; Esling, C.; Zhao, X.; Zuo, L.;

Liang Zuo; Zuo, L. Crystal structure determination of incommensurate modulated martensite in Ni-Mn-In Heusler alloys. *Acta Mater* **2015**, *88*, 375–388.

11. Krenke, T.; Acet, M.; Wassermann, E.F.; Moya, X.; Mañosa, L.; Planes, A. Ferromagnetism in the austenitic and martensitic states of Ni-Mn-In alloys. *Phys Rev B* **2006**, *73*, 174413.

12. Zhang, C.Y.; Zhang, Y.D.; Esling, C.; Zhao, X.; Zuo, L. Crystallographic features of the martensitic transformation and their impact on variant organization in the intermetallic compound $Ni_{50}Mn_{38}Sb_{12}$ studied by SEM/EBSD. *IUCrJ* **2017**, *4*, 700–709.

13. Planes, A.; Mãnosa, L.; Acet, M. Magnetocaloric effect and its relation to shape-memory properties in ferromagnetic Heusler alloys. *J Phys Condens Matter* **2009**, *21*, 223201.

14. Krenke, T.; Duman, E.; Acet, M.; Wassermann, E.F.; Moya, X.; Mañosa, L.; Planes, A. Inverse magnetocaloric effect in ferromagnetic Ni-Mn-Sn alloys. *Nat Mater* **2005**, *4*, 450–454.

15. Oikawa, K.; Ito, W.; Imano, Y.; Sutou, Y.; Kainuma, R.; Ishida, K.; Okamoto, S.; Kitakami, O.; Kanomata, T. Effect of magnetic field on martensitic transition of $Ni_{46}Mn_{41}In_{13}$ Heusler alloy. *Appl. Phys. Lett.* **2006**, *88*, 122507.

16. Li, C.M.; Luo, H.B.; Hu, Q.M.; Yang, R.; Johansson, B.; Vitos, L. Role of magnetic and atomic ordering in the martensitic transformation of Ni-Mn-In from a first-principles study. *Phys Rev B* **2012**, *86*, 214205.

17. Buchelnikov, V.D.; Entel, P.; Taskaev, S. V.; Sokolovskiy, V. V.; Hucht, A.; Ogura, M.; Akai, H.; Gruner, M.E.; Nayak, S.K. Monte Carlo study of the influence of antiferromagnetic exchange interactions on the phase transitions of ferromagnetic Ni-Mn-X alloys (X = In, Sn, Sb). *Phys Rev B* **2008**, *78*, 184427.

18. Umetsu, R.Y.; Fujita, A.; Ito, W.; Kanomata, T.; Kainuma, R. Determination of the magnetic ground state in the martensite phase of Ni-Mn-Z (Z = In, Sn and Sb) off-stoichiometric Heusler alloys by nonlinear AC susceptibility. *J Phys Condens Matter* **2011**, *23*, 326001.

19. Priolkar, K.R.; Bhobe, P.A.; Lobo, D.N.; D'Souza, S.W.; Barman, S.R.; Chakrabarti, A.; Emura, S. Antiferromagnetic exchange interactions in the $Ni_2Mn_{1.4}In_{0.6}$ ferromagnetic Heusler alloy. *Phys Rev B* **2013**, *87*, 144412.

20. Priolkar, K.R.; Lobo, D.N.; Bhobe, P.A.; Emura, S.; Nigam, A.K. Role of Ni-Mn hybridization in the magnetism of the martensitic state of Ni-Mn-In shape memory alloys. *EPL* **2011**, *94*, 38006.

21. Umetsu, R.Y.; Kusakari, Y.; Kanomata, T.; Suga, K.; Sawai, Y.; Kindo, K.; Oikawa, K.; Kainuma, R.; Ishida, K. Metamagnetic behaviour under high magnetic fields in $Ni_{50}Mn_{50-x}In_x$ (x= 14.0 and 15.6) shape memory alloys. *J Phys D Appl Phys* **2009**, *42*, 075003.

22. Kanomata, T.; Yasuda, T.; Sasaki, S.; Nishihara, H.; Kainuma, R.; Ito, W.; Oikawa, K.; Ishida, K.; Neumann, K.; Ziebeck, K.R.A. Magnetic properties on shape memory alloys $Ni_2Mn_{1+x}In_{1-x}$. *J Magn Magn Mater* **2009**, *321*, 773–776.

23. Şaşıoğlu, E.; Sandratskii, L.M.; Bruno, P. First-principles calculation of the intersublattice exchange interactions and Curie temperatures of the full Heusler alloys Ni_2MnX (X = Ga, In, Sn, Sb). *Phys Rev B* **2004**, *70*, 024427.

24. Şaşıoğlu, E.; Sandratskii, L.M.; Bruno, P. Role of conduction electrons in mediating exchange interactions in Mn-based Heusler alloys. *Phys Rev B* **2008**, *77*, 064417.

25. Kresse, G.; Furthmüller, J. Efficient iterative schemes for ab initio total-energy calculations using a plane-wave basis set. *Phys Rev B* **1996**, *54*, 11169–11186.

26. Cao, P.; Tian, F.; Wang, Y. Effect of Mo on the phase stability and elastic mechanical properties of Ti-Mo random alloys from ab initio calculations. *J Phys Condens Matter* **2017**, *29*, 435703.

27. Tian, F.; Wang, Y.; Vitos, L. Impact of aluminum doping on the thermo-physical properties of refractory medium-entropy alloys. *J Appl Phys* **2017**, *121*, 015105.

28. Li, C.M.; Hu, Q.M.; Yang, R.; Johansson, B.; Vitos, L. Understanding the martensitic phase transition of $Ni_2(Mn_{1-x}Fe_x)Ga$ magnetic shape-memory alloys from theoretical calculations. *Phys Rev B* **2015**, *91*, 174112.

29. Perdew, J.P.; Burke, K.; Ernzerhof, M. Generalized gradient approximation made simple. *Phys Rev Lett* **1996**, *77*, 3865–3868.

30. Ayuela, A.; Enkoraara, J.; Ullakko, K.; R. M. Nieminen Structural properties of magnetic Heusler alloys. *J Phys Condens Matter* **1999**, *11*, 2017–2026.

31. Godlevsky, V. V; Rabe, K.M. Soft tetragonal distortions in ferromagnetic Ni_2MnGa and related materials from first principles. *Phys Rev B* **2001**, *63*, 134407.

32. Cong, D.Y.; Zetterström, P.; Wang, Y.D.; Delaplane, R.; Peng, R.L.; Zhao, X.; Zuo, L. Crystal structure and phase transformation in $Ni_{53}Mn_{25}Ga_{22}$ shape memory alloy from 20 K to 473 K. *Appl Phys Lett* **2005**, *87*, 111906.

33. Li, Z.; Jiang, Y.; Li, Z.; Valdés, C.F.S.; José Luis Sánchez Llamazares; Yang, B.; Zhang, Y.; Esling, C.; Zhao, X.; Zuo, L. Phase transition and magnetocaloric properties of $Mn_{50}Ni_{42-x}Co_xSn_8$ ($0 \leq x \leq 10$) melt-spun ribbons. *IUCrJ* **2018**, *5*, 54–66.

34. Pathak, A.K.; Khan, M.; Dubenko, I.; Stadler, S.; Ali, N. Large magnetic entropy change in $Ni_{50}Mn_{50-x}In_x$ Heusler alloys. *Appl Phys Lett* **2007**, *90*, 262504.

35. Vitos, L. *Computational quantum mechanics for materials engineers: the EMTO method and applications*; Springer US: Boston, MA, 2005; ISBN 9781846289507.

36. David Sholl; Steckel, J.A. *Density functional theory: a practical introduction*; New Jersey, Canada, 1999;

Chapter 4 Composition dependent thermal excited contributions to phase stability of ferromagnetic $Ni_{50}Mn_xIn_{50-x}$ alloys at finite temperatures

4.1 Outline

In present chapter, by considering the effect of the Mn concentration and the thermally excited contributions (including the vibrational, electronic excitation and magnetic contributions) on the austenite and the martensite phase stability from 0 K to finite temperatures, the martensitic phase stability of the Heusler type Ni-Mn-In shape memory alloy was studied by the first-principle calculations using exact muffin-tin orbitals with coherent potential approximation (EMTO-CPA). Based on this, the martensitic transformation tendency was explored. The formation energies of the two phases were obtained with 5 different Mn compositions at 0 K. Furthermore, based on the equilibrium states, the vibrational and electronic entropies of the two phases were calculated. Further, the influences of the Mn content and the temperature were simulated on the magnetic moment of both phases in their ferromagnetic state.

4.2 Introduction

The off-stoichiometric Heusler typed Ni-Mn-X alloys (X: In, Sb and Sn) undergo a martensitic phase transition from austenite with a cubic $L2_1$ structure to martensite with a modulated structure (such as *6M* [1], *10M* [2], *4O* [3]) or non-modulated $L1_0$ structure [4] around the room temperature, during which the alloy demonstrates shape memory and magnetocaloric effects. The phase diagrams of the $Ni_{50}Mn_xIn_{50-x}$ alloys - established either from experimentally measured data [2,5,6] or from the theoretical prediction by DFT calculation at 0 K [7] - show that the martensitic transition temperature varies with the Mn composition and increases drastically with the addition of Mn. In general, the vibrational entropy has an important influence on the martensitic transition.

So far, two simulation approaches have been mainly used to investigate the vibrational contribution. The one is the accurate and classic quasi-harmonic approximation [8–11], and the other is the efficient and practical Debye model [12–15]. For the Ni-Mn-X alloys in the ferromagnetic state, the magnetic entropy also makes a significant contribution to the martensitic transition. This can be explored by the fix-spin moment approach [11] and the Debye Bragg-Williams approach [14]. As reported by the previous studies on the Ni-Mn-In alloys, the cubic phase tends to transform into the tetragonal phase when the excess Mn is added [2,5–7]. During the process, the magnetic transition from the ferromagnetic state to the ferromagnetic and antiferromagnetic coexisting state may occur in the off-stoichiometric $Ni_{50}Mn_xIn_{50-x}$ alloys with $L1_0$ structures at 0 K [16]. By combining the ab-initio calculations with the Monte Carlo simulation, the complex magnetic contribution from ferromagnetic and antiferromagnetic interactions in the tetragonal phase was investigated on the $Ni_{50}Mn_{34}In_{16}$ alloy at finite temperatures [17]. However, there are less systematical investigations on the influence of the Mn content on the thermodynamic stability of the austenite and martensite of Ni-Mn-In alloys at finite temperatures by considering all the thermally excited contributions. Clearly, the phase stability of the austenite and the martensite could be affected not only by chemical composition, but also by temperature. The former influences the atom and electronic interactions, and the latter affects the phonon and electronic excitations. Therefore, to figure out the effect of these factors on the martensitic phase transition, the thermodynamic stability should be quantitatively evaluated on the thermal physical origins (including the vibrational, electronic excitation and magnetic entropy) for the austenite and the martensite. Such an investigation could not easily be conducted by experiments. Theoretical simulation by the first-principle calculations could be an effective approach.

The conventional first-principle calculations can be employed to obtain the information about crystal structure, electronic structure and magnetic moment of the phases at ground state, and it is powerful in exploring composition effect on phase stability at 0 K [18]. However, to predict the martensitic phase transition, which always occurs at finite temperatures and is affected by the thermally excited entropies, the first-principle calculations show certain limitations. To figure out the temperature excitations, the ab-initio simulation combined with the integrated approaches could be applied to obtain the different thermodynamic entropies [19] for the analysis on the temperature-driven phase transition of alloys with different compositions.

In the present work, we made an attempt to work out the influences of Mn content and temperature on phase stabilities of austenite and martensite in 5 $Ni_{50}Mn_xIn_{50-x}$ alloys. The thermodynamic contributions to the phase stability at finite temperatures, including the vibrational, electronic excitation and magnetic contribution, were studied. The phase stability of the ground state of the austenite with an ordered $L2_1$ structure and the martensite with a non-modulated (NM) tetragonal structure with different Mn contents were analyzed through calculating their total energies at 0 K. Then, the temperature excitation entropic contributions (vibrational and electronic) were calculated at different Mn contents. The relationship between the magnetic moment and the Mn content was also investigated at finite temperatures.

4.3 Computational method: theory and methodology

In the framework of the Density Functional Theory (DFT) [19], the plane-wave basis projector augmented wave (PAW) method with the generalized-gradient approximation (GGA-PBE) [20] was used in the exact muffin-tin orbital method combined with the coherent potential approximation (EMTO-CPA) [21]. The ferromagnetic interactions of atoms were set for both austenite and martensite phases. Although the martensite phase has two kinds of structures (the

modulated martensite with monoclinic structure, and the non-modulated martensite with tetragonal structure), only the non-modulated $L1_0$ structure was used to calculate the martensite phase stability, as the modulated structure was considered to consist of twin related $L1_0$ structures (the so-called adaptive structure) [22]. The convergence criterion of energy was 10^{-6} eV. A 13 × 13 × 13 k-point sampling mesh was set for the ferromagnetic austenite and martensite with 4 atoms, respectively. The lattice parameters of ground state for the two phases with different Mn contents were determined by the equation of states (EOS) with the Morse function [12] and were used as the equilibrium configurations for the further finite temperature calculations. According to the experimental observations [1,23], the extra Mn atom prefers to substitute In and stays at In site.

To determine the thermodynamic properties of crystalline materials, the temperature and volume related formulation of the Helmholtz free energy [15,24,25] should be used, as follows:

$$F(V,T) = E_{0K}(V) + F_{el}(V,T) + F_{vib}(V,T) + F_{mag}(V,T) - T * S_{conf}(T) \tag{4.1}$$

In the equation, E_{0K} is the static lattice total energy at 0 K and is only volume dependent. F_{vib}, F_{el} and F_{mag}, are the vibrational, electronic excitation and magnetic free energies, respectively, and they are both volume and temperature dependent. S_{conf} is the configurational entropy. The vibrational contribution was simulated in the frame of the efficient quasi-harmonic Debye-Grüneisen model using the Gibbs2 code [26–28]. The electronic excitation contribution was calculated with the EMTO [21] using the finite temperature Fermi distribution [29,30]. Here, we only calculated the magnetic moment at finite temperatures to predict the variation of the magnetic entropy at finite temperatures using the EMTO [21]. The temperature dependent magnetic moment was derived from the magnetic free energy ($F_{mag}(T,\mu) = -TS_{mag}(\mu)$), where the magnetic entropy was estimated by the mean-field approach ($S_{mag}(\mu) = k_B \log(\mu_i + 1)$, in which μ_i is the magnetic moment of atom *i*) [15,31–34].

Entropy change during the martensitic transformation can be defined as [14]:

$$\Delta S^{tr.} = S^{mar.} - S^{aus.} \tag{4.2}$$

Since the martensitic transition is diffusionless in the Ni-Mn-In alloys, the change of the configurational entropy is zero [35], and the anharmonic contributions is also negligible. Therefore, only the three main contributions should be taken into consideration for the Ni-Mn-In alloys [36–38]:

$$\Delta S = \Delta S_{vib} + \Delta S_{ele} + \Delta S_{mag} \tag{4.3}$$

4.4 Results and discussion

Based on the equilibrium energies of the austenite and the NM martensite, we first analyzed the effect of Mn concentration on the ground state stability in terms of the static lattice contribution at 0 K which is the most important part of the conventional contribution to the free energy. Fig. 4.1 presents the equilibrium energy difference ($\Delta E = E^{mar.} - E^{aut.}$) between the two phases in the ferromagnetic state as a function of Mn content at 0 K. It is seen that a positive value (0.026 eV) is reached at 25 at. % Mn, which indicates that the austenite is more stable than the martensite in the stoichiometric alloy. Apart from this, the energy differences of all compositions with excess Mn are negative, *i.e.* the total energy of the martensite is lower than that of the austenite at 0 K. This suggests that the ground state of the off-stoichiometric $Ni_{50}Mn_xIn_{50-x}$ alloys is the martensite. Moreover, with the increase of the Mn content, the energy differences between the two phases decrease monotonously. This indicates that the stability of the NM martensite becomes higher with the increasing Mn content. This tendency is in good accordance with what predicted from the phase diagram of Ni-Mn-In alloys [2,7] which showed that the NM martensite with $L1_0$ structure is stable at high Mn concentration. Such a tendency was also observed in the experiments, *e.g.* the $Ni_{50}Mn_{50}$

alloys have a tetragonal structure at room temperature [4] and the martensitic transition temperature of the ferromagnetic martensite increases dramatically with the extra Mn [5,39]. However, the total energies obtained in the present work were calculated with the atoms fixed at their equilibrium positions at 0 K. In reality, the martensitic transitions of the Ni-Mn-In alloys were observed at different temperatures below or above room temperature [5]. Therefore, the temperature related entropy changes due to thermal excitation are essential to understand the phase transitions of the off-stoichiometric $Ni_{50}Mn_xIn_{50-x}$ alloys.

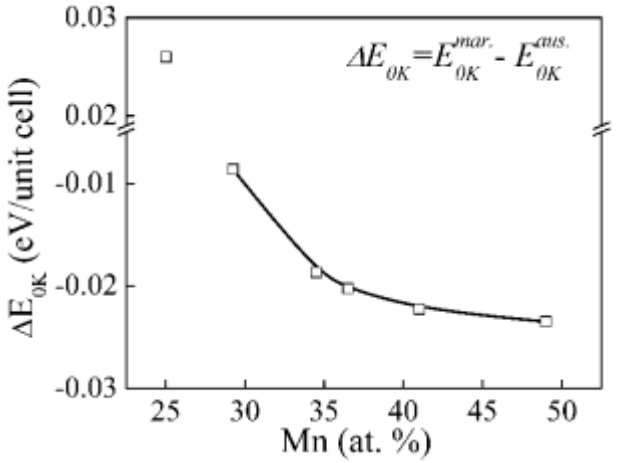

Fig. 4.1 Total ground state energy differences between austenite and NM martensite of $Ni_{50}Mn_xIn_{50-x}$ alloys

Then, we analyzed the temperature excitations (including the vibrational, electronic excitation and magnetic entropies) of the off-stoichiometric $Ni_{50}Mn_xIn_{50-x}$ alloys. Firstly, the vibrational entropy (S_{vib}) arising from the phonon interactions was calculated based on the equilibrium structures obtained at 0 K. The results are shown in Fig. 4.2. One can find that the vibrational entropy value of the austenite is higher than that of the NM martensite for all Mn contents. This indicates that the vibrational entropy contributes to destabilizing austenite at elevated temperatures. The lower vibrational entropy value of the NM martensite can be attributed to its close-packed structure and to the existence of the soft modes in the austenite before the martensitic transition

[40]. From Fig. 4.2, one can also find that the vibrational entropies of the two phases increase sharply in the whole investigated temperature range (from 100 to 600 K). At 100 K, the vibrational entropies of the two phases are very close. This may be due to the fact that 100 K is too low to excite the phonon interactions. Moreover, for the NM martensite, the different amount of the extra Mn does not provoke big change in their vibrational entropies at all temperatures from 100 K to 600 K. The similar situation can be also observed in the off-stoichiometric austenite. However, a certain difference appears between the stoichiometric austenite and the off-stoichiometric austenite from 200 K to 500 K. With the addition of the extra Mn, the vibrational entropy of austenite decreases sharply. This suggests that the phase stability of the off-stoichiometric austenite is lowered with respect to that of the stoichiometric austenite. As for the vibrational entropy difference between the two phases, it increases with the increase of the temperature at all Mn contents.

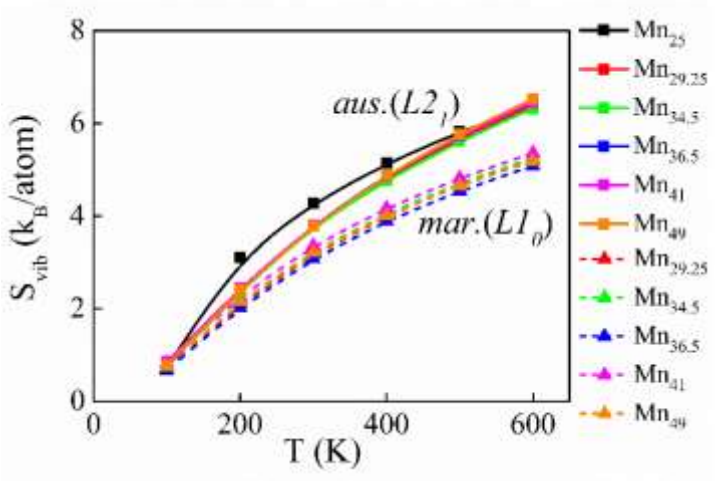

Fig. 4.2 Vibrational entropy of austenite and NM martensite of $Ni_{50}Mn_xIn_{50-x}$ alloys at finite temperatures with different Mn content

To clearly figure out the entropy differences between the two phases and estimate the phase transition tendency at each Mn content, the vibrational entropy difference ($\Delta S_{vib}^{tr.}$) between the

austenite and the NM martensite were also calculated for the 5 Mn contents at finite temperatures, and the results are displayed in Fig. 4.3. It is seen that the values of the vibrational entropy differences are negative and decrease sharply with temperature for all Mn compositions. When the Mn content is 36.5 at. %, the vibrational entropy difference possesses the lowest value at all the temperatures. The martensitic phase transition from the austenite to the martensite could take place when the $\Delta S_{vib}^{tr.} = S_{vib}^{mar.} - S_{vib}^{aus.} < 0$, according to the classic thermodynamics rule [14,41]. From the increased difference between the two phases, we could draw a conclusion that the vibrational contribution further enhances the martensitic transition, and the extra Mn also promotes the transition at finite temperatures.

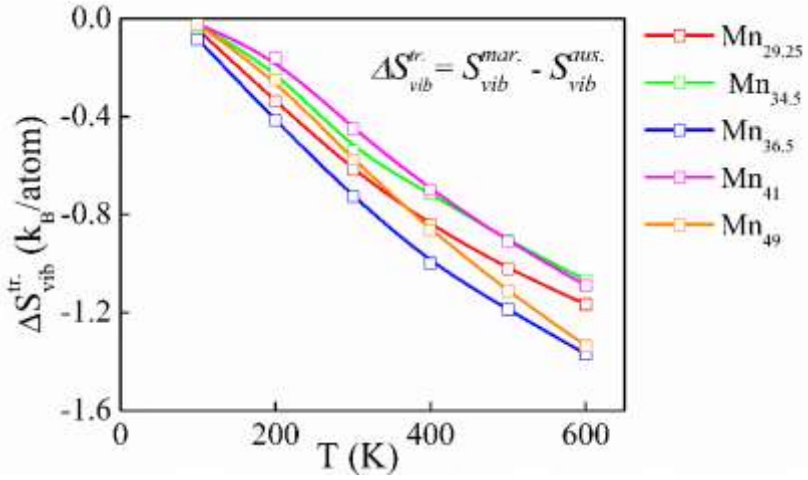

Fig. 4.3 Vibrational entropy change between austenite and NM martensite of $Ni_{50}Mn_xIn_{50-x}$ alloy with Mn concentrations at different temperatures.

As the second possible contribution to the phase stability comes from the electronic excitation entropy, we further calculated the electronic excitation entropies of the two phases with different Mn compositions at finite temperatures. Here, the electronic entropies of the $Ni_{50}Mn_{29.25}In_{20.75}$ alloy were presented in Fig. 4.4, for instance, as the electronic entropies of the two phases for the 4 other concentrations show the same tendency and have the similar magnitude. It is seen that the electronic

excitation entropies (S_{el}) of the two phases increase with the increased temperature and the electronic entropy of the NM martensite is smaller than that of the austenite, which is consistent with the influential tendency of the vibrational entropy (Fig. 4.2). Compared with the vibrational contribution, although the electronic excitation contribution is quite small, it is in the same direction to promote the martensitic transition.

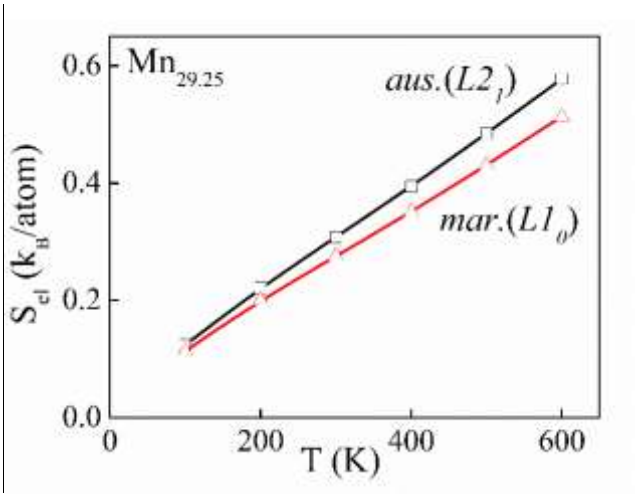

Fig. 4.4 Electronic entropy of austenite and NM martensite in $Ni_{50}Mn_{29.25}In_{20.75}$ alloy at finite temperatures.

In addition to the two kinds of temperature-excitation entropies calculated above, the magnetic entropy also plays an important role in phase stability. As the magnetic moment lies at the origin of the magnetic entropy and is correlated with the magnetic entropy according to the mean-field approach [15,32], we further calculated the magnetic moments of the two phases with different Mn contents at finite temperatures. Here, we set the two phases in the ferromagnetic state. As the Curie temperatures were measured to be around 300 K [2,7] for the austenite and 200 K for the martensite [17], the magnetic moments of the martensite and austenite were calculated at temperatures below their respective Curie temperatures. In Fig. 4.5, the total magnetic moments of the unit-cell austenite and martensite were each plotted as a function of the Mn content at finite temperatures. For comparison, the experimental results at 5 K [6] and the ab-initio simulation results at 0 K [16]

were also displayed in the figure. Fig. 4.5 (a) shows that the magnetic moments of the austenite increase with the Mn contents at 0 K and 300 K, which means that the ferromagnetism of the austenite is enhanced by the added Mn. Based on the related expressions in the mean-field approach, we can deduce that an increased magnetic moment will contribute to a larger magnetic entropy at high temperatures [15,32]. Thus, the added Mn increases the magnetic entropy of the austenite. However, the amount of magnetic moment of the austenite is only sensitive to Mn content but indifferent to temperature. As shown in Fig. 4.5 (a). for the same alloy, the magnetic moment at 0 K is almost the same as that at 300 K. This indicates that the effect of temperature excitation is less effective than the that of the Mn content. For the NM martensite, it is seen from Fig. 4.5(b) that the magnetic moment increases linearly with the Mn content in the ferromagnetic state, and the magnitudes at 0 K and 200 K are very close. When compared with the simulated magnetic moments of $L1_0$ martensite at 0 K from Ref. [16] where both the ferromagnetic and antiferromagnetic states were considered, an accordance between our calculated results and the data from Ref. [16] is reached at 29 at. % Mn. As discovered by the Monte Carlo simulation [17], the existence of the antiferromagnetic interaction decreases the overall magnetic moment of the Ni-Mn-In alloys. The disagreement of our results at the Mn contents higher than 29 at. % in Fig. 4.5(b) indicates that a change of magnetic nature (to paramagnetic or antiferromagnetic) in the martensite phase occurs when the Mn content is increased [5]. Such a discrepancy is due to the fact that we set the two phases in the ferromagnetic state within the EMTO. Thus, the magnetic state of the phases was kept ferromagnetic during the whole calculation process and no magnetic transition was allowed.

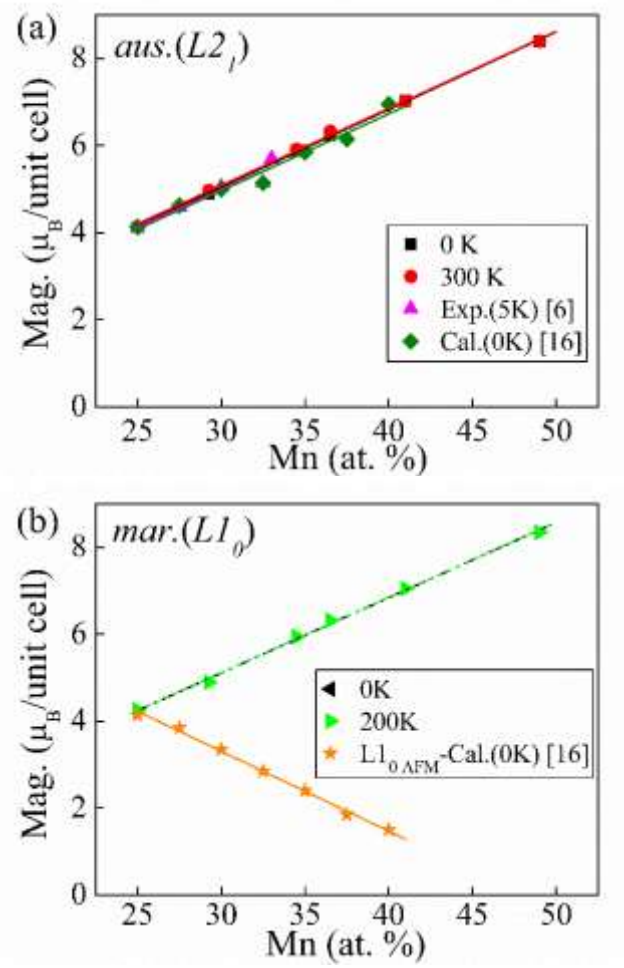

Fig. 4.5 Magnetic moment variation with Mn content (a) austenite (b) NM martensite of $Ni_{50}Mn_xIn_{50-x}$ alloy, together with data from previous research

As only the *L1₀* structured martensite with the Mn content around 29 at. % is still dominated by the ferromagnetic state, the temperature excitation on the magnetic moments of the ferromagnetic austenite and the ferromagnetic martensite was further analyzed and compared for the alloy with 29.25 at. % Mn. The results are shown in Fig. 4.6. It is seen that the magnetic moment of the austenite shows a quick increase with temperature and then slightly decrease to the Curie temperature, whereas that of the NM martensite slightly decreases with the increase of temperature to the Curie temperature. However, above 100 K, the magnetic moments of the austenite are higher than those of the martensite. This means that the magnetic contribution also promotes the phase

transformation like the vibrational and electronic contributions. This tendency agrees with the experimental observation but the total magnetic change is not obvious. It may be caused by the disorder of the magnetic moment at high temperatures and this could be modified by the local disorder local moment (DLM) approach [42] around the transition temperatures.

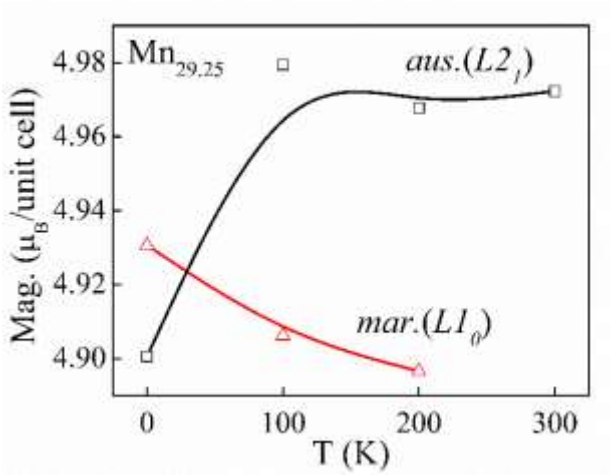

Fig. 4.6 Total magnetic moments of austenite and NM martensite in $Ni_{50}Mn_{29.25}In_{20.75}$ alloy at finite temperatures

Using the conventional method, frozen magnon approach [31], to model the magnetic free energies is in general a challenging task from first-principles in multi-component alloy systems. Therefore, mean field approximation could be implemented to estimate the S_{mag}, especially under the high-temperature limitation. Therefore, in this Chapter, the magnetic moments were determined as a function of temperature (T) which is obtained from the equilibrium volume at the ground state at 0K. From Fig. 4.7 (a), the magnetic moment of Mn sited on the normal Mn site in $L2_1$ structure is much larger than that of the NM structure. The magnetic moment of Mn decreases monotonically in $L2_1$ structure, whereas it variates at finite temperature with Mn content in NM structure. As shown in Fig. 4.7 (b), the magnetic moment of extra Mn substituted on the In site decreases linearly in both phases with the increasing Mn content at finite temperatures. With the Mn content below 41 at. %, the magnetic moment of extra-Mn substituted on In site is larger than the Mn site on the

normal Mn site in both phases. When the Mn content reaches the 49 at. %, the magnetic moment of both kinds of Mn are almost the same. The magnetic moment of the NM phase is larger than that of *L2₁* phase. Compared with the effect of the temperature, the Mn content plays an essential effect on the magnetic moment of Mn site on In and normal Mn sites.

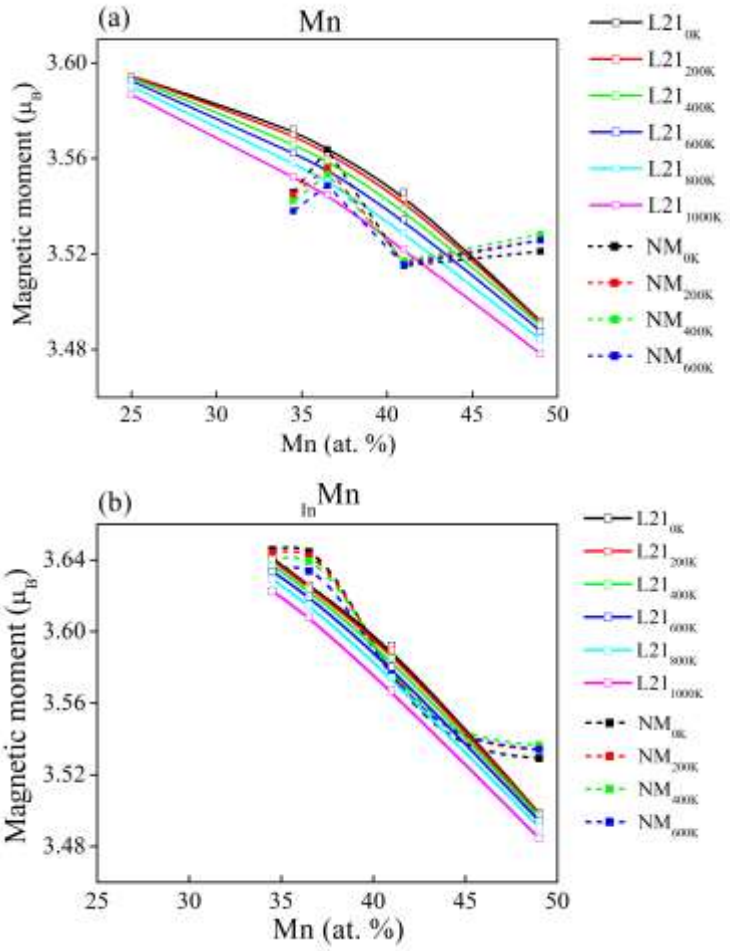

Fig. 4.7 Magnetic moment fluctuation of Mn (a) substituted on normal Mn site (b) substituted on In site of austenite and martensite in Ni-Mn-In alloy with different Mn contents at finite temperatures

As shown in Fig. 4.7 (c), the magnetic moment of Ni of NM phase is larger than the values of *L2₁* phase with the Mn content below 41 at. %, whereas it increases slowly after 41 at. % Mn content and becomes smaller than that of *L2₁* phase at 49 at. %, which is opposite to the variation of the Mn magnetic moment. The magnetic moments of In are negative in all alloys shown in Fig.

4.7 (d). In *L2₁* phase, the values keep similar at different temperature with different Mn content. And the magnetic moment of In varies slightly when the Mn content reaches the 49 at. % in the NM.

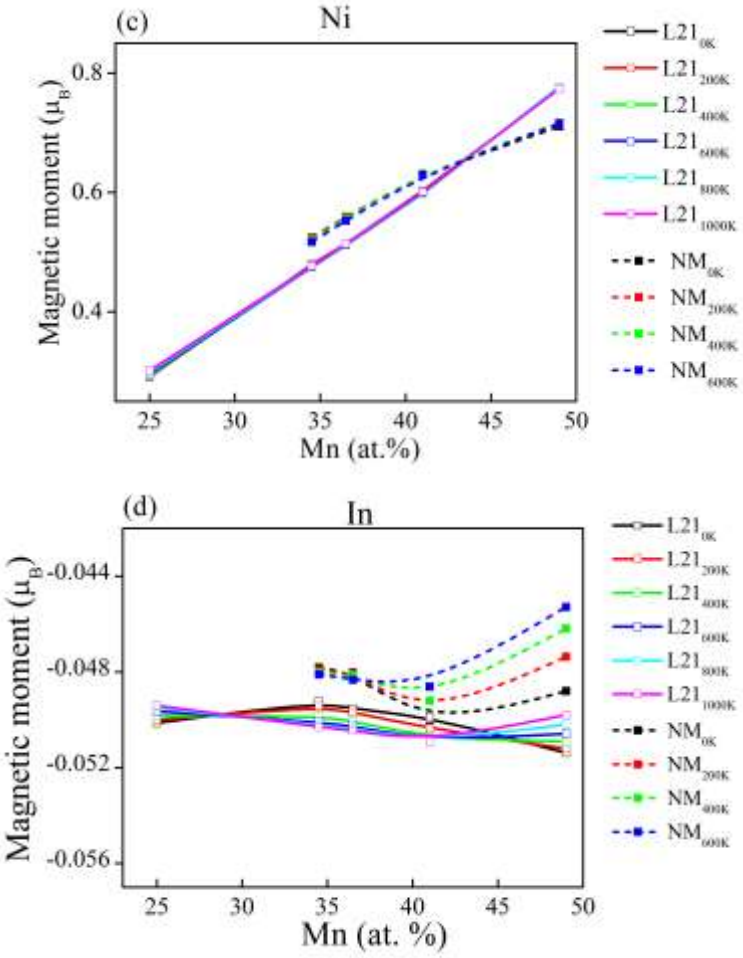

Fig. 4.7 Magnetic moment fluctuation of Ni (c) and In (d) of austenite and martensite in Ni-Mn-In alloy with different Mn contents at finite temperatures

4.4 Conclusions

In this work, the effects of Mn content and the three main thermally excited contributions on phase stability of the ordered cubic *L2₁* austenite and the non-modulated tetragonal martensite were investigated from 0 K to finite temperatures for the $Ni_{50}Mn_xIn_{50-x}$ alloys and the martensitic

transformation possibility was evaluated. The simulation was implemented by the first-principle calculations combined with the integration approach using the EMTO-CPA software.

1) At 0 K, the addition of the extra Mn can lower the phase stability of austenite and increase that of martensite through affecting their static lattice contributions, leading to an enhanced martensitic transformation tendency. The effect increase with the increase of Mn content.
2) For the vibrational contribution at finite temperatures, the addition of the extra Mn leads to a sharp decrease of the vibrational entropy of the austenite with respect to that of the martensite, which indicates a reduced phase stability of the austenite. The negative vibrational entropy difference between the martensite and the austenite increases with the temperature, which indicates an enhanced phase transition possibility.
3) For the electronic excitation contribution, it is quite small under the excess Mn and the temperature excitation, compared with the vibrational contribution, but shows the same tendency to promote the martensitic transition.
4) For the magnetic contributions of the two phases in the ferromagnetic state, the total magnetic moment of austenite increases with the increase of the Mn content, which should result in an increase of the magnetic entropy. The total magnetic moment of the martensite demonstrates the same tendency with the Mn content, but it is always lower than that of the austenite. Thus, the magnetic contribution is also favorable for martensitic transition.

The results of the present work provide new information on the effects of Mn content and thermally excited contributions on phase stabilities of both austenite and martensite of Heusler typed $Ni_{50}Mn_xIn_{50-x}$ shape memory alloys to evaluate their martensitic transformation tendencies.

Reference

1. Yan, H.L.; Zhang, Y.D.; Xu, N.; Senyshyn, A.; Brokmeier, H.-G.; Esling, C.; Zhao, X.; Zuo, L. Crystal structure determination of incommensurate modulated martensite in Ni-Mn-In Heusler alloys. *Acta Mater* **2015**, *88*, 375–388.
2. Krenke, T.; Acet, M.; Wassermann, E.F.; Moya, X.; Mañosa, L.; Planes, A. Ferromagnetism in the austenitic and martensitic states of Ni-Mn-In alloys. *Phys Rev B* **2006**, *73*, 174413.
3. Zhang, C.Y.; Zhang, Y.D.; Esling, C.; Zhao, X.; Zuo, L. Crystallographic features of the martensitic transformation and their impact on variant organization in the intermetallic compound $Ni_{50}Mn_{38}Sb_{12}$ studied by SEM/EBSD. *IUCrJ* **2017**, *4*, 700–709.
4. Planes, A.; Mãnosa, L.; Acet, M. Magnetocaloric effect and its relation to shape-memory properties in ferromagnetic Heusler alloys. *J Phys Condens Matter* **2009**, *21*, 223201.
5. Sutou, Y.; Imano, Y.; Koeda, N.; Omori, T.; Kainuma, R.; Ishida, K.; Oikawa, K. Magnetic and martensitic transformations of NiMnX(X = In, Sn, Sb) ferromagnetic shape memory alloys. *Appl. Phys. Lett.* **2004**, *85*, 4358–4360.
6. Kanomata, T.; Yasuda, T.; Sasaki, S.; Nishihara, H.; Kainuma, R.; Ito, W.; Oikawa, K.; Ishida, K.; Neumann, K.; Ziebeck, K.R.A. Magnetic properties on shape memory alloys $Ni_2Mn_{1+x}In_{1-x}$. *J Magn Magn Mater* **2009**, *321*, 773–776.
7. Entel, P.; Siewert, M.; Gruner, M.E.; Chakrabarti, A.; Barman, S.R.; Sokolovskiy, V. V.; Buchelnikov, V.D. Optimization of smart Heusler alloys from first principles. *J Alloys Compd* **2013**, *577S*, S107–S112.
8. Planes, A.; Mañosa, L.; Ríos-Jara, D.; Ortín, J. Martensitic transformation of Cu-based shape-memory alloys: elastic anisotropy and entropy change. *Phys Rev B* **1992**, *45*, 7633–7639.

9. Xie, J.J.; de Gironcoli, S.; Baroni, S.; Scheffler, M. First-principles calculation of the thermal properties of silver. *Phys Rev B* **1999**, *59*, 965–969.

10. Uijttewaal, M.A.; Hickel, T.; Neugebauer, J.; Gruner, M.E.; Entel, P. Understanding the phase transitions of the Ni_2MnGa magnetic shape memory system from first principles. *Phys Rev Lett* **2009**, *102*, 035702.

11. Dutta, B.; Çaklr, A.; Giacobbe, C.; Al-Zubi, A.; Hickel, T.; Acet, M.; Neugebauer, J. Ab initio prediction of martensitic and intermartensitic phase boundaries in Ni-Mn-Ga. *Phys Rev Lett* **2016**, *116*, 025503.

12. Moruzzi, V.L.; Janak, J.F.; Schwarz, K. Calculated thermal properties of metals. *Phys Rev B* **1988**, *37*, 790–799.

13. Shang, S.L.; Wang, Y.; Kim, D.; Liu, Z.K. First-principles thermodynamics from phonon and Debye model: Application to Ni and Ni_3Al. *Comput Mater Sci* **2010**, *47*, 1040–1048.

14. Pérez-Landazábal, J.I.; Recarte, V.; Sanchez-Alarcos, V.; Ruiz, M.J.; Cesari, E. Outstanding role of the magnetic entropy in arrested austenite in an ordered $Ni_{45}Mn_{36.7}In_{13.3}Co_5$ metamagnetic shape memory alloy. *Scr Mater* **2019**, *168*, 91–95.

15. Ma, D.; Grabowski, B.; Körmann, F.; Neugebauer, J.; Raabe, D. Ab initio thermodynamics of the CoCrFeMnNi high entropy alloy: Importance of entropy contributions beyond the configurational one. *Acta mater* **2015**, *100*, 90–97.

16. Li, C.M.; Luo, H.B.; Hu, Q.M.; Yang, R.; Johansson, B.; Vitos, L. Role of magnetic and atomic ordering in the martensitic transformation of Ni-Mn-In from a first-principles study. *Phys Rev B* **2012**, *86*, 214205.

17. Buchelnikov, V.D.; Entel, P.; Taskaev, S. V.; Sokolovskiy, V. V.; Hucht, A.; Ogura, M.; Akai, H.; Gruner, M.E.; Nayak, S.K. Monte Carlo study of the influence of

antiferromagnetic exchange interactions on the phase transitions of ferromagnetic Ni-Mn-X alloys (X = In, Sn, Sb). *Phys Rev B* **2008**, *78*, 184427.

18. Kresse, G.; Furthmüller, J. Efficiency of ab-initio total energy calculations for metals and semiconductors using a plane-wave basis set. *Comput Mater Sci* **1996**, *6*, 15–50.
19. Grabowski, B.; Söderlind, P.; Hickel, T.; Neugebauer, J. Temperature-driven phase transitions from first principles including all relevant excitations: the fcc-to-bcc transition in Ca. *Phys Rev B* **2011**, *84*, 214107.
20. Perdew, J.P.; Burke, K.; Ernzerhof, M. Generalized gradient approximation made simple. *Phys Rev Lett* **1996**, *77*, 3865–3868.
21. Vitos, L. *Computational quantum mechanics for materials engineers: the EMTO method and applications*; Springer US: Boston, MA, 2005; ISBN 9781846289507.
22. Kaufmann, S.; Rößler, U.K.; Heczko, O.; Wuttig, M.; Buschbeck, J.; Schultz, L.; Fähler, S. Adaptive modulations of martensites. *Phys Rev Lett* **2010**, *104*, 145702.
23. López-García, J.; Sánchez-Alarcos, V.; Recarte, V.; Pérez-Landazábal, J.I.; Fabelo, O.; Cesari, E.; Rodríguez-Velamazán, J.A. Routes for enhanced magnetism in Ni-Mn-In metamagnetic shape memory alloys. *Scr Mater* **2019**, *167*, 21–25.
24. Wallace, D.C. *Thermodynamics of Crystals*; Dover books on physics; Dover Publications, 1998; ISBN 9780486402123.
25. Grabowski, B.; Hickel, T.; Neugebauer, J. Ab initio study of the thermodynamic properties of nonmagnetic elementary fcc metals: Exchange-correlation-related error bars and chemical trends. *Phys Rev B* **2007**, *76*, 024309.
26. Blanco, M.A.; Francisco, E.; Luaña, V. GIBBS: Isothermal-isobaric thermodynamics of solids from energy curves using a quasi-harmonic Debye model. *Comput Phys Commun*

2004, *158*, 57–72.

27. Otero-De-La-Roza, A.; Abbasi-Pérez, D.; Luaña, V. Gibbs2: A new version of the quasiharmonic model code. II. Models for solid-state thermodynamics, features and implementation. *Comput Phys Commun* **2011**, *182*, 2232–2248.
28. Otero-De-La-Roza, A.; Luaña, V. Gibbs2: A new version of the quasi-harmonic model code. I. Robust treatment of the static data. *Comput Phys Commun* **2011**, *182*, 1708–1720.
29. Mermin, N.D. Thermal properties of the inhomogeneous electron gas. *Phys Rev* **1965**, *137*, 1441–1443.
30. Marx, D.; Hutter, J. Ab initio molecular dynamics: Theory and implementation. In *Modern Methods and Algorithms of Quantum Chemistry*; 2000; Vol. 1, pp. 301–449 ISBN 3000056181.
31. Halilov, S. V.; Perlov, A.Y.; Oppeneer, P.M.; Eschrig, H. Magnon spectrum and related finite-temperature magnetic properties: A first-principle approach. *Europhys Lett* **1997**, *39*, 91–96.
32. Körmann, F.; Dick, A.; Grabowski, B.; Hallstedt, B.; Hickel, T.; Neugebauer, J. Free energy of bcc iron: Integrated ab initio derivation of vibrational, electronic, and magnetic contributions. *Phys Rev B* **2008**, *78*, 033102.
33. Li, C.M.; Luo, H. Bin; Hu, Q.M.; Yang, R.; Johansson, B.; Vitos, L. First-principles investigation of the composition dependent properties of $Ni_{2+x}Mn_{1-x}Ga$ shape-memory alloys. *Phys Rev B* **2010**, *82*, 024201.
34. Şaşıoğlu E, Sandratskii L M and Bruno P 2004 First-principles calculation of the intersublattice exchange interactions and Curie temperatures of the full Heusler alloys Ni_2MnX (X = Ga, In, Sn, Sb) *Phys Rev B* **70** 024427.

35. Mañosa, L.; Planes, A.; Ortín, J.; Martínez, B. Entropy change of martensitic transformations in Cu-based shape memory alloys. *Phys Rev B* **1993**, *48*, 3611–3619.

36. Stipcich, M.; Marcos, J.; Mañosa, L.; Planes, A.; Romero, R. Low-temperature entropy in Cu-based shape-memory alloys and the boson peak. *Phys Rev B* **2003**, *68*, 214302.

37. Recarte, V.; Pérez-Landazábal, J.I.; Gómez-Polo, C.; Sánchez-Alarcos, V.; Cesari, E.; Pons, J. Vibrational and magnetic contributions to the entropy change associated with the martensitic transformation of Ni-Fe-Ga ferromagnetic shape memory alloys. *J Phys Condens Matter* **2010**, *22*, 416001.

38. Khovailo, V.V.; Oikawa, K.; Abe, T.; Takagi, T. Entropy change at the martensitic transformation in ferromagnetic shape memory alloys. *J Appl Phys* **2003**, *93*, 8483–8485.

39. Umetsu, R.Y.; Kusakari, Y.; Kanomata, T.; Suga, K.; Sawai, Y.; Kindo, K.; Oikawa, K.; Kainuma, R.; Ishida, K. Metamagnetic behaviour under high magnetic fields in $Ni_{50}Mn_{50-x}In_x$ (x = 14.0 and 15.6) shape memory alloys. *J Phys D Appl Phys* **2009**, *42*, 075003.

40. Moya, X.; González-Alonso, D.; Mañosa, L.; Planes, A.; Garlea, V.O.; Lograsso, T.A.; Schlagel, D.L.; Zarestky, J.L.; Aksoy, S.; Acet, M. Lattice dynamics in magnetic superelastic Ni-Mn-In alloys: Neutron scattering and ultrasonic experiments. *Phys Rev B* **2009**, *79*, 214118.

41. Umetsu, R.Y.; Ito, W.; Ito, K.; Koyama, K.; Fujita, A.; Oikawa, K.; Kanomata, T.; Kainuma, R.; Ishida, K. Anomaly in entropy change between parent and martensite phases in the $Ni_{50}Mn_{34}In_{16}$ Heusler alloy. *Scr mater* **2009**, *60*, 25–28.

42. Staunton, J.; Gyorffy, B.L.; Pindor, A.J.; Stocks, G.M.; Winter, H. The "disordered local moment" picture of itinerant magnetism at finite temperatures. *J Magn Magn Mater* **1984**, *45*, 15–22.

Chapter 5 Conclusions and perspectives

From the above theoretical calculations, the following important conclusions could be drawn:

Effect of effective Coulomb and exchange parameters on phase stability, structural and magnetic properties of $Ni_{50}Mn_{25}In_{25}$ alloys

The effect of the Hubbard *U* and *J* coupling parameters on the phase stability, structural and magnetic properties of the ferromagnetic austenite with a cubic $L2_1$ structure in the stoichiometric $Ni_{50}Mn_{25}In_{25}$ alloy were simulated with the *Vienna Ab-initio Simulation Package* (VASP) in the frame of the density-functional theory using the plane-wave pseudopotential calculations. The the phase stability of the ordered $Ni_{50}Mn_{25}In_{25}$ austenite with the effective Coulomb and exchange *U* and *J* parameters was firstly investigated in the present work. The effect of the effective Coulomb and exchange *U* and *J* parameters on the optimized structural parameters, the phase stability (including the ground state energy, the formation energy and the elastic constants), and the electronic structure (including the magnetic moment, the band structure and the density of states and the charge density difference) of the cubic stoichiometric $Ni_{50}Mn_{25}In_{25}$ austenite were obtained. The results of the first principle calculations with the *GGA + U* approach of the cubic $L2_1$ austenite of $Ni_{50}Mn_{25}In_{25}$ alloy were as below.

i) The optimized lattice parameters vary with the effective Coulomb and exchange *U* and *J* parameters around the experimentally evaluated value. With all the *J* values, the lattice parameters *a* become extremely close at *U* equal to 6. The ground state energy arrives at a stable stage when *J* equal to 0.5. The elastic constants and the bulk modulus change with *U* and *J* coupling, whereas they do not show any evident tendency to affect the phase stability. Based on the optimization of the lattice parameter and the magnetic

moment and the minimum ground state energy variation for further physical properties analysis, the effective Coulomb and exchange parameters of U = 6 eV and J = 0.5 were chosen for further calculation.

ii) With the exchange-correlation GGA + U (U = 6 eV and J = 0.5) method, the lattice parameter of the austenite increases slightly. Compared with the calculation without considering the effective Coulomb and exchange parameters, the magnetic moment increase slightly. However, the calculation showed a higher formation energy, which means that the consideration of the Hubbard U and J coupling reduced the stability of the $L2_1$ structure.

iii) The effects of the effective Coulomb and exchange parameters on the electronic structure were obtained by band structure, density of states and charge density difference. With some slight influence on the spin coupling, no obvious change was detected around the Fermi Level. With the effective Coulomb and exchange parameters U and J coupling, the bandgap still shows the metallic bonding in the cubic austenite $Ni_{50}Mn_{25}In_{25}$ alloy.

We first tried to systematically calculate the physical properties of the cubic austenite of the $Ni_{50}Mn_{25}In_{25}$ alloy by considering the effective Coulomb and exchange U and J parameter into the exchange correlation by the *GGA* using the VASP with an aim to modulate more accurately for the metal transition element Ni and Mn with *3d* orbitals. Since there is no obvious effect on the equilibrium crystal structure or the electronic structure, we could deduce that there is no need to add the efficient Coulomb parameter into the physical property simulation of the Heusler typed Ni-Mn-In alloys by the first-principle calculations.

Composition dependent martensitic structural preference of $Ni_{50}Mn_xIn_{50-x}$ alloys by VASP and EMTO-CPA method

The effect of the Mn concentration on the martensitic phase transition preference was analyzed, and the structural stability of the cubic $L2_1$ austenite, the tetragonal $L1_0$ and the orthorhombic martensite of the off-stoichiometric $Ni_{50}Mn_xIn_{50-x}$ alloys were evaluated by the first-principle calculations by taking the stoichiometric $Ni_{50}Mn_{25}In_{25}$ alloy as the reference. The ground state energy resolved tetragonal distortion revealed that the excess Mn changes the preferred stable structure from the perfect cubic $L2_1$ structure to the tetragonally distorted structures, and the stable tetragonal structure would shift from the tetragonal distortion with $c/a < 1$ to c/a >1 with the increase of the Mn concentration. Furthermore, to find out more accurate preference of the martensitic structure, the formation energies were calculated using different relaxation methods by the chemical disorder method with a 4-atom cell by the EMTO-CPA for the tetragonal $L1_0$ structure and the supercell method with a 96-atom cell with the VASP for the orthorhombic structure at 0 K in the ferromagnetic state. The results show that, compared with the perfect cubic $L2_1$ structure of the stoichiometric $Ni_{50}Mn_{25}In_{25}$ alloy, the orthorhombic structure is preferred at lower Mn concentrations which are between 29 at. % and 40 at. % Mn, whereas the tetragonal $L1_0$ structure is more stable at the higher Mn concentrations which are above 40 at. % Mn. Furthermore, the effect of the Mn concentration on the magnetic properties was also calculated, and it shows that the magnetic moment of the cubic $L2_1$ structure increases linearly with the excess Mn in the ferromagnetic state, whereas it varies with the Mn concentration in the two kinds of martensite. The excess Mn could lead to the coexistence of ferromagnetism and antiferromagnetism, and the appearance of the antiferromagnetism could be arisen from the Ni-Mn antiferromagnetic interaction in the tetragonal martensite.

Composition dependent thermal excited contributions to phase stability of ferromagnetic $Ni_{50}Mn_xIn_{50-x}$ alloys at finite temperatures

To figure out the martensitic phase stability of the $Ni_{50}Mn_xIn_{50-x}$ alloys, the thermodynamic contributions, including the vibrational, the electronic excitation and the magnetic contribution, were calculated with 5 different Mn contents for the austenite and the martensite at finite temperatures. The ground state phase stability between the austenite with an ordered $L2_1$ structure and the martensite with a non-modulated (*NM*) tetragonal structure were studied through calculating their formation energies at 0 K. Then, the temperature excitation entropic contributions (including vibrational and electronic) were calculated at different Mn contents. The relationship between the magnetic moment and the Mn contents were also investigated at finite temperatures.

By considering the effect of the Mn concentration and the thermally excited contributions (including the vibrational, electronic excitation and magnetic contributions) on the austenite and the martensite phase stability at finite temperatures, the martensitic phase transition mechanism of the Heusler typed Ni-Mn-In shape memory alloys was studied by the first-principle calculations using the exact muffin-tin orbitals with the coherent potential approximation (EMTO-CPA). The formation energies of the two phases were obtained with 5 different Mn compositions at 0 K and the results showed that the NM martensite is more stable than the austenite at high Mn concentrations. Furthermore, for the two phases, the vibrational entropy increases with the rise of the temperature for all the Mn compositions. The additional Mn would decrease the vibrational entropy of the austenite in the off-stoichiometric alloys from 100 K to 600 K. In all the cases (temperature and Mn-content), the austenite has the larger vibrational entropy than that of the martensite, which reveals that the vibrational entropy contributes to promote the martensitic transition. The Mn-content and the temperature show a similar influence on the electronic entropy of the two phases, but the contribution of the electronic entropy is much smaller compared with the vibrational contribution. Furthermore, the influences of the Mn content and the temperature on the magnetic moment of the both phases in their ferromagnetic state were also calculated. The

magnetic moments increase linearly with the Mn-content, however, the influence of temperature is relatively small. Above 100 K, the magnetic moment of the austenite is higher than that of the martensite, suggesting that the magnetic entropy makes a similar contribution to promote the martensitic transformation like that of the vibrational entropy.

Perspectives

Up to now, the Ni-Mn-In ferromagnetic shape memory alloys, which shows promising prospects for the future applications, have been investigated extensively on many aspects by both the experimental and calculational methods. However, there is still a long way before the material could be used in the large-scale practical applications since there are still several essential properties that need to be resolved. The physical properties which could be further explained by the *ab-initio* simulations are summarized as follows:

1) To date, the effect of the Mn concentration on the magnetic properties of the martensite with different structures (including the tetragonal $L1_0$ and the orthorhombic or monoclinic structures) of the off-stoichiometric $Ni_{50}Mn_xIn_{50-x}$ alloys is still lack, especially for the possible physical mechanism of the antiferromagnetic interaction in the martensite structure that still needs to be studied systematically, which could be discovered by the local disorder method within the EMTO or the antiferromagnetic spin-orbital setting within the VASP at 0 K, respectively;
2) The magnetic contribution to the Helmholtz free energy of the martensite at finite temperature, which is critical for the prediction of the phase transformation temperature, is still not very clear. Based on the discovery of the magnetic properties of the martensite at 0 K, the simulations of the magnetic entropy for the modulated martensite with the

orthorhombic or the monoclinic structure (such as *6M*, *10M*, *4O*), will be an important research direction.

Publication list

1. **X.M. Liu**, J.M. Raulot, C. Esling, X. Zhao, L. Zuo, 'Investigation on vibrational, electronic excitation entropy and magnetic moment contributions to phase stability of off-stoichiometric $Ni_{50}Mn_xIn_{50-x}$ alloys at finite temperatures by first-principle calculations', 2020, **Journal of Physics D: Applied Physics**, http://iopscience.iop.org/10.1088/1361-6463/ab9975, online.
2. **X.M. Liu**, J.M. Raulot, C. Esling, X. Zhao, L. Zuo, 'Investigation on the preference of the martensitic structure in off-stoichiometric Ni-Mn-In_5 alloys by first-principle calculations', Journal of Magnetism and magnetic materials, ***waiting for final decision after revision***.

Acknowledgement

The present work is completed at the Laboratoire d'Étude des Microstructures et de Mécanique des Matériaux (LEM3), Université de Lorraine, France, and the Key Laboratory for Anisotropy and Texture of Materials (ATM), Northeastern University, China. I had the honor to work with numerous colleagues in the two laboratories and I would like to give my hearted thanks for their kind help. I gratefully acknowledge the China Scholarship Council (CSC) for providing a Ph.D. scholarship.

I would like to sincerely thank all the jury members for taking time out of their busy schedules to achieve my dissertation defense, and special gratitude to Prof. XXX. And Prof. Daoyong CONG to evaluate my dissertation and provide constructive suggestions.

I sincerely express my deepest gratitude to my supervisors, Prof. Jean-Marc RAULOT at Université de Lorraine, France, and Prof. Liang ZUO at Northeastern University, China, for their guidance and support to my Ph.D. work and their constant and selfless help in my daily life. They are learned, modest, serious and kind supervisors. From them, I have learned not only knowledge but also a precise scientific attitude towards work and persistence to overcome difficulties. I would also like to extend my appreciation to Prof. Claude ESLING, Prof. Xiang ZHAO and Yudong ZHANG for encouraging, supporting, and mentoring me during my Ph.D. study.

I would like to express my thanks to Ms. Jacqueline DECKER, Ms. Arlette JACQUIERRE, at LEM3, Université de Lorraine, France, and Prof. Nan JIA, Prof. Binzong LI, Dr. Bo YANG, Dr. Haile YAN at ATM, Northeastern University, China, for their technical and administrative help and support to my Ph.D. work.

I am also grateful to all the staffs and students in the two labs, LEM3 and ATM, and my friends who shared their experience with me and offered help to my study, especially Prof. Shun

XU, Prof. Ke HUA, Dr. Chunyang ZHANG, Dr. Naifu ZOU, Ms. Qian WANG, Dr. Manoj SUBRAMANI, Mr. Rui XU. Special thanks to Dr. Meishuai LIU, Dr. Cai CHEN, and my young friend Ms. Pengru ZHAO for their endless help and support in my daily life.

Last but not least, I would like to express my deep love and gratitude to my parents, my family and my friend Mr. Lin MA who always show loving, helping, encouraging and supporting me in my life.

Résumé en Français

1. Introduction

Les alliages à mémoire de forme (SMA) peuvent être caractérisés par deux types de comportements: la superélasticité et l'effet de mémoire de forme (SME) [1–4]. La superélasticité est associée à la capacité de récupération des déformations d'origine de chargement sans aucune contrainte résiduelle [5]. Les alliages à mémoire de forme magnétique (MSMA) sont une nouvelle façon de produire du mouvement et de la force [6]. Les alliages à mémoire de forme magnétique produiraient un mouvement qui est associé aux joints de macles des variantes de martensite orientées différemment ou aux interfaces entre l'austénite et la martensite [7]. Il force également la récupération à sa forme d'origine sous un champ magnétique appliqué [6]. Parmi eux, les alliages Ni-Mn-Ga produisent les grandes déformations induites par le champ magnétique [8,9], qui pourraient être déduites de la réorientation des macles de martensite sous le champ magnétique. Cependant, sa contrainte magnétique est assez faible, ce qui est dû à la faible résistance au maclage / démaclage [10]. Pour les alliages Ni-Mn-X (X: In, Sn, Sb), la magnétostriction est attribuée à son réarrangement magnétique des variantes [11–13]. Les alliages à mémoire de forme subissent la transition martensitique de l'austénite ferromagnétique à la martensite faiblement magnétique à basse température [14]. Au cours de ce processus, la température de transition martensitique pourrait être influencée par le champ magnétique, et de nombreuses propriétés physiques uniques se manifesteraient, notamment la magnétorésistance géante, la conductivité magnétothermique et les effets magnétocaloriques inverses [15].

Au cours du processus thermodynamique, un alliage Ni-Mn-In subit une série de transformations qui se traduit par de nombreuses phases différentes avec des structures différentes. La première étape de transition de phase consiste à ce que la masse fondue se solidifie directement dans la phase *B2* intermédiaire partiellement désordonnée [16], et la transition de second ordre *B2* - $L2_1$ a lieu pendant le refroidissement [17]. Ensuite, l'austénite cubique de premier ordre $L2_1$ se transforme en martensite de structures différentes, qui dépendent fortement de la composition chimique autour de l'alliage stoechiométrique Ni-Mn-In [18]. Pour la transition de phase martensitique, les alliages Ni-Mn-In de type Heusler se transforment en deux types de phases martensitiques à basse température: i) la martensite modulée, c'est-à-dire les structures modulées

orthorhombiques ou monocliniques (ie c/a <1, dans le système de coordonnées cubique) avec In appauvri, comme les structures modulées *6M* [19], *10M* [20], *4O* [21]; ii) et la martensite non modulée, c'est-à-dire la structure tétragonale à faible concentration en In, telle que la structure tétragonale non modulée $L1_0$ (c'est-à-dire c/a> 1, dans le système de coordonnées cubiques) [22].

Jusqu'à présent, les alliages Ni-Mn-In de type Heusler ont été étudiés de manière intensive sous de nombreux aspects, y compris la structure cristalline [19,20], la transition de phase martensitique [23-27] et la stabilité de la phase martensitique et les propriétés magnétiques [18, 20,28–30], en utilisant des méthodes expérimentales et informatiques.

Dans le présent travail, nous avons étudié trois aspects des alliages Ni-Mn-In.

1) Nous avons d'abord étudié l'effet des paramètres efficaces de Coulomb et d'échange U et J sur la stabilité de phase, les propriétés structurelles et magnétiques de l'austénite ordonnée de l'alliage $Ni_{50}Mn_{25}In_{25}$.
2) L'effet de la concentration en Mn sur la préférence de la structure martensitique dans les alliages off-stoechiométriques $Ni_{50}Mn_xIn_{50-x}$ a été étudié par la distorsion tétragonale sous optimisation de la structure magnétique. Sur la base des résultats de préférence de structure martensitique, la stabilité de phase du $L1_0$ tétragonal et des structures orthorhombiques à l'état ferromagnétique a été calculée. Les énergies de formation ont été comparées à la structure cubique $L2_1$ des alliages off-stoechiométriques $Ni_{50}Mn_xIn_{50-x}$ avec différentes teneurs en Mn. De plus, l'effet de la concentration de Mn sur le moment magnétique total a été calculé pour les trois structures à l'état ferromagnétique. Le type d'interaction antiferromagnétique au sein de la martensite tétragonale $L1_0$ à l'état ferromagnétique et antiferromagnétique coexistants a également été analysé.
3) Les contributions thermodynamiques, y compris la vibration, l'excitation électronique et la contribution magnétique, ont été calculées avec 5 teneurs en Mn différentes pour les stabilités de phase de l'austénite et de la martensite à températures finies. La stabilité de phase de l'état fondamental de l'austénite avec une structure ordonnée $L2_1$ et de la martensite avec une structure tétragonale non modulée (NM) a été étudiée à 0 K. Ensuite, les contributions entropiques d'excitation de température (vibrationnelles et électroniques) ont été calculées à différents contenu en Mn. La relation entre le

moment magnétique et la teneur en Mn a également été étudiée à des températures finies.

2. Méthode de calcul

Dans ce travail, une série de calculs de premiers principes dans les alliages Ni-Mn-In ont été effectués dans le cadre de la théorie de la densité fonctionnelle (DFT) en utilisant le Vienna Ab initio Software Package (VASP) [31–33] et l'Extra Muffin-Tin Orbital (EMTO) combiné avec le Coherent Potential Approximation (CPA). Le présent travail a été orienté vers l'étude de la stabilité de phase d'austénite et de martensite dans les alliages Ni-Mn-In à 0 K et à températures finies. La méthode Projector Augmented Wave (PAW, [34,35]) a été utilisée. La relaxation de l'atome a été réalisée par un algorithme de gradient conjugué. Les calculs préliminaires ont été exécutés en utilisant l'approximation de gradient généralisé (GGA) de Perdew, Burke et Ernzerhof (PBE) [36]. Les calculs seraient effectués en utilisant la polarisation de spin avec une coupure d'énergie de 420 eV et le Monkhorst-Pack [37] avec 12 × 12 × 12 (pour la cellule primitive austénitique à 4 atomes) des mailles de point k appliquées pour l'intégration de la zone de Brillouin. La valeur des paramètres efficaces de Coulomb U et d'échange J a été testée dans ce travail.

L'énergie de formation (E_f) de la cellule $Ni_2Mn_xIn_{2-x}$ (à 4 atomes) a été déterminée selon la fonction suivante de la concentration en Mn (x):

$$E_f(x) = E_0(Ni_2Mn_xIn_{2-x}) - 2*E_{Ni} - x*E_{Mn} - (2-x)*E_{In} \quad (1)$$

Pour déterminer les propriétés thermodynamiques des matériaux cristallins, la formulation liée à la température et au volume de l'énergie libre de Helmholtz [38–40] doit être utilisée, comme suit:

$$F(V,T) = E_{0K}(V) + F_{el}(V,T) + F_{vib}(V,T) + F_{mag}(V,T) - T*S_{conf}(T) \quad (2)$$

Dans l'équation, E_{0K} est l'énergie totale du réseau statique à 0 K et dépend uniquement du volume. Fvib, Fel et Fmag, sont respectivement l'énergie vibratoire, l'excitation électronique et l'énergie magnétique libre, et elles dépendent à la fois du volume et de la température. Sconf est l'entropie configurationnelle. La contribution vibrationnelle a été simulée dans le cadre du modèle efficace quasi-harmonique de Debye-Grüneisen avec le code Gibbs2 [41–43]. La contribution de l'excitation électronique a été calculée par l'EMTO [44] en utilisant la distribution de Fermi à température finie [45,46]. Ici, nous avons seulement calculé le moment magnétique à des températures finies pour prédire la variation de l'entropie magnétique à température finie, en

utilisant l'EMTO [44]. Le moment magnétique dépendant de la température est dérivé de l'énergie magnétique libre ($F_{mag}(T,\mu) = -TS_{mag}(\mu)$), où l'entropie magnétique a été estimée par l'approche du champ moyen ($S_{mag}(\mu) = k_B \log(\mu_i + 1)$, μ_i est le moment magnétique de l'atome *i*) [15, 31–33].

Le changement d'entropie pendant la transformation martensitique peut être défini comme [50]:

$$\Delta S^{tr.} = S^{mar.} - S^{aus.} \tag{3}$$

La transition martensitique étant sans diffusion dans les alliages Ni-Mn-In, le changement de l'entropie configurationnelle est absent [51] et les contributions anharmoniques peuvent également être négligées.

3. Résultats et discussion

3.1 Effet de Coulomb efficace et des paramètres d'échange sur la stabilité de phase, les propriétés structurelles et magnétiques des alliages $Ni_{50}Mn_{25}In_{25}$

Comme le montre la figure 1, l'austénite et la martensite ont la relation d'orientation: $[1\ 1\ 0]_A//[1\ 0\ 0]_M$, $[0\ 0\ 1]_A//[0\ 1\ 0]_M$, $[1\ -1\ 0]_A//[0\ 0\ 1]_M$.

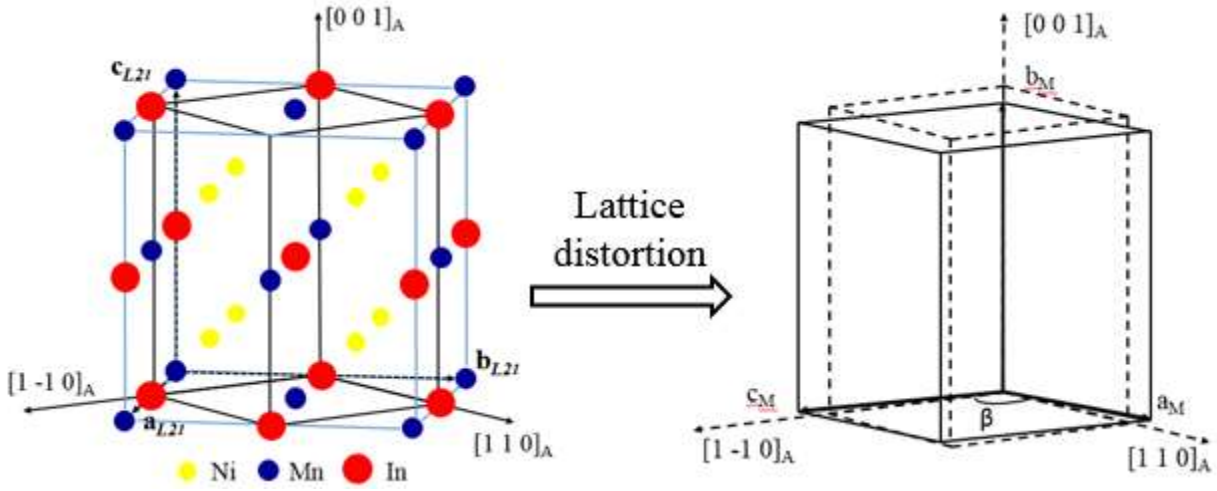

Fig. 1 Relation d'orientation entre l'austénite cubique *L2₁* (A) et la martensite (M), construite selon le modèle de Bain [19].

Sur la base de cette relation d'orientation, nous avons révélé les structures cristallines, magnétiques et électroniques et les propriétés élastiques de l'austénite ferromagnétique de structure *L2₁* pour le $Ni_{50}Mn_{25}In_{25}$ stoechiométrique. Pour ce faire, nous adoptons d'abord le paramètre de réseau expérimental a = 6. 071Å [19] et optimisé pour le volume d'équilibre. Sur la base du paramètre de réseau optimisé, les propriétés de structure de la phase d'austénite ont également été calculées en tenant compte des paramètres de Coulomb efficaces, comme le montre la figure 2. Nous avons d'abord étudié la structure et la stabilité de phase ordonnée de l'alliage d'austénite $Ni_{50}Mn_{25}In_{25}$ avec le Coulomb *U* efficace et les paramètres d'échange *J*. Il a été montré que le paramètre du réseau, les énergies de l'état fondamental varient avec les différents couplages *U* et *J* dans la structure d'austénite *L2₁* de l'alliage $Ni_{50}Mn_{25}In_{25}$. Le moment magnétique a montré la même tendance avec le paramètre de réseau, qui augmente avec le Hubbard *U* ajouté, puis diminue lorsque le *U* est supérieur à 6 eV. Alors que pour l'énergie de l'état fondamental, elle augmente linéairement avec le paramètre Coulomb *U* effectif à toutes les valeurs d'échange *J*. Par conséquent, nous choisissons les paramètres efficaces de Coulomb et d'échange: *U* = 6 eV et *J* = 0,5 pour les analyses plus approfondies de la stabilité de phase.

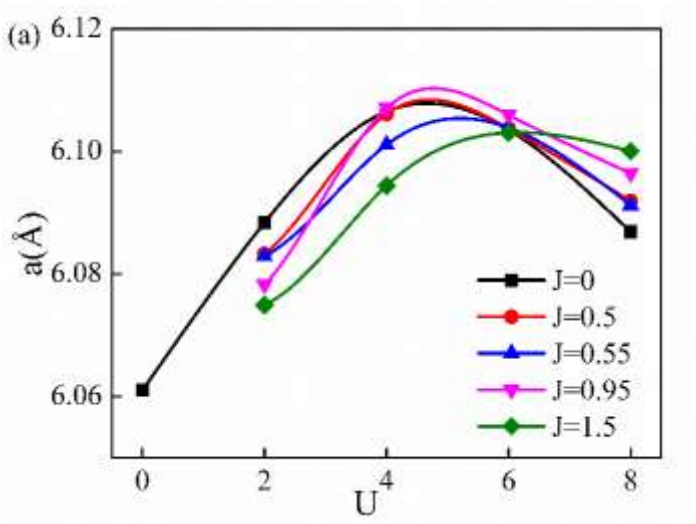

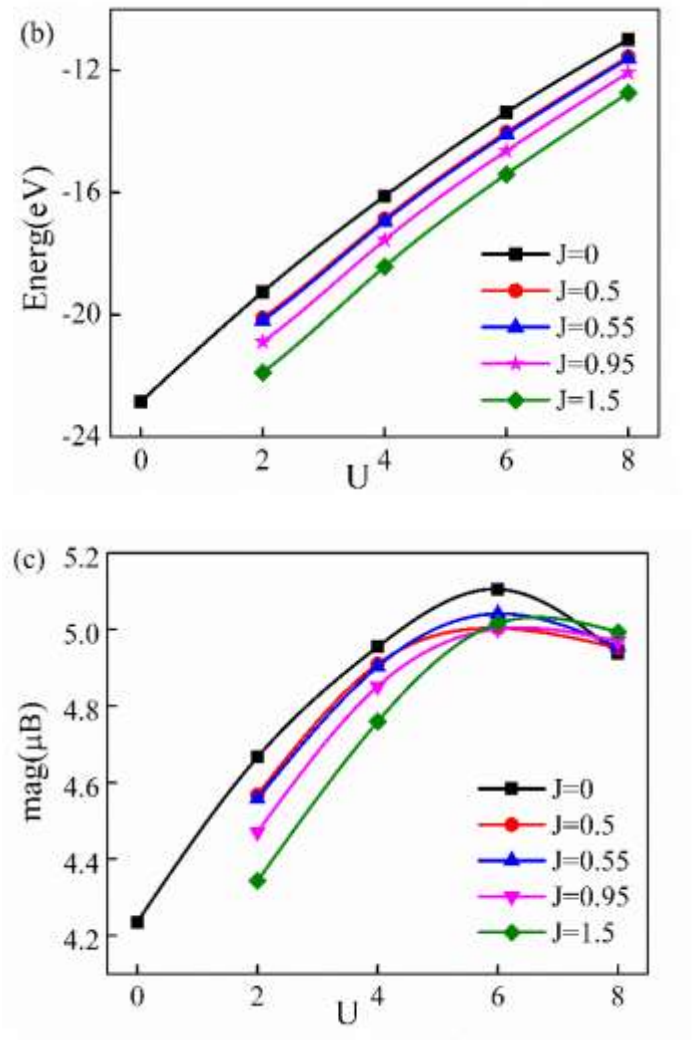

Fig. 2 Variations de (a) paramètre de réseau optimisé; b) énergie à l'état fondamental; (c) moment magnétique total de l'austénite en alliage $Ni_{50}Mn_{25}In_{25}$ avec couplage *U* et *J*.

Les énergies de formation de la phase d'austénite sans et avec couplage $U = 6$ eV et $J = 0,5$ ont été calculées sur la base de l'état d'équilibre optimisé. L'énergie à l'état fondamental de l'alliage ferromagnétique austénite $Ni_{50}Mn_{25}In_{25}$ est indiquée dans le tableau 1. Une énergie à l'état fondamental plus grande et une énergie de formation plus importante ont été obtenues, ce qui signifie que la prise en compte du couplage Hubbard *U* et *J* rend la structure $L2_1$ moins stable. Sur la base de la comparaison de l'énergie de formation de l'austénite ferromagnétique $Ni_{50}Mn_{25}In_{25}$ avec et sans couplage *U* et *J*, nous avons pu constater que le couplage Hubbard *U* et *J* pouvait réduire la stabilité de la phase d'austénite cubique $L2_1$. Cependant, sur la base de la définition du Hubbard *U*, qui pourrait être utilisé pour intégrer les atomes dans un environnement de polarisation, l'état fondamental serait abaissé [52].

Table 1 Paramètre de réseau optimisé, moment magnétique et énergie de formation de l'austénite cubique $Ni_{50}Mn_{25}In_{25}$ (cellule unitaire à 4 atomes) sans couplage U et J et avec U = 6 eV et J = 0,5.

	a/(Å)	mag/(μ_B)	E_0/(eV)	E_f/(eV)	structure
$Ni_{50}Mn_{25}In_{25}$ (sans couplage $U + J$)	6.061	4.235	-22.838	-0.256	cubic
$Ni_{50}Mn_{25}In_{25}$ (U = 6 eV and J = 0.5)	6.104	5.003	-14.024	-0.059	cubic

Afin de comprendre l'effet du paramètre Hubbard U et J sur la structure électronique de l'alliage $Ni_{50}Mn_{25}In_{25}$, nous avons en outre calculé la structure de bande, la densité des états (DOS) et les différences de densité de charge, comme le montre la figure 3. À partir des structures de bande, nous avons constaté que les paramètres efficaces de Coulomb et d'échange n'ont pas montré de changement significatif autour du niveau de Fermi, et seules certaines structures de bande se sont éloignées du niveau de Fermi. Nous pourrions également trouver un état In p renforcé s'éloignant du niveau de Fermi, lorsque les paramètres effectifs de Coulomb U et J ont été pris en compte. Cependant, avec le couplage de Coulomb effectif et d'échange U et J, la bande interdite montre toujours la liaison métallique dans l'alliage cubique $Ni_{50}Mn_{25}In_{25}$.

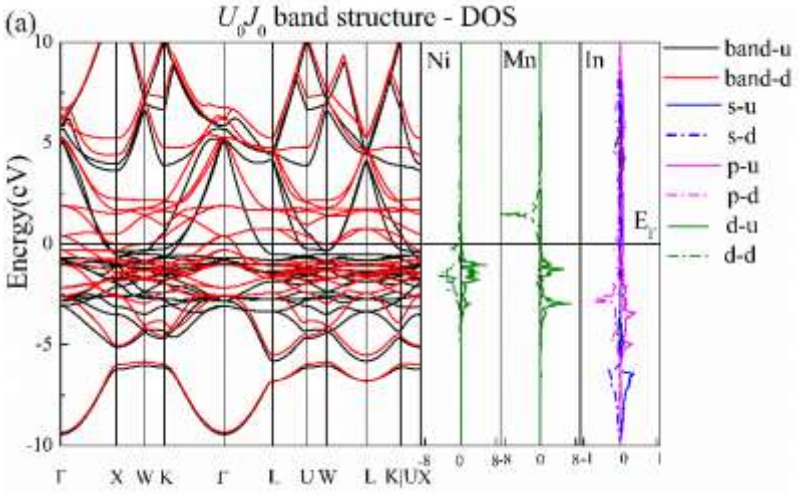

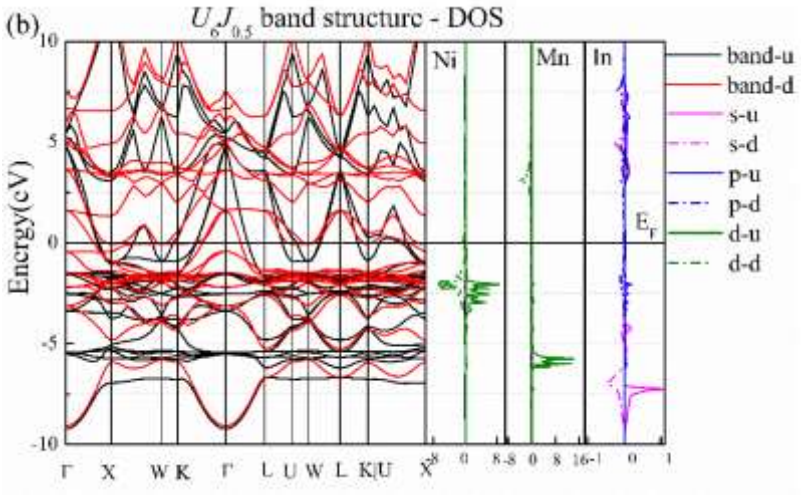

Fig. 3 Structure de bande et densité d'états (DOS) d'austénite de $Ni_{50}Mn_{25}In_{25}$ avec calculs U_0J_0 et $U_6J_{0,5}$.

3.2 Préférence structurelle martensitique dépendante de la composition des alliages $Ni_{50}Mn_xIn_{50-x}$

Pour découvrir la préférence du site de sous-réseau des atomes de Mn en excès, les énergies de formation de différents défauts ponctuels dans la cellule à 16 atomes ont été testées par optimisation de la structure cristalline à l'aide de VASP. Les énergies de formation calculées de l'austénite parfaite et de l'austénite avec 6,25 at. %. sont indiquées dans le tableau 2.

Tableau 2 Paramètres de réseau optimisés et énergie de formation d'austénite parfaite et d'austénite avec défaut ponctuel pour une cellule de 16 atomes (*v* élément indique une situation de vacance).

	a/(Å)	**E_f/ (eV/ cellule élémentaire)**		**a/(Å)**	**E_f/ (eV/ cellule élémentaire)**
v_Ni	6.0261	-0.584	$_{In}Mn$	6.0645	-0.850
v_In	5.9195	0.522	$Ni_8Mn_4In_4$	6.0607	-1.130

Afin de comprendre l'effet de la concentration de Mn sur la préférence de structure martensitique des alliages off-stoechiométriques $Ni_{50}Mn_xIn_{50-x}$ et de révéler l'interaction antiferromagnétique entre les atomes, la distorsion tétragonale a été appliquée pour déterminer les structures stables possibles à 0 K pour la première étape. Les résultats calculés étaient représentés avec la différence d'énergie à l'état fondamental entre la structure déformée et la structure cubique initiale à chaque concentration de Mn. Sur la base de l'analyse d'énergie de formation de défauts ponctuels, quatre alliages $Ni_{50}Mn_xIn_{50-x}$ (x = 25, 29,25, 34,5 et 36,5) avec l'excès de Mn se

substituant à In ($_{In}$Mn) ont été utilisés. Les résultats sont montrés sur la figure 4. On voit sur la figure 4 (a) que, pour le composé stoechiométrique $Ni_{50}Mn_{25}In_{25}$, la structure cubique parfaite avec $c/a = 1$ possède l'énergie d'état fondamental minimale. En revanche, la différence d'énergie de l'état fondamental entre la structure déformée tétragonalement et la structure cubique des alliages hors stœchiométriques $Ni_{50}Mn_xIn_{50-x}$ est négative pour les distorsions $c/a > 1$ et $c/a < 1$. De plus, pour connaître la relation entre la structure stable préférée possible et les teneurs en Mn en excès, la distorsion tétragonale avec $c/a > 1$ et $c/a < 1$ possédant une énergie minimale locale à différentes concentrations de Mn a été ajustée, et les courbes sont présentées sur la figure 4 (b). À partir des résultats, nous pourrions déduire que la stabilité de la structure tétragonale serait améliorée avec l'ajout de Mn supplémentaire, et la structure martensitique préférée passe de la structure tétragonale avec $c/a < 1$ à celle avec $c/a > 1$.

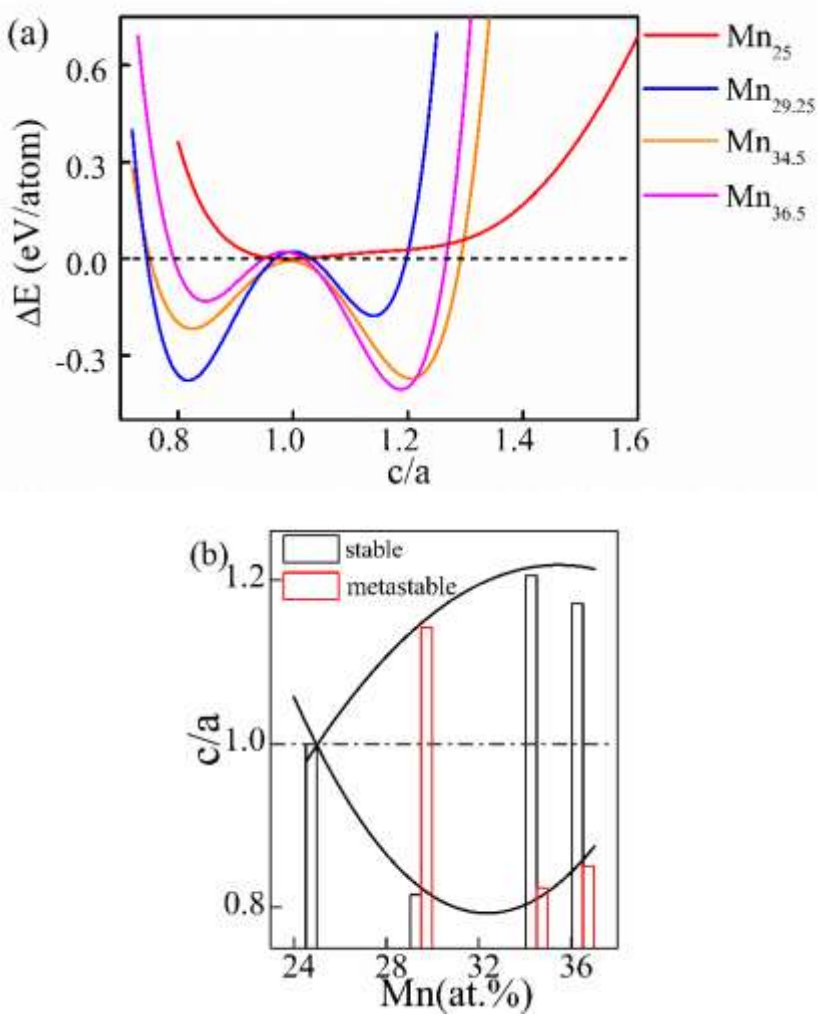

Fig. 4 (a) Variation de la différence d'énergie de l'état fondamental en fonction de la distorsion tétragonale (rapport *c/a*) dans les alliages Ni-Mn-In avec différentes teneurs en Mn. (b) valeur de rapport c / a du point d'énergie minimum local des alliages Ni-Mn-In avec différentes teneurs en Mn. Les courbes paraboliques indiquent la valeur du rapport *c/a* du point d'énergie minimum local pour *c/a* <1 et *c/a* > 1.

Sur la base des résultats ci-dessus de distorsion tétragonale, la préférence de la transition martensitique aux différentes structures tétragonales a été analysée pour les alliages hors stœchiométriques $Ni_{50}Mn_xIn_{50-x}$ avec le Mn supplémentaire ajouté. Comme la structure précise de la structure martensitique préférée sous l'effet de la concentration en Mn n'est toujours pas claire, nous avons construit la structure tétragonale $L1_0$ et la structure orthorhombique (provenant de la martensite monoclinique *6M* [19]) qui correspondent à la structure tétragonale respective avec *c/a* > 1 et *c/a* <1 dans la distorsion tétragonale. On voit que les paramètres de réseau des deux structures montrent une dépendance de composition pour tous les alliages. Le paramètre de réseau (a) de la structure tétragonale $L1_0$ diminue régulièrement avec l'augmentation du Mn supplémentaire. Le volume des structures orthorhombiques diminue également avec l'ajout de Mn supplémentaire.

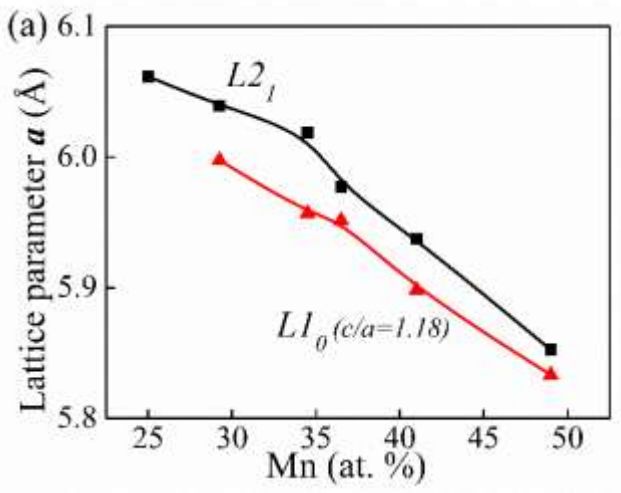

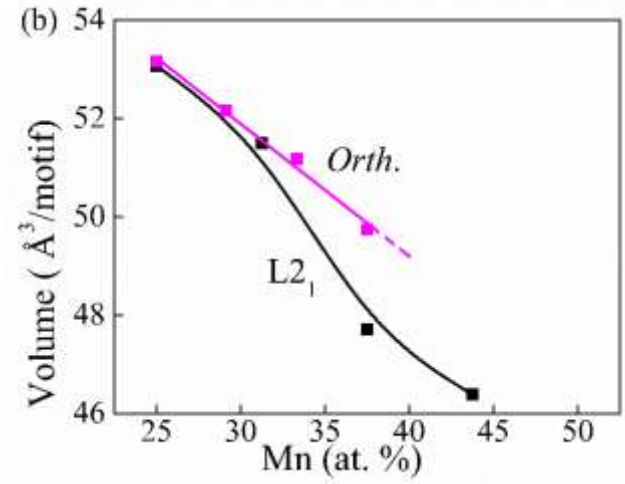

Fig.5 (a) Paramètre de réseau optimisé (a) des structures ferromagnétiques cubiques *L2₁* et tétragonales *L1₀* (*c/a* = 1,18) ; (b) volume cellulaire optimisé des structures ferromagnétiques cubiques *L2₁* et orthorhombiques (la ligne pointillée indique l'extrapolation de l'ajustement.)

Sur la base des paramètres de réseau d'équilibre obtenus, les énergies de formation du *L2₁* cubique, du *L1₀* tétragonal (*c/a* = 1,18) et des structures orthorhombiques ont été calculées pour analyser la préférence de la structure martensitique, comme le montre la Fig. 6. Sur la base des résultats de calcul d'énergie de formation, nous avons constaté que la structure orthorhombique est préférée à des concentrations de Mn plus faibles, et la structure tétragonale *L1₀* devient favorisée à des concentrations de Mn plus élevées. Ainsi, nous pourrions en déduire que l'excès de Mn augmenterait la possibilité de la transition martensitique de l'austénite avec la structure cubique à la martensite avec la structure orthorhombique ou tétragonale. La structure martensitique préférée entre la structure orthorhombique et la structure *L1₀* tétragonale est déterminée par la concentration en Mn.

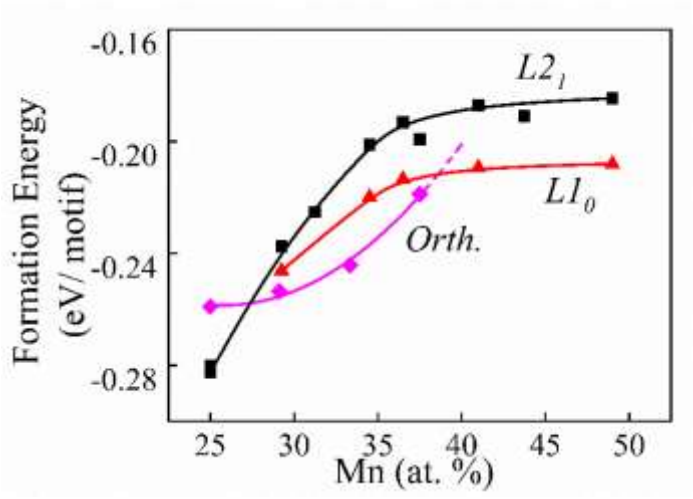

Fig.6 Énergie de formation de $L2_1$ cubique ferromagnétique, $L1_0$ tétragonale avec c/a = 1,18 et structures orthorhombiques en fonction de la concentration en Mn (la ligne pointillée indique l'extrapolation de l'ajustement.)

Le moment magnétique total d'un motif des trois structures a également été calculé pour les alliages hors stœchiométriques avec différentes teneurs en Mn à l'état ferromagnétique. On voit que le moment magnétique total du cubique $L2_1$ et celui de la structure tétragonale $L1_0$ montrent une augmentation avec l'excès de concentration en Mn pour toutes les compositions, et la différence de moment magnétique entre la martensite et l'austénite est assez faible. Nous avons également effectué le calcul du moment magnétique total de l'alliage 34,5 at. % et celui 36,5 at. % Mn à structure tétragonale. Comparé à la martensite ferromagnétique, le moment magnétique total de la martensite à structure tétragonale pour ces deux alliages montre une baisse brutale à environ 2,5 μ_B. Le moment magnétique des atomes de Ni montre un antiferromagnétisme avec une valeur d'environ - 0,2 μ_B et celui de Mn un ferromagnétisme avec une valeur décroissante à 2,25 μ_B. Les résultats suggèrent la coexistence du ferromagnétisme et de l'antiferromagnétisme dans ces deux concentrations. L'interaction antiferromagnétique pourrait provenir de l'interaction d'hybridation Ni-Mn.

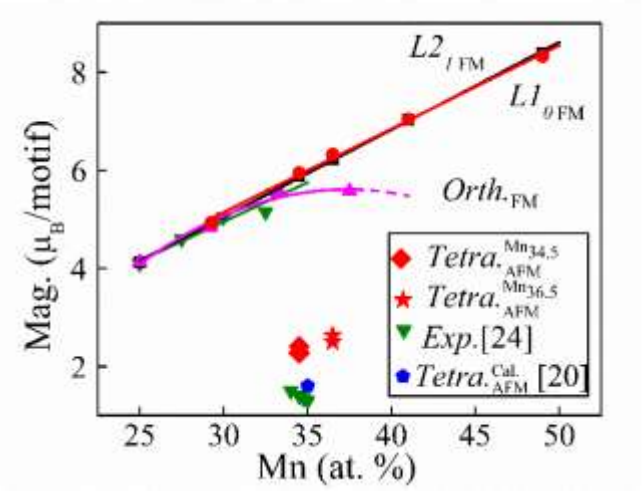

Fig. 7 Moment magnétique total des structures cubiques $L2_1$, tétragonales $L1_0$ et orthorhombiques dans les alliages hors stoechiométriques $Ni_{50}Mn_xIn_{50-x}$ avec différentes teneurs en Mn à l'état ferromagnétique et les structures tétragonales de $Ni_{50}Mn_{34.5}In_{15.5}$ et $Ni_{50}Mn_{36.5}In_{13.5}$ à coexistence ferromagnétique et antiferromagnétique. (La ligne pointillée indique l'extrapolation de l'interpolation.)

3.3 Contributions excitées thermiquement dépendantes de la composition à la stabilité de phase des alliages ferromagnétiques $Ni_{50}Mn_xIn_{50-x}$ à températures finies

Sur la base des énergies d'équilibre de l'austénite et de la martensite NM, nous avons d'abord analysé la stabilité de l'état fondamental à 0 K qui est la partie la plus importante des contributions conventionnelles à l'énergie libre. La Fig.8 présente la différence d'énergie d'équilibre ($\Delta E = E^{mar.} - E^{aut.}$) entre les deux phases à l'état ferromagnétique à 0K en fonction de la teneur en Mn. Les résultats ont montré que les différences d'énergie de toutes les compositions avec un excès de Mn sont négatives, c'est-à-dire que l'énergie totale de la martensite est inférieure à celle de l'austénite à 0K.

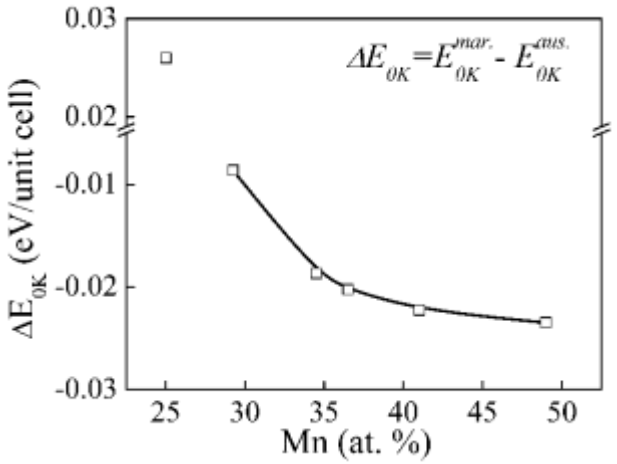

Fig. 8 Différences d'énergie totales à l'état fondamental entre l'austénite et la martensite NM des alliages $Ni_{50}Mn_xIn_{50-x}$

Ensuite, nous avons analysé les excitations de température (y compris l'excitation vibrationnelle, électronique et les entropies magnétiques) des alliages non-stoechiométriques $Ni_{50}Mn_xIn_{50-x}$. Premièrement, l'entropie vibrationnelle (S_{vib}) résultant des interactions phononiques a été calculée sur la base des structures d'équilibre obtenues à 0 K. Les résultats sont présentés sur la figure 9. On peut constater que la valeur d'entropie vibrationnelle de l'austénite est plus grande que celle de la martensite NM à tous les teneurs en Mn. Cela indique que l'entropie vibrationnelle contribue positivement à la déstabilisation de l'austénite à des températures élevées.

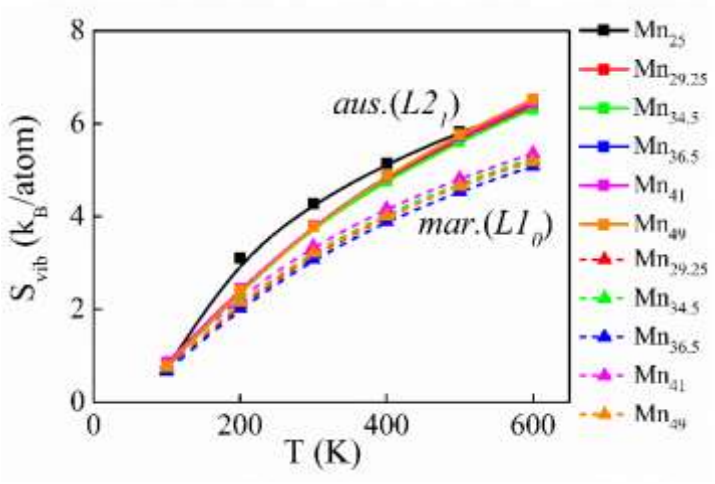

Fig. 9 Entropie vibrationnelle de l'austénite et de la martensite NM des alliages $Ni_{50}Mn_xIn_{50-x}$ à des températures finies avec différentes teneurs en Mn.

Pour comprendre clairement les différences d'entropie entre les deux phases et estimer la tendance de transition de phase à chaque teneur en Mn, les changements d'entropie vibrationnelle ($\Delta S_{vib}^{tr.}$) entre l'austénite et la martensite NM ont également été calculés pour 5 teneurs en Mn à températures finies, et les résultats sont affichés sur la Fig.10.

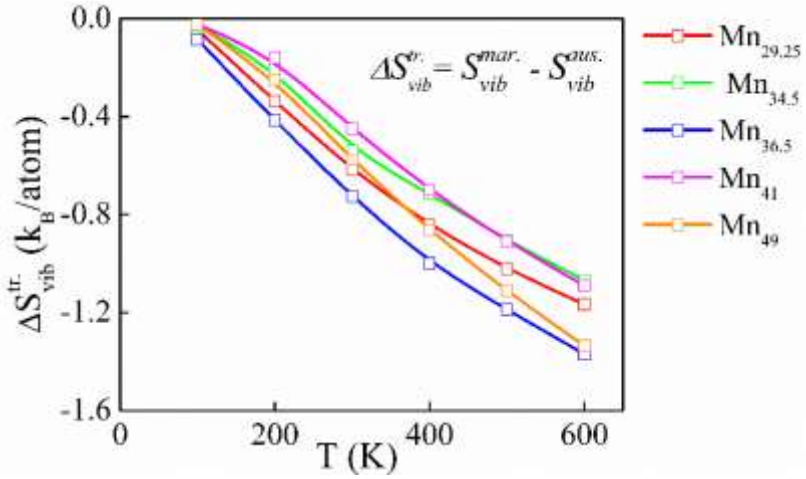

Fig. 10 Changement d'entropie vibratoire entre l'austénite et la martensite NM de l'alliage $Ni_{50}Mn_xIn_{50-x}$ avec différentes concentrations de Mn en fonction de la température.

Comme la deuxième contribution possible à la stabilité de phase peut provenir de l'entropie d'excitation électronique, nous avons en outre calculé les entropies électroniques des deux phases avec des compositions de Mn différentes à des températures finies. Ici, les entropies électroniques de l'alliage $Ni_{50}Mn_{29.25}In_{20.75}$ ont été présentées sur la figure 11 à titre d'exemple représentatif. On voit que les entropies d'excitation électronique (S_{el}) des deux phases augmentent avec

l'augmentation de la température et l'entropie électronique de la martensite NM est plus petite que celle de l'austénite, ce qui est cohérent avec la tendance influente de l'entropie vibrationnelle.

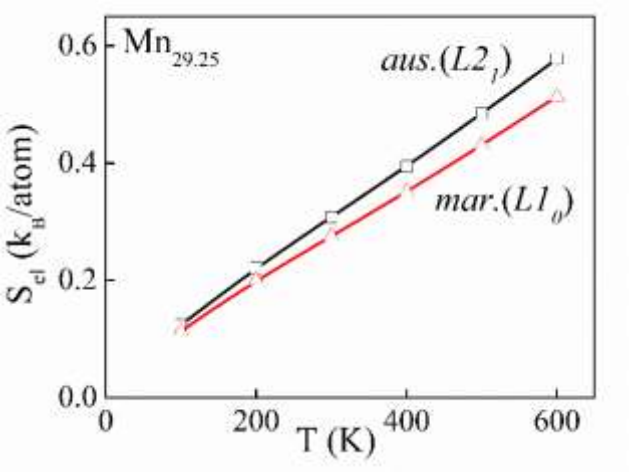

Fig. 11 Entropie électronique de l'austénite et de la martensite NM dans un alliage $Ni_{50}Mn_{29.25}In_{20.75}$ à températures finies.

Ensuite, nous avons utilisé la variation du moment magnétique pour estimer l'effet de la concentration en Mn et de la température sur la stabilité de phase des deux phases. Comme seule la martensite à structure $L1_0$ avec une teneur en Mn d'environ 29 at. % est toujours dominée par l'état ferromagnétique, l'excitation de la température sur les moments magnétiques de l'austénite ferromagnétique et de la martensite ferromagnétique a été analysée et comparée pour l'alliage avec 29,25 at. % Mn. Les résultats sont présentés sur la Fig. 12. On voit que les moments magnétiques de l'austénite montrent une augmentation rapide avec la température puis diminuent légèrement jusqu'à la température de Curie, tandis que ceux de la martensite NM diminuent légèrement avec l'augmentation de la température jusqu'au Curie Température. Cependant, au-dessus de 100 K, les moments magnétiques de l'austénite sont supérieurs à ceux de la martensite. Cela signifie que la contribution magnétique favorise également la transformation de phase comme les contributions vibrationnelles et électroniques.

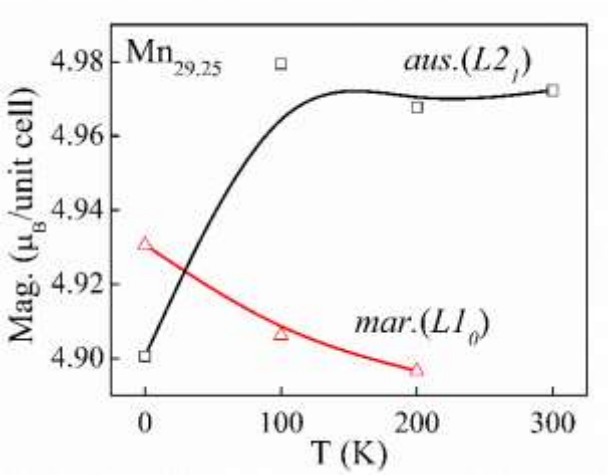

Fig. 12 Moments magnétiques totaux de l'austénite et de la martensite NM dans un alliage $Ni_{50}Mn_{29.25}In_{20.75}$ à températures finies.

4. Conclusion

Dans le but de présenter une structure électronique plus précise près du niveau de Fermi pour l'austénite cubique de l'alliage $Ni_{50}Mn_{25}In_{25}$ avec l'élément de transition métallique Ni et Mn avec des orbitales *3d*, nous avons d'abord essayé de calculer systématiquement les propriétés physiques en considérant les paramètres de Coulomb efficace et d'échange *U* et *J* avec la méthode GGA d'échange-corrélation dans VASP. Cependant, nous n'avons trouvé aucun effet évident sur la structure cristalline d'équilibre ou la structure électronique. Par conséquent, nous n'avons pas ajouté le paramètre Coulomb efficace dans la corrélation d'échange pour des calculs ultérieurs pour les alliages Ni-Mn-In.

L'effet de la concentration de Mn sur la préférence de transition de phase martensitique a été étudié. Les résultats ont montré que la stabilité de la structure tétragonale pouvait être améliorée avec le Mn supplémentaire, et la structure cubique $L2_1$ devient moins stable dans les alliages non stœchiométriques $Ni_{50}Mn_xIn_{50-x}$. Avec l'augmentation de la concentration en Mn, la structure tétragonale stable préférée évolue de la structure tétragonale avec $c/a < 1$ à celle avec $c/a > 1$. Par rapport à la structure cubique $L2_1$, la structure orthorhombique est préférée à des concentrations en Mn plus faibles, et la structure tétragonale $L1_0$ devient préférée à des concentrations de Mn plus élevées. Sous l'optimisation de la structure magnétique, la concentration élevée de Mn pourrait entraîner la coexistence du ferromagnétisme et de l'antiferromagnétisme. Ce dernier pourrait être attribué à l'hybridation antiferromagnétique Ni-Mn.

Les stabilités de phase de l'austénite cubique ordonnée $L2_1$ et de la martensite tétragonale non modulée dans les alliages $Ni_{50}Mn_xIn_{50-x}$ ont été étudiées par simulation des énergies totales à 0 K et des contributions excitées thermiquement (y compris l'entropie vibrationnelle, l'entropie d'excitation électronique et le moment magnétique) à des températures finies. La différence d'entropie vibrationnelle négative entre la martensite et l'austénite augmente avec la température, ce qui indique une possibilité de transition de phase augmentée. Par rapport à la contribution vibrationnelle, la contribution d'excitation électronique est assez faible, mais montre la même tendance à favoriser la transition martensitique. Le moment magnétique total d'une cellule élémentaire d'austénite ferromagnétique augmente avec l'augmentation de la teneur en Mn, et devrait conduire à une augmentation de l'entropie magnétique. Ainsi, l'entropie magnétique apporte également une contribution positive à la transition de phase.

Reference

1. Otsuka, K.; Wayman, C.M. *shape memory materials*; Cambridge University Press, **1998**; ISBN 0521663849;9780521663847;
2. Wayman, C.M. *Introduction to the crystallography of martensitic transformations*; Macmillan: New York, **1964**;
3. Nishiyama, Z. *Martensitic Transformation*; New York: Academic Press, **1978**; ISBN 9780125198509.
4. Kainuma, R.; Oikawa, K.; Ito, W.; Sutou, Y.; Kanomata, T.; Ishida, K. Metamagnetic shape memory effect in NiMn-based Heusler-type alloys. *J Mater Chem* **2008**, *18*, 1837–1842.
5. Lobo, P.S.; Almeida, J.; Guerreiro, L. Shape Memory Alloys Behaviour: A Review. *Procedia Eng* **2015**, *114*, 776–783.
6. Tellinen, J.; Suorsa, I.; Aaltio, I.; Ullakko, K. Basic Properties of Magnetic Shape Memory Actuators. *8th Int Conf ACTUATOR 2002* **2002**, 10–12.
7. Ullakko, K. Magnetically controlled shape memory alloys: A new class of actuator materials. *J Mater Eng Perform* **1996**, *5*, 405–409.
8. Ullakko, K.; Huang, J.K.; Kokorin, V. V.; O'Handley, R.C. Magnetically controlled shape memory effect in Ni_2MnGa intermetallics. *Scr Mater* **1997**, *36*, 1133–1138.
9. Tickle, R.; James, R.D.; Shield, T.; Wuttig, M.; Kokorin, V. V. Ferromagnetic shape memory in the NiMnGa system. *IEEE Trans Magn* **1999**, *35*, 4301–4310.
10. Murray, S.J.; Marioni, M.; Allen, S.M.; O'Handley, R.C.; Lograsso, T.A. 6% magnetic-field-induced strain by twin-boundary motion in ferromagnetic Ni-Mn-Ga. *Appl Phys Lett* **2000**, *77*, 886–888.
11. Kainuma, R.; Imano, Y.; Ito, W.; Morito, H.; Sutou, Y.; Oikawa, K.; Fujita, A.; Ishida, K. Metamagnetic shape memory effect in a Heusler-type $Ni_{43}Co_7Mn_{39}Sn_{11}$ polycrystalline alloy. *Appl Phys Lett* **2006**, *88*, 192513.
12. Sozinov, A.; Likhachev, A.A.; Lanska, N.; Ullakko, K. Giant magnetic-field-induced strain in NiMnGa seven-layered martensitic phase. *Appl Phys Lett* **2002**, *80*, 1746–1748.
13. Ullakko, K.; Huang, J.K.; Kantner, C.; O'Handley, R.C.; Kokorin, V. V. Large magnetic-field-induced strains in Ni_2MnGa single crystals. *Appl Phys Lett* **1996**, *69*, 1966–1968.
14. Sutou, Y.; Imano, Y.; Koeda, N.; Omori, T.; Kainuma, R.; Ishida, K.; Oikawa, K. Magnetic and martensitic transformations of NiMnX(X = In, Sn, Sb) ferromagnetic shape memory alloys. *Appl. Phys. Lett.* **2004**, *85*, 4358–4360.
15. Umetsu, R.Y.; Xu, X.; Kainuma, R. NiMn-based metamagnetic shape memory alloys. *Scr Mater* **2016**, *116*, 1–6.
16. McCormack, R.; de Fontaine, D. First-principles study of multiple order-disorder transitions in Cd_2AgAu Heusler alloys. *Phys Rev B* **1996**, *54*, 9746–9755.
17. Khovailo, V.V.; Takagi, T.; Vasil'ev, A.N.; Miki, H.; Matsumoto, M.; R. Kainuma On Order-Disorder ($L2_1$ -> B2') Phase Transition in $Ni_{2+x}Mn_{1-x}Ga$ Heusler Alloys. *Phys Stat Sol* **2001**, *183*, R1–R3.
18. Miyamoto, T.; Ito, W.; Umetsu, R.Y.; Kainuma, R.; Kanomata, T.; Ishida, K. Phase stability and magnetic

properties of $Ni_{50}Mn_{50-x}In_x$ Heusler-type alloys. *Scr Mater* **2010**, *62*, 151–154.

19. Yan, H.L.; Zhang, Y.D.; Xu, N.; Senyshyn, A.; Brokmeier, H.G.; Esling, C.; Zhao, X.; Zuo, L. Crystal structure determination of incommensurate modulated martensite in Ni-Mn-In Heusler alloys. *Acta Mater* **2015**, *88*, 375–388.
20. Krenke, T.; Acet, M.; Wassermann, E.F.; Moya, X.; Mañosa, L.; Planes, A. Ferromagnetism in the austenitic and martensitic states of Ni-Mn-In alloys. *Phys Rev B* **2006**, *73*, 174413.
21. Zhang, C.Y.; Zhang, Y.D.; Esling, C.; Zhao, X.; Zuo, L. Crystallographic features of the martensitic transformation and their impact on variant organization in the intermetallic compound $Ni_{50}Mn_{38}Sb_{12}$ studied by SEM/EBSD. *IUCrJ* **2017**, *4*, 700–709.
22. Planes, A.; Mãnosa, L.; Acet, M. Magnetocaloric effect and its relation to shape-memory properties in ferromagnetic Heusler alloys. *J Phys Condens Matter* **2009**, *21*, 223201.
23. Umetsu, R.Y.; Ito, W.; Ito, K.; Koyama, K.; Fujita, A.; Oikawa, K.; Kanomata, T.; Kainuma, R.; Ishida, K. Anomaly in entropy change between parent and martensite phases in the $Ni_{50}Mn_{34}In_{16}$ Heusler alloy. *Scr mater* **2009**, *60*, 25–28.
24. Pérez-sierra, A.M.; Bruno, N.M.; Pons, J.; Cesari, E.; Karaman, I. Atomic order and martensitic transformation entropy change in Ni-Co-Mn-In metamagnetic shape memory alloys. *Scr mater* **2016**, *110*, 61–64.
25. Kazakov, A.P.; Prudnikov, V.N.; Granovsky, A.B.; Zhukov, A.P.; Gonzalez, J.; Dubenko, I.; Pathak, A.K.; Stadler, S.; Ali, N. Direct measurements of field-induced adiabatic temperature changes near compound phase transitions in Ni-Mn-In based Heusler alloys. *Appl. Phys. Lett.* **2011**, *98*, 131911.
26. Oikawa, K.; Ito, W.; Imano, Y.; Sutou, Y.; Kainuma, R.; Ishida, K.; Okamoto, S.; Kitakami, O.; Kanomata, T. Effect of magnetic field on martensitic transition of $Ni_{46}Mn_{41}In_{13}$ Heusler alloy. *Appl. Phys. Lett.* **2006**, *88*, 122507.
27. Kustov, S.; Corro, M.L.; Pons, J.; Cesari, E. Entropy change and effect of magnetic field on martensitic transformation in a metamagnetic Ni-Co-Mn-In shape memory alloy. *Appl. Phys. Lett.* **2009**, *94*, 191901.
28. Dubenko, I.; Pathak, A.K.; Stadler, S.; Ali, N.; Kovarskii, Y.; Prudnikov, V.N.; Perov, N.S.; Granovsky, A.B. Giant Hall effect in Ni-Mn-In Heusler alloys. *Phys Rev B* **2009**, *80*, 092408.
29. Chatterjee, S.; Singh, V.R.; Deb, A.K.; Giri, S.; De, S.K.; Dasgupta, I.; Majumdar, S. Magnetic properties of $Ni_{2+x}Mn_{1-x}In$ Heusler alloys: Theory and experiment. *J Magn Magn Mater* **2010**, *322*, 102–107.
30. Kanomata, T.; Yasuda, T.; Sasaki, S.; Nishihara, H.; Kainuma, R.; Ito, W.; Oikawa, K.; Ishida, K.; Neumann, K.; Ziebeck, K.R.A. Magnetic properties on shape memory alloys $Ni_2Mn_{1+x}In_{1-x}$. *J Magn Magn Mater* **2009**, *321*, 773–776.
31. Kresse, G.; Furthmüller, J.; Hafner, J. Ab initio force constant approach to phonon dispersion relations of diamond and graphite. *Epl* **1995**, *32*, 729–734.
32. Kresse, G.; Hafner, J. Ab Initio Molecular Dynamics of Liquid Metals. *Phys Rev B* **1993**, *47*, 558–561.
33. Kresse, G.; Furthmüller, J. Efficiency of ab-initio total energy calculations for metals and semiconductors using a plane-wave basis set. *Comput Mater Sci* **1996**, *6*, 15–50.

34. Blöchl, P.E. Projector augmented-wave method. *Phys Rev B* **1994**, *50*, 17953–17979.
35. Hafner, J. Atomic-scale computational materials science. *Acta mater* **2000**, *48*, 71–92.
36. Perdew, J.P.; Burke, K.; Ernzerhof, M. Generalized gradient approximation made simple. *Phys Rev Lett* **1996**, *77*, 3865–3868.
37. Monkhorst, H.J.; Pack, J.D. Special points for Brillouin-zone integrations. *Phys Rev B* **1977**, *13*, 5188–5192.
38. Ma, D.; Grabowski, B.; Körmann, F.; Neugebauer, J.; Raabe, D. Ab initio thermodynamics of the CoCrFeMnNi high entropy alloy: Importance of entropy contributions beyond the configurational one. *Acta mater* **2015**, *100*, 90–97.
39. Wallace, D.C. *Thermodynamics of Crystals*; Dover books on physics; Dover Publications, **1998**; ISBN 9780486402123.
40. Grabowski, B.; Hickel, T.; Neugebauer, J. Ab initio study of the thermodynamic properties of nonmagnetic elementary fcc metals: Exchange-correlation-related error bars and chemical trends. *Phys Rev B* **2007**, *76*, 024309.
41. Blanco, M.A.; Francisco, E.; Luaña, V. GIBBS: Isothermal-isobaric thermodynamics of solids from energy curves using a quasi-harmonic Debye model. *Comput Phys Commun* **2004**, *158*, 57–72.
42. Otero-De-La-Roza, A.; Abbasi-Pérez, D.; Luaña, V. Gibbs2: A new version of the quasiharmonic model code. II. Models for solid-state thermodynamics, features and implementation. *Comput Phys Commun* **2011**, *182*, 2232–2248.
43. Otero-De-La-Roza, A.; Luaña, V. Gibbs2: A new version of the quasi-harmonic model code. I. Robust treatment of the static data. *Comput Phys Commun* **2011**, *182*, 1708–1720.
44. Vitos, L. *Computational quantum mechanics for materials engineers: the EMTO method and applications*; Springer US: Boston, MA, **2005**; ISBN 9781846289507.
45. Mermin, N.D. Thermal properties of the inhomogeneous electron gas. *Phys Rev* **1965**, *137*, 1441–1443.
46. Marx, D.; Hutter, J. Ab initio molecular dynamics: Theory and implementation. In *Modern Methods and Algorithms of Quantum Chemistry*; **2000**; Vol. 1, pp. 301–449 ISBN 3000056181.
47. Halilov, S. V.; Perlov, A.Y.; Oppeneer, P.M.; Eschrig, H. Magnon spectrum and related finite-temperature magnetic properties: A first-principle approach. *Europhys Lett* **1997**, *39*, 91–96.
48. Körmann, F.; Dick, A.; Grabowski, B.; Hallstedt, B.; Hickel, T.; Neugebauer, J. Free energy of bcc iron: Integrated ab initio derivation of vibrational, electronic, and magnetic contributions. *Phys Rev B* **2008**, *78*, 033102.
49. Li, C.M.; Luo, H. Bin; Hu, Q.M.; Yang, R.; Johansson, B.; Vitos, L. First-principles investigation of the composition dependent properties of $Ni_{2+x}Mn_{1-x}Ga$ shape-memory alloys. *Phys Rev B* **2010**, *82*, 024201.
50. Pérez-Landazábal, J.I.; Recarte, V.; Sanchez-Alarcos, V.; Ruiz, M.J.; Cesari, E. Outstanding role of the magnetic entropy in arrested austenite in an ordered $Ni_{45}Mn_{36.7}In_{13.3}Co_5$ metamagnetic shape memory alloy. *Scr Mater* **2019**, *168*, 91–95.
51. Mañosa, L.; Planes, A.; Ortín, J.; Martínez, B. Entropy change of martensitic transformations in Cu-based shape memory alloys. *Phys Rev B* **1993**, *48*, 3611–3619.

52. Brink, J. Van Den; Meinders, M.B.J.; Sawatzky, G.A. Influence of screening effects and inter-site Coulomb repulsion on the insulating correlation gap. **1995**, *207*, 682–684.